Parabolic Variational Problems of 1-Laplacian Type and Finite Element Models of Protein Diffusion and Homogenized Cone Photoreceptor Visual Transduction

By

Colin James Stockdale Klaus

Dissertation

Submitted to the Faculty of the

Graduate School of Vanderbilt University

in partial fulfillment of the requirements

for the degree of

DOCTOR OF PHILOSOPHY

in

Mathematics

August 31, 2017

Nashville, Tennessee

Approved:

Emmanuele DiBenedetto, Ph.D.

Larry Schumaker, Ph.D.

Gieri Simonett, Ph.D.

Glenn Webb, Ph.D.

Vsevolod Gurevich, Ph.D.

Anne Kenworthy, Ph.D.

Dedication

To my parents, Jim and Lisa, and to my siblings, Karl and Lydia, who always support me.

Acknowledgments

My adviser is fond of saying that research is an activity you do with friends. Foremost I would like to thank my adviser, Emmanuele, who has encouragingly and caringly believed in me as I undertook this research process. A close collaborator of ours, Ugo Gianazza at the Universita di Pavia, has been a kind and warm host and mentor through our total variation flow collaborations. Giovanni Caruso at the Italian National Research Council was my Finite Elements mentor in Cone Visual Transduction. His friendship and humor were as fundamental to this research experience as the work itself. Krishnan Raghunathan coauthored with me our paper on diffusion in tubules. I have gladly enjoyed our many discussions. I am grateful to both Anne Kenworthy and Seva Gurevich who took to teaching biology to a math-minded person with enthusiasm and welcome. I am also grateful to Larry Schumaker for his thoughts and discussion on several of the numerical issues we encountered.

TABLE OF CONTENTS

List of Tables

List of Figures

Chapter 1

Introduction

This thesis includes four different projects. The first two are projects in classical analysis. First a necessary and sufficient condition for the continuity at a point of minima for parabolic variational integrals with linear growth is obtained. Second a topology of convergence through which solutions of the parabolic p-Laplacian (P-LAP) $u_t = \text{div}\left[|Du|^{p-2}Du\right]$ converge to the parabolic 1-Laplacian (1-Lap) is quantified. In the (1-Lap) case solutions are naturally taken in the class of bounded variation rather than Sobolev spaces. The equations are recast as parabolic variational integrals and the convergence is accomplished in the variational setting rather than the customary weak formulation.

The final two projects are in computational mathematics applied to math biology. The third project numerically models surface, Laplace-Beltrami driven diffusion of proteins along tube-shaped cell membranes. This Finite Element code was built using *B-splines* whose general advantages over the standard linear, nodal interpolant splines extend to rates of convergence, shape control, and degree of smoothness. In the fourth project, a program of homogenization and concentrating capacity has been applied to a PDE system for diffusing, biological 2^{nd} messengers, Ca^{2+} and cGMP, in the rod and cone visual photoreceptors of vertebrate retina with a nonlinear couple in the Neumann data. This model is numerically implemented through Finite Element code after having formally determined the homogenized limit. Convergence of the nonhomogenized model towards the homogenized one is investigated numerically by successively increasing the number of discs in the nonhomogenized model and comparing the current response across models. Findings and time cost of the models are reported. Both these latter projects are interdisciplinary and have been conducted alongside mathematicians and biologists.

1 The Parabolic 1-Laplacian: Solutions' Regularity and Their Approximation by p-Laplacian Solutions

The origins of the p-Laplacian and its limiting cases, *e.g.* 1-Laplacian, are rooted in the heat equation. The p-Laplacian describes diffusion phenomena when the *conductivity*, $|\nabla u|^{p-2}$, is a function of the space-gradient of the diffusing quantity u. It occurs in geometry and with quasi-conformal mappings for p=N ([1],[2]) and elsewhere in the study of non-newtonian fluids [3]. There the distinctions between regimes $[p > 2]$ and $[p < 2]$ are physical and correspond to *super-fluidity* and *super-viscosity* (e.g. jelly or rheologic fluids [4]) respectively. The fine regularity of this operator has been extensively studied. This paves the way for a study of its limiting cases. The interest herein concerns the $p \to 1$ case. In fact, the 1-Lap itself has strong motivations: In image processing ([5],[6]), 1-Lap flows are advantageous for BV's ability to exhibit jump discontinuities. There boundaries of image curves may be sharpened rather than blurred. In geometry, where u is a parabolic 1-Lap solution, the evolution is a mean curvature geometric flow for the level sets $[u = k]$ ([7]).

For convenience the main result of [8] is surveyed here while developed in its own chapter. Let E be an open set of $\mathbb{R}^N$ for $T > 0$ and E_T denote the space-time cylinder $E \times (0,T]$. Consider formally the quasi-linear parabolic differential equation

$$u_t - \operatorname{div}\left[|Du|^{-1} Du\right] = 0 \text{ weakly in } E_T \tag{1.1}$$

Solutions of (1.1) can be made precise by requiring that they be parabolic variational solutions in the sense of Wieser ([9],[10]). A function $u \in L^1_{loc}(0,T;BV_{loc}(E))$ is a variational solution of (1.1) and a local parabolic minimizer of the total variation flow in E_T if for all nonnegative $\varphi \in C_0^\infty(E_T)$

$$\int_0^T \left[\int_E -u\varphi_t dx + \|Du(t)\|(E)\right] dt \leq \int_0^T \|D(u-\varphi)\|(E)\, dt \tag{1.2}$$

Formally applying the Euler-Lagrange procedure to (1.2) returns (1.1). Letting $p \to 1^+$, (1.1) may be regarded as a formal limit of the family of p-Laplacian equations.

$$u_t - \operatorname{div}\left[|Du|^{p-2} Du\right] = 0 \text{ weakly in } E_T$$

In the case of the p-Laplacian, it is known that a Hölder modulus of continuity can be quantified in terms of an *a priori* bound for the solution and the equation itself. Because of their BV nature, 1-Laplacian solutions are not expected to be continuous and an *a priori* modulus of continuity cannot be quantified from boundedness and the equation alone. In **Theorem 1.1** below, we give a necessary and sufficient condition for solutions to be continuous at a point. In the above sense our result of [8] optimally gives a criterion for continuity

Theorem 1.1 *Let $u \in L^1_{loc}(0,T;BV_{\text{loc}}(E))$ be a local parabolic minimizer of the total variation flow (1.2) in E_T which satisfies in addition*

$$u \in L^\infty_{\text{loc}}(E_T) \text{ and } u_t \in L^1_{\text{loc}}(E_T)$$

Then u is continuous at some $(x_0,t_0) \in E_T$ if and only if

$$\limsup_{\rho \to 0} \frac{\rho}{|Q_\rho|} \int_{t_0-\rho}^{t_0} \|Du(\cdot;t)\| \left(B_\rho(x_0)\right) dt = 0$$

Turning to the task of quantifying a topology of convergence where solutions of the p-Laplacian tend to those of the 1-Laplacian, this work is driven by two main theorems found in Chapter 3:

Theorem 1.2 *Under the assumptions given in Chapter 3, when $p \to 1$, we have that for any $T > 0$, the p-Laplacian variational solutions $u_p \to u_1$ in $L^q(\Omega^*_T)$ for any $1 \le q < \frac{N}{N-1}$, and $\partial_t u_p \to \partial_t u_1$ in $L^2_w(\Omega^*_T)$, where $u_1 \in L^1_w(0,T;BV_{u_o}(\Omega)) \cap C^0\left([0,T];L^2(\Omega^*)\right)$ is a variational solution to the Cauchy-Dirichlet Problem for the total variation flow.*

The latter theorem depends on a density result:

Theorem 1.3 $\left\{L^\infty\left(0,T;u_o+C^\infty_{o,\gamma,p}(\Omega)\right)\right\}_{\gamma>0}\cap L^\infty\left(0,T;L^2(\Omega)\right)$ *is dense in the space* $L^1\left(0,T;BV_{u_o}(\Omega)\right)$.

In proving the convergence of these Cauchy-Dirichlet problems, a chief obstacle is the loss of weak* convergence of traces in $BV(\Omega)$. This difficulty is overcome by suitably extending the solutions into a larger domain through a single extension of their common trace.

2 Finite Element Approximations of Laplace-Beltrami Diffusions of Proteins

Lateral diffusion of proteins in highly regulated, curved cell membranes is commonplace and plays important roles in processes such as neuronal signaling, immunological reactions, receptor endocytosis, protein recruitment, and many signaling pathways. Classical cell diffusion models assume the membrane to be planar ([11]). However, geometry affects concentration gradients. This has been demonstrated for tubular geometries ([12],[13]). To study geometric influence, we implemented a numerical Finite Element, Laplace-Beltrami driven diffusion for geometrically complex surfaces using membrane tubules as a biologically relevant example. Tubular membrane geometries are typical of numerous structures found in cells including dendritic spines, the endoplasmic reticulum, membrane nanotubes, primary cilia, clathrin-independent carriers and sorting tubules emanating from endosomes and the trans-Golgi network [14]

The results here are presented in detail in our paper [15]. From first principles, a Laplace-Beltrami driven diffusion model was justified and applied to tubular surfaces. A finite element methods (FEM) solver was built for both symmetric and bivariate, nonsymmetric cases. The numerical, symmetric solution is computed by Galerkin, semi-discrete methods applied to normalized B-splines [16]. B-splines can lead to faster convergence rates and avoid artifacts like negativity in contrast to nodal basis splines. B-splines further allow the user to work in conforming spaces of arbitrary smoothness and polynomial degree.

A tubule may be modeled as a cylinder with length h and radius r attached to a hemispherical cap of radius r. We compared our simulations with experimental work measuring protein diffusion in curved membrane tethers ([12]). The simulated FEM data (closed circles Fig. 2) closely agree with the experimental (open circle, Figure 2). We next performed numerical experiments over biophysically relevant ranges of radii and lengths. We found changing the radius does not substantially impact the concentration profile in the tubule. We observed concentration gradients to be different for different tubule lengths with identical radii.

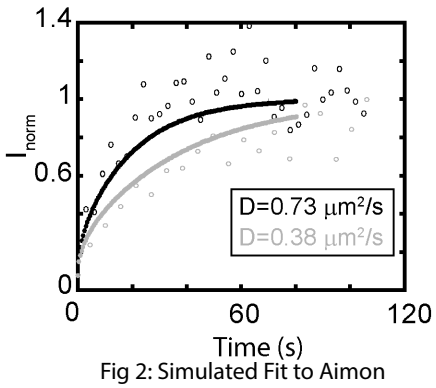

Figure 1.1: Simulated Fit to Aimon

It was illuminating to compare diffusion on a tubule to diffusion on a corresponding flat surface. We design curved and flat surface pairs that are comparable by enforcing that they share a common amount of total material (global area). In one it is curved like a tube where the other it is a planar disc laid flat. Due to Gaussian curvature, we cannot expect a local, isometric correspondence between these two model spaces. However, nor would we want the two surfaces to be equivalent. That would erase curvature differences. Varying every parameter of interest, we found that compared to the flat geometry, the material diffusion from the hemisphere was slowed in the tubular geometry. In some cases, the magnitude of this effect was nearly 20 percent.

3 Homogenization and Concentrated Capacity in Cone Photoreceptors

Sight is produced by visual transduction in the rod and cone outer segments. Here the second messengers, Ca^{2+} and cGMP, diffuse within the slight outer membrane and many, thin layers of the cytosol [17]. Though thin, incised domains and similar biochemically, these outer segments differ in their global architecture. These geometries (cylin-

der vs cone) inform rods' and cones' main biochemical and biophysical functions. Their biochemstry acts at three disparate scales across three orders of magnitude (global 10μm, membrane/layers 10nm, molecular 100Å). This discrepancy renders mathematical modeling and its numerical implementations challenging. To mediate between scales, the techniques of homogenization and concentrating capacity have been applied to messenger diffusion in domains that model the cone outer segment of human eyes and vertebrate animals. The technique of homogenization may be traced back to DeGiorgi who conceived it while studying fine-scale and periodically scattered impurities in media [18]. Concentrating capacity goes back to Tychonov who was interested in limiting cases of heat diffusion in thin slabs [19].

An outer segment may be modeled as a cone in which one makes discal, volume cuts along the cross sections with width and vertical spacing of ε-order. These incisions mimic the layered cytosol. An angular portion of lateral surface is replaced with an ε-sliver of extended, conical volume, resembling the "residual" outer membrane. Though $\mathrm{O}(\varepsilon)$ in size, the discs carry messenger fluxes that regulate diffusion, and the membrane conducts a current modulating vision [17]. These necessitate tracking the small order structures.

Initially, the diffusion is modeled pointwise for each layered, ε-domain. One enforces the heat equation, $a_\varepsilon \frac{\partial}{\partial t} u_\varepsilon - \operatorname{div}\{a_\varepsilon(x)\nabla u_\varepsilon\} = 0$, weakly and extracts the solutions $\{u_\varepsilon\}$. Variational data is taken at the discs and properly balanced over the boundaries to reflect the underlying biochemistry. This method encodes the biophysics at its own scales and locations. The a_ε express concentrating capacity. They are of unity everywhere but the membrane, where their ε-growth is of the inverse order that the sliver shrinks. These balances are to preserve the cytosol's biophysics. As $\varepsilon \to 0$, the interdiscal regions narrow, growing in number. The sliver retracts onto the cone's surface. A PDE process for the weak limit of the solutions u_ε is then extracted formally.

For clarity, I here describe the salient features of the formal, homogenized and concentrated capacity limit in the single prototype cGMP messenger context. The limit contains

three novel components:

- A principle diffusion term $\Delta_{\bar{x}} u = \dfrac{\partial^2 u}{\partial x^2} + \dfrac{\partial^2 u}{\partial y^2}$ in the horizontal variables $\bar{x} = (x, y)$. Homogenization reveals that the discs are barriers to $z-$dimensional diffusion along the axis of the cone. As the number of interposing discs grows over the u_ε problems, the $z-$dimensional height of interconical chambers diminishes, so that in the limit it is vanishing.

- A volume source term of $-(u - f(u))$ type not present in the u_ε problems.
  At their interface with the cytosolic interior, the discs site Neumann terms in the u_ε problems. These are recast into the interior per integration by parts and their limit taken. This produces the above. The resultant $-u$ encodes cGMP hydrolysis by the effector Phosphodiesterase. The resultant and nonlinear $f(u)$ encodes the synthesis of cGMP by GCAP stimulated Guanylate Cyclase.

- A Laplace-Beltrami diffusion for the trace of u at the boundary of the retracted sliver. In the family of u_ε problems and within the sliver only, the coefficient of diffusivity contains a $1/\varepsilon$ term to balance the sliver's volume diminishing like $O(\varepsilon)$. In the energy estimates, this method of Tychonov then generates the Steklov average of u_ε, taken obliquely to the surface, in the surface measure of the boundary interface between cone and sliver. Testing by an appropriate class of function determined by that oblique direction, the diffusion PDE formally tends to the surface Laplace-Beltrami.

The homogenized, concentrated capacity limit couples an interior 3d volume diffusion with a 2d surface diffusion. We have a system of coupled PDE's in dimensionally different domains. A Matlab based finite element code has been written for cGMP diffusion and its companion second messenger Ca^{2+} both in the homogenized and nonhomogenized cases. Both codes have been included. Tables are given that report the relative errors between these two models as well as the difference in time cost to simulate. A table of param-

eters used in the model has also been gathered from the existing biochemical literature. How those values were derived and the meaning of those parameters within the model is discussed. A small collection of numerical experiments is also included.

Chapter 2

A Necessary and Sufficient Condition for the Continuity of Local Minima of Parabolic Variational Integrals with Linear Growth

This chapter was published under this title in *The Journal of Advances in Calculus of Variations* in July 2017 and online January 2016, [8].

1 Introduction

For proper minimizers of parabolic variational integrals with linear growth with respect to $|Du|$, we establish a necessary and sufficient condition for u to be continuous at a point (x_o,t_o), in terms of a sufficient fast decay of the total variation of u about (x_o,t_o) (see (1.4) below). These minimizers arise also as proper solutions to the parabolic 1-laplacian equation. Hence, the continuity condition continues to hold for such solutions.

Let E be an open subset of $\mathbb{R}^N$, and denote by $BV(E)$ the space of functions $v \in L^1(E)$ with finite total variation [20]

$$\|Dv\|(E) := \sup_{\substack{\varphi\in[C_o^1(E)]^N \\ |\varphi|\le 1}} \left\{ \langle Dv, \varphi\rangle = -\int_E v \operatorname{div}\varphi \, dx \right\} < \infty.$$

Here $Dv = (D_1 v, \dots, D_N v)$ is the vector valued Radon measure, representing the distributional gradient of v. A function $v \in BV_{\text{loc}}(E)$ if $v \in BV(E')$ for all open sets $E' \subsetneq E$. For $T > 0$, let $E_T = E \times (0,T)$, and denote by $L^1(0,T;BV(E))$ the collection of all maps $v : [0,T] \to BV(E)$ such that

$$v \in L^1(E_T), \qquad \|Dv(t)\|(E) \in L^1(0,T),$$

and the maps

$$(0,T) \ni t \to \langle Dv(t), \varphi \rangle$$

are measurable with respect to the Lebesgue measure in $\mathbb{R}$, for all $\varphi \in [C_o^1(E)]^N$.

A function $u \in L^1_{\text{loc}}\big(0,T;BV_{\text{loc}}(E)\big)$ is a local parabolic minimizer of the total variation flow in E_T, if

$$\int_0^T \Big[\int_E -u\varphi_t dx + \|Du(t)\|(E) \Big] dt \leq \int_0^T \|D(u-\varphi)(t)\|(E) dt \tag{1.1}$$

for all non-negative $\varphi \in C_o^\infty(E_T)$. The notion has been introduced in [9] and modeled in [10]. It is a parabolic version of the elliptic local minima of total variation flow as introduced in [21].

2 The Main Result

Let $B_\rho(x_o)$ denote the ball of radius ρ about x_o. If $x_o = 0$, write $B_\rho(x_o) = B_\rho$. Introduce the cylinders $Q_\rho(\theta) = B_\rho \times (-\theta\rho, 0]$, where θ is a positive parameter to be chosen as needed. If $\theta = 1$ we write $Q_\rho(1) = Q_\rho$. For a point $(x_o,t_o) \in \mathbb{R}^{N+1}$ we let $[(x_o,t_o) + Q_\rho(\theta)]$ be the cylinder of "vertex" at (x_o,t_o) and congruent to $Q_\rho(\theta)$, i.e.,

$$[(x_o,t_o) + Q_\rho(\theta)] = B_\rho(x_o) \times (t_o - \theta\rho, t_o],$$

and we let $\rho > 0$ be so small that $[(x_o,t_o) + Q_\rho(\theta)] \subset E_T$.

Theorem 2.1 *Let $u \in L^1_{\text{loc}}\big(0,T;BV_{\text{loc}}(E)\big)$ be a local parabolic minimizer of the total variation flow in E_T, satisfying in addition*

$$u \in L^\infty_{\text{loc}}(E_T) \quad \text{and} \quad u_t \in L^1_{\text{loc}}(E_T). \tag{2.1}$$

Then, u is continuous at some $(x_o,t_o)\in E_T$, if and only if

$$\limsup_{\rho\searrow 0}\frac{\rho}{|Q_\rho|}\int_{t_o-\rho}^{t_o}\|Du(\cdot,t)\|(B_\rho(x_o))dt=0. \tag{2.2}$$

For stationary, elliptic minimizers, condition (2.2) has been introduced in [21]. The stationary version of (2.2) implies that u is quasi-continuous at x_o. For time-dependent minimizers, however, (2.2) gives no information on the possible quasi-continuity of u at (x_o,t_o). Condition (2.2), is only a measure-theoretical restriction on the speed at which a possible discontinuity may develop at (x_o,t_o). For this reason our proof is entirely different than [21], being based instead on a DeGiorgi-type iteration technique that exploits precisely such a measure-theoretical information.

3 Comments on Boundedness and Continuity

The theorem requires that u is locally bounded and that $u_t\in L^1_{\rm loc}(E_T)$. In the elliptic case, local minimizers of the total gradient flow in E, are locally bounded ([21, § 2]). This is not the case, in general, for parabolic minimizers in E_T, even if $u_t\in C^\infty_{\rm loc}\big(0,T;L^1_{\rm loc}(E)\big)$. Consider the function

$$B_1\times(-\infty,1)\ni(x,t)\to F(|x|,t)=(1-t)\frac{N-1}{|x|},\quad \text{for } N\geq 3.$$

Denote by D_aF that component of the measure DF which is absolutely continuous with respect to the Lebesgue measure in $\mathbb{R}^N$. One verifies that $DF=D_aF$ and $\|DF(t)\|(B_1)=\|D_aF(t)\|_{1,B_1}$. By direct computation

$$\int_0^T\int_{B_1}\Big(-F\varphi_t+\frac{D_aF}{|D_aF|}\cdot D\varphi\Big)dxdt=0,$$

for all $\varphi \in C_o^\infty\big(B_1 \times (0,T)\big)$, $0 < T < 1$. From this

$$\int_0^T \int_{B_1} \Big(-F\varphi_t + \frac{D_a F}{|D_a F|} \cdot D_a F \Big) dxdt = \int_0^T \int_{B_1} \frac{D_a F}{|D_a F|} \cdot D_a (F - \varphi) dxdt,$$

which yields

$$\int_0^T \int_{B_1} \Big(-F\varphi_t + |D_a F| \Big) dxdt \leq \int_0^T \int_{B_1} |D_a (F - \varphi)| dxdt.$$

Thus F is a local, unbounded, parabolic minimizer of the total variation flow. The requirement $u \in L^\infty_{\rm loc}(E_T)$ could be replaced by asking that $u \in L^r_{\rm loc}(E_T)$ for some $r > N$. A discussion on this issue is provided in Section 13.

4 On the Modulus of Continuity

While Theorem 2.1 gives a necessary and sufficient condition for continuity at a given point, it provides no information on the modulus of continuity of u at (x_o, t_o). Consider the two time-independent functions in $B_\rho \times (0,\infty)$, for some $\rho < 1$:

$$u_1(x_1,x_2) = \begin{cases} \dfrac{1}{\ln x_1} & \text{for } x_1 > 0; \\ \\ 0 & \text{for } x_1 = 0; \\ \\ -\dfrac{1}{\ln(-x_1)} & \text{for } x_1 < 0. \end{cases}$$

$$u_2(x_1,x_2) = \begin{cases} \sqrt{x_1} & \text{for } x_1 > 0; \\ \\ -\sqrt{-x_1} & \text{for } x_1 \leq 0. \end{cases}$$

Both are stationary parabolic minimizers of the total variation flow in the sense of (1.1)–(2.1), over $B_{\frac{1}{2}} \times (0,\infty)$. We establish this for u_1, the analogous statement for u_2 follows similarly. Since $u_1 \in W^{1,1}(B_\rho)$, and is time-independent, one also has $u \in L^1\big(0,T;BV(B_\rho)\big)$. To verify (1.1), one needs to show that

$$\|Du_1\|(B_\rho) \le \frac{1}{T}\int_0^T \|D(u_1+\varphi)(\cdot,t)\|(B_\rho)dt \qquad (*)$$

for all $T>0$, and all $\varphi \in C_o^\infty(B_\rho \times (0,T))$. Let $\mathscr{H}^k(A)$ denote the k-dimensional Hausdorff measure of a Borel set $A \subset \mathbb{R}^N$. One checks that $\mathscr{H}^N([Du_1 = 0]) = 0$ and there exists a closed set $K \subset B_\rho$, such that $\mathscr{H}^{N-1}(K) = 0$ and

$$\int_{B_\rho - K} \frac{Du_1}{|Du_1|}\cdot D\varphi\, dx = 0, \qquad \text{for all } \varphi \in C_o^\infty(B_\rho - K).$$

From this, by Lemma 4 of [22, § 8], for all $\psi \in C_o^\infty(B_\rho)$, one has

$$\|Du_1\|(B_\rho) \le \|D(u_1+\psi)\|(B_\rho),$$

which, in turn, yields (*). The two functions u_1 and u_2 can be regarded as equibounded near the origin. They both satisfy (2.2), and exhibit quite different moduli of continuity at the origin. This occurrence is in line with a remark of Evans ([23]). A sufficiently smooth minimizer of the elliptic functional $\|Du\|(E)$ is a function whose level sets are surfaces of zero mean curvature. Thus, if u is a minimizer, so is $\varphi(u)$ for all continuous monotone functions $\varphi(\cdot)$. This implies that a modulus of continuity cannot be identified solely in terms of an upper bound of u.

5 Singular Parabolic DeGiorgi Classes

Let $\mathscr{C}\big(Q_\rho(\theta)\big)$ denote the class of all non-negative, piecewise smooth, cutoff functions ζ defined in $Q_\rho(\theta)$, vanishing outside B_ρ, such that $\zeta_t \geq 0$ and satisfying

$$|D\zeta| + \zeta_t \in L^\infty\big(Q_\rho(\theta)\big).$$

For a measurable function $u : E_T \to \mathbb{R}$ and $k \in \mathbb{R}$ set

$$(u-k)_\pm = \{\pm(u-k) \wedge 0\}.$$

The singular, parabolic DeGiorgi class $[DG]^\pm(E_T;\gamma)$ is the collection of all measurable maps

$$u \in C_{\rm loc}\big((0,T);L^2_{\rm loc}(E)\big) \cap L^1_{\rm loc}\big(0,T;BV_{\rm loc}(E)\big), \tag{5.1}$$

satisfying

$$\begin{aligned}
&\sup_{t_o-\theta\rho\leq t\leq t_o}\int_{B_\rho(x_o)}(u-k)^2_\pm\zeta(x,t)dx \\
&\qquad\qquad + \int_{t_o-\theta\rho}^{t_o}\|D((u-k)_\pm\zeta)(\tau)\|(B_\rho(x_o))dt \\
&\leq \gamma\iint_{[(x_o,t_o)+Q_\rho(\theta)]}\big[(u-k)_\pm|D\zeta| + (u-k)^2_\pm|\zeta_t|\big]dxdt + \\
&\qquad\qquad + \int_{B_\rho(x_o)}(u-k)^2_\pm\zeta(x,t_o-\theta\rho)dx
\end{aligned} \tag{5.2}$$

for all $[(x_o,t_o)+Q_\rho(\theta)] \subset E_T$, all $k \in \mathbb{R}$, and all $\zeta \in \mathscr{C}([(x_o,t_o)+Q_\rho(\theta)])$, for a given positive constant γ. The singular DeGiorgi classes $[DG](E_T;\gamma)$ are defined as $[DG](E_T;\gamma) = [DG]^+(E_T;\gamma) \cap [DG]^-(E_T;\gamma)$.

6 The Main Result

The main result of this note is that the necessary and sufficient condition of Theorem 2.1 holds for functions $u \in DG(E_T;\gamma) \cap L^\infty_{\rm loc}(E_T)$. Indeed, the proof of Theorem 2.1, only uses

the local integral inequalities (5.2). In particular, the second of (2.1) is not needed.

Proposition 6.1 *Let u in the functional classes (5.1), be a parabolic minimizer of the total variation flow in E_T, in the sense of (1.1), satisfying in addition (2.1). Then $u \in DG(E_T;2)$.*

The proof will be given in Section 12.

Remark 6.1 Note that in the context of $DG(E_T)$ classes, the characteristic condition (2.2), holds with no further requirement that $u_t \in L^1_{\rm loc}(E_T)$. The latter however is needed to cast a parabolic minimizer of the total variation flow into a $DG(E_T)$-class as stated by Proposition 6.1.

7 A Singular Diffusion Equation

Consider formally, the parabolic 1-Laplacian equation

$$u_t - \operatorname{div}\Big(\frac{Du}{|Du|}\Big) = 0 \quad \text{formally in } E_T. \tag{7.1}$$

Let $\mathscr{P}$ be the class of all Lipschitz continuous, non-decreasing functions $p(\cdot)$ defined in $\mathbb{R}$, with p' compactly supported. Denote by $\mathscr{C}(E_T)$ the class of all non-negative functions ζ defined in E_T, such that $\zeta(\cdot,t) \in C^1_o(E)$ for all $t \in (0,T)$, and $0 \le \zeta_t < \infty$ in E_T. A function $u \in C_{\rm loc}\big(0,T;L^1(E)\big)$ is a local solution to (7.1) if

a. $p(u) \in L^1_{\rm loc}\big(0,T;BV(E)\big)$, for all $p \in \mathscr{P}$;

b. there exists a vector valued function $\mathbf{z} \in [L^\infty(E_T)]^N$ with $\|\mathbf{z}\|_{\infty,E} \le 1$, such that $u_t = \operatorname{div}\mathbf{z}$ in $\mathscr{D}'(E_T)$;

c. denoting by $d(\|Dp(u-\ell)\|)$ the measure in E generated by the total variation $\|Dp(u-\ell)\|(E)$

$$\begin{aligned}
&\int_E \Big(\int_0^{u-\ell} p(s)ds\Big)\zeta(x,t_2)\,dx + \int_{t_1}^{t_2}\int_E \zeta\, d(\|D(p(u-\ell)\|)dt \\
&\le \int_E \Big(\int_0^{u-\ell} p(s)ds\Big)\zeta(x,t_1)\,dx + \int_{t_1}^{t_2}\int_E \Big(\int_0^{u-\ell} p(s)ds\Big)\zeta_t dxdt \qquad (7.2)\\
&\quad - \int_{t_1}^{t_2}\int_E \mathbf{z}\cdot D\zeta\, p(u-\ell)dxdt
\end{aligned}$$

for all $\ell \in \mathbb{R}$, all $p \in \mathscr{P}$, all $\zeta \in \mathscr{C}(E_T)$ and all $[t_1,t_2] \subset (0,T)$. The notion is a local version of a global one introduced in [24, Chapter 3]. Similar notions are in [24, 25, 26, 27], associated with issues of existence for the Cauchy problem and boundary value problems associated with (7.1). The notion of solution in [25], called *variational*, is different and closely related to the variational integrals (1.1).

Our results are local in nature and disengaged from any initial or boundary conditions. Let u be a local solution to (7.1) in the indicated sense, which in addition is locally bounded in E_T. In (7.2) take $\ell = 0$, and $p_\pm(u) = \pm(u-k)_\pm$. Since $u \in L^\infty_{\rm loc}(E_T)$ one verifies that $p_\pm \in \mathscr{P}$. Standard calculations then yield that u is in the DeGiorgi classes $[DG]^\pm(E;\gamma)$, for some fixed $\gamma > 0$. As a consequence, we have the following:

Corollary 7.1 *Let $u \in L^\infty_{\rm loc}(E_T)$ be a local solution to (7.1), in E_T, in the sense* **(a)-(c)** *above. Then, u is continuous at some $(x_o,t_o) \in E_T$, if and only if (2.2) holds true.*

8 Proof of the Necessary Condition

Let $u \in [DG](E_T;\gamma)$ be continuous at $(x_o,t_o) \in E_T$, which we may take as the origin of $\mathbb{R}^{N+1}$, and may assume $u(0,0) = 0$. In $(5.2)_+$ for $(u-k)_+$, take $\theta = 1$ and $k = 0$. Let also $\zeta \in \mathscr{C}(Q_{2\rho})$ be such that $\zeta(\cdot,-2\rho) = 0$, such that $\zeta = 1$ on $Q_{\frac{3}{2}\rho}$, and

$$|D\zeta| + \zeta_t \le \frac{3}{\rho}.$$

Repeat the same choices in $(5.2)_-$ for $(u-k)_-$. Adding the resulting inequalities gives

$$\frac{\rho}{|Q_\rho|}\int_{-2\rho}^{0}\|D(u\zeta)(\cdot,t)\|(B_{2\rho})dt \le 2^{N+1}\gamma\iint_{Q_{2\rho}}\big(u+u^2\big)dxdt. \tag{8.1}$$

Since the total variation $\|Dw\|$ of a function $w \in BV$ can be seen as a measure (see, for example, [28, Chapter 1, § 1]), we have

$$\frac{\rho}{|Q_\rho|}\int_{-\rho}^{0}\|D(u\zeta)(\cdot,t)\|(B_{\rho})dt \le \frac{\rho}{|Q_\rho|}\int_{-2\rho}^{0}\|D(u\zeta)(\cdot,t)\|(B_{2\rho})dt;$$

on the other hand, $u\zeta \equiv u$ in $Q_{\frac{3}{2}\rho} \supset Q_\rho$, and therefore we conclude

$$\frac{\rho}{|Q_\rho|}\int_{-\rho}^{0}\|Du(\cdot,t)\|(B_{\rho})dt \le 2^{N+1}\gamma\iint_{Q_{2\rho}}\big(u+u^2\big)dxdt.$$

The right-hand side tends to zero as $\rho \to 0$, thereby implying the necessary condition of Theorem 2.1. ∎

9 A DeGiorgi Type Lemma

For a fixed cylinder $[(y,s)+Q_{2\rho}(\theta)] \subset E_T$, denote by $\mu_\pm$ and ω, non-negative numbers such that

$$\mu_+ \ge \operatorname*{ess\,sup}_{[(y,s)+Q_{2\rho}(\theta)]} u, \quad \mu_- \le \operatorname*{ess\,inf}_{[(y,s)+Q_{2\rho}(\theta)]} u, \quad \omega \ge \mu_+ - \mu_-. \tag{9.1}$$

Let $\xi \in (0,\frac{1}{2}]$ be fixed and let $\theta = 2\xi\omega$. This is an intrinsic cylinder in that its length $\theta\rho$ depends on the oscillation of u within it. We assume momentarily that the indicated choice of parameters can be effected.

Lemma 9.1 *Let u belong to $[DG]^-(E_T,\gamma)$. There exists a number ν_- depending on N, and γ only, such that if*

$$\big|[u \le \mu_- + \xi\omega] \cap [(y,s)+Q_{2\rho}(\theta)]\big| \le \nu_-|Q_{2\rho}(\theta)|, \tag{9.2}$$

then

$$u \geq \mu_- + \tfrac{1}{2}\xi\omega \quad \text{a.e. in } \big[(y,s)+Q_\rho(\theta)\big]. \tag{9.3}$$

Likewise, if u belongs to $[DG]^+(E_T,\gamma)$*, there exists a number* ν_+ *depending on N, and* γ *only, such that if*

$$\big|[u \geq \mu_+ - \xi\omega] \cap [(y,s)+Q_{2\rho}(\theta)]\big| \leq \nu_+ |Q_{2\rho}(\theta)|, \tag{9.4}$$

then

$$u \leq \mu_+ - \tfrac{1}{2}\xi\omega \quad \text{a.e. in } \big[(y,s)+Q_\rho(\theta)\big]. \tag{9.5}$$

Proof: We prove (9.2)–(9.3), the proof for (9.4)–(9.5) being similar. We may assume $(y,s)=(0,0)$ and for $n=0,1,\dots$, set

$$\rho_n = \rho + \frac{\rho}{2^n}, \qquad B_n = B_{\rho_n}, \qquad Q_n = B_n \times (-\theta\rho_n, 0].$$

Apply $(5.2)_-$ over B_n and Q_n to $(u-k_n)_-$, for the levels

$$k_n = \mu_- + \xi_n\omega \qquad \text{where} \qquad \xi_n = \frac{1}{2}\xi + \frac{1}{2^{n+1}}\xi.$$

The cutoff function ζ is taken of the form $\zeta(x,t)=\zeta_1(x)\zeta_2(t)$, where

$$\zeta_1 = \begin{cases} 1 & \text{in } B_{n+1} \\ \\ 0 & \text{in } \mathbb{R}^N - B_n \end{cases} \qquad |D\zeta_1| \leq \frac{1}{\rho_n - \rho_{n+1}} = \frac{2^{n+1}}{\rho}$$

$$\zeta_2 = \begin{cases} 0 & \text{for } t < -\theta\rho_n \\ \\ 1 & \text{for } t \geq -\theta\rho_{n+1} \end{cases} \qquad 0 \leq \zeta_{2,t} \leq \frac{1}{\theta(\rho_n - \rho_{n+1})} = \frac{2^{(n+1)}}{\theta\rho}.$$

Inequality $(5.2)_-$ with these stipulations yields

$$\begin{aligned}
&\operatorname*{ess\,sup}_{-\theta\rho_n<t<0}\int_{B_n}(u-k_n)_-^2\zeta(x,t)dx+\int_{-\theta\rho_n}^0\|D(u-k_n)_-\zeta\|(B_n)dt\\
&\le\gamma\frac{2^n}{\rho}\left(\iint_{Q_n}(u-k_n)_-dxdt+\frac{1}{\theta}\iint_{Q_n}(u-k_n)_-^2dxdt\right)\\
&\le\gamma\frac{2^n(\xi\omega)}{\rho}|[u<k_n]\cap Q_n|.
\end{aligned}$$

By the embedding Proposition 4.1 of [29, Preliminaries]

$$\begin{aligned}
\iint_{Q_n}[(u-k_n)_-\zeta]^{\frac{N+2}{N}}dxdt&\le\int_{-\theta\rho_n}^0\|D[(u-k_n)_-\zeta]\|(B_n)dt\\
&\quad\times\left(\operatorname*{ess\,sup}_{-\theta\rho_n<t<0}\int_{B_n}[(u-k_n)_-\zeta(x,t)]^2dx\right)^{\frac{1}{N}}\\
&\le\gamma\left(\frac{2^n}{\rho}\xi\omega\right)^{\frac{N+1}{N}}|[u<k_n]\cap Q_n|^{\frac{N+1}{N}}.
\end{aligned}$$

Estimate below

$$\iint_{Q_n}[(u-k_n)_-\zeta]^{\frac{N+2}{N}}dxdt\ge\left(\frac{\xi\omega}{2^{n+2}}\right)^{\frac{N+2}{N}}|[u<k_{n+1}]\cap Q_{n+1}|$$

and set

$$Y_n=\frac{|[u<k_n]\cap Q_n|}{|Q_n|}.$$

Then

$$Y_{n+1}\le\gamma b^nY_n^{1+\frac{1}{N}}$$

where

$$b=2^{\frac{1}{N}[3N+4]}.$$

By Lemma 5.1 of [29, Preliminaries], $\{Y_n\}\to 0$ as $n\to\infty$, provided

$$Y_o\le\gamma^{-N}b^{-N^2}\stackrel{\text{def}}{=}\nu_-.$$

The proof of (9.4)–(9.5) is almost identical. One starts from inequalities $(5.2)_+$ written for the truncated functions

$$(u-k_n)_+ \qquad \text{with} \qquad k_n = \mu_+ - \xi_n \omega$$

for the same choice of ξ_n. ■

10 A Time Expansion of Positivity

For a fixed cylinder

$$[(y,s)+Q_{2\rho}^+(\theta)] = B_{2\rho}(y)\times(s,s+\theta\rho)\subset E_T,$$

denote by $\mu_\pm$ and ω, non-negative numbers satisfying the analog of (9.1). Let also $\xi \in (0,1)$ be a fixed parameter. The value of θ will be determined by the proof; we momentarily assume that such a choice can be done.

Lemma 10.1 *Let $u \in [DG]^-(E_T,\gamma)$ and assume that for some $(y,s)\in E_T$ and some $\rho>0$*

$$\big|[u(\cdot,s)\geq \mu_- + \xi\,\omega]\cap B_\rho(y)\big| \geq \tfrac{1}{2}\big|B_\rho(y)\big|.$$

Then, there exist δ and ε in $(0,1)$, depending only on N, γ, and independent of ξ, such that

$$\big|[u(\cdot,t)>\mu_- + \varepsilon\xi\,\omega]\cap B_\rho(y)\big| \geq \tfrac{1}{4}|B_\rho| \quad \textit{for all } t\in\big(s,s+\delta(\xi\,\omega)\rho\big].$$

Proof: Assume $(y,s)=(0,0)$ and for $k>0$ and $t>0$ set

$$A_{k,\rho}(t) = [u(\cdot,t)<k]\cap B_\rho.$$

The assumption implies

$$|A_{\mu_-+\xi\omega,\rho}(0)| \le \tfrac{1}{2}|B_\rho|. \tag{10.1}$$

Write down inequalities $(5.2)_-$ for the truncated functions $(u-(\mu_-+\xi\omega))_-$, over the cylinder $B_\rho\times(0,\theta\rho]$, where $\theta>0$ is to be chosen. The cutoff function ζ is taken independent of t, non-negative, and such that

$$\zeta = 1 \quad \text{on } B_{(1-\sigma)\rho}, \quad \text{and} \quad |D\zeta| \le \frac{1}{\sigma\rho},$$

where $\sigma\in(0,1)$ is to be chosen. Discarding the non-negative term containing $D(u-(\mu_-+\xi\omega))_-$ on the left-hand side, these inequalities yield

$$\begin{aligned}\int_{B_{(1-\sigma)\rho}}(u-(\mu_-+\xi\omega))_-^2(x,t)dx &\le \int_{B_\rho}(u-(\mu_-+\xi\omega))_-^2(x,0)dx\\ &\quad+\frac{\gamma}{\sigma\rho}\int_0^{\theta\rho}\int_{B_\rho}(u-(\mu_-+\xi\omega))_-dxdt\\ &\le(\xi\omega)^2\Big[\frac{1}{2}+\gamma\frac{\theta}{\sigma(\xi\omega)}\Big]|B_\rho|\end{aligned}$$

for all $t\in(0,\theta\rho]$, where we have enforced (10.1). The left-hand side is estimated below by

$$\begin{aligned}&\int_{B_{(1-\sigma)\rho}}(u-(\mu_-+\xi\omega))_-^2(x,t)dx\\ &\ge\int_{B_{(1-\sigma)\rho}\cap[u<\mu_-+\varepsilon\xi\omega]}(u-(\mu_-+\xi\omega))_-^2(x,t)dx\\ &\ge(\xi\omega)^2(1-\varepsilon)^2|A_{\mu_-+\varepsilon\xi\omega,(1-\sigma)\rho}(t)|\end{aligned}$$

where $\varepsilon \in (0,1)$ is to be chosen. Next, estimate

$$\begin{aligned}|A_{\mu_-+\varepsilon\xi\omega,\rho}(t)| &= |A_{\mu_-+\varepsilon\xi\omega,(1-\sigma)\rho}(t) \cup (A_{\mu_-+\varepsilon\xi\omega,\rho}(t) - A_{\mu_-+\varepsilon\xi\omega,(1-\sigma)\rho}(t))| \\ &\le |A_{\mu_-+\varepsilon\xi\omega,(1-\sigma)\rho}(t)| + |B_\rho - B_{(1-\sigma)\rho}| \\ &\le |A_{\mu_-+\varepsilon\xi\omega,(1-\sigma)\rho}(t)| + N\sigma|B_\rho|.\end{aligned}$$

Combining these estimates gives

$$\begin{aligned}|A_{\mu_-+\varepsilon\xi\omega,\rho}(t)| &\le \frac{1}{(\xi\omega)^2(1-\varepsilon)^2}\int_{B_{(1-\sigma)\rho}} (u-(\mu_-+\xi\omega))_-^2(x,t)dx + N\sigma|B_\rho| \\ &\le \frac{1}{(1-\varepsilon)^2}\Big[\frac{1}{2} + \frac{\gamma\theta}{\sigma(\xi\omega)} + N\sigma\Big]|B_\rho|.\end{aligned}$$

Choose $\theta = \delta(\xi\omega)$ and then set

$$\sigma = \frac{1}{16N}, \qquad \varepsilon \le \frac{1}{32}, \qquad \delta = \frac{1}{2^8\gamma N}. \tag{10.2}$$

This proves the lemma. ■

11 Proof of the Sufficient Part of the Theorem

Having fixed $(x_o,t_o) \in E_T$ assume it coincides with the origin of $\mathbb{R}^{N+1}$ and let $\rho > 0$ be so small that $Q_\rho \subset E_T$. Set

$$\mu_+ = \operatorname*{ess\,sup}_{Q_\rho} u, \quad \mu_- = \operatorname*{ess\,inf}_{Q_\rho} u, \quad \omega = \mu_+ - \mu_- = \operatorname*{ess\,osc}_{Q_\rho} u.$$

Without loss of generality, we may assume that $\omega \le 1$ so that

$$Q_\rho(\omega) = B_\rho \times (-\omega\rho, 0] \subset Q_\rho \subset E_T$$

and

$$\operatorname*{ess\,osc}_{Q_\rho(\omega)} u \le \omega.$$

If u were not continuous at (x_o,t_o), there would exist $\rho_o>0$ and $\omega_o>0$, such that

$$\omega_\rho = \operatorname*{ess\,osc}_{Q_\rho} u \ge \omega_o > 0 \quad \text{for all } \rho \le \rho_o. \tag{11.1}$$

Let δ be determined from the last of (10.2). At the time level $t=-\delta\omega\rho$, either

$$\begin{aligned}
&\big|\big[u(\cdot,-\delta\omega\rho) \ge \mu_- + \tfrac{1}{2}\omega\big]\cap B_\rho\big| \ge \tfrac{1}{2}|B_\rho|, \quad \text{or}\\
&\big|\big[u(\cdot,-\delta\omega\rho) \le \mu_+ - \tfrac{1}{2}\omega\big]\cap B_\rho\big| \ge \tfrac{1}{2}|B_\rho|.
\end{aligned}$$

Assuming the former holds, by Lemma 10.1

$$\big|\big[u(\cdot,t) > \mu_- + \tfrac{1}{64}\omega\big]\cap B_\rho\big| \ge \tfrac{1}{4}|B_\rho| \quad \text{for all } t\in(-\delta\omega\rho,0].$$

Let $2\xi = \frac{1}{64}\delta$. Then

$$|[u(\cdot,t) > \mu_- + 2\xi\omega]\cap B_\rho| \ge \tfrac{1}{4}|B_\rho| \quad \text{for all } t\in(-\xi\omega\rho,0]. \tag{11.2}$$

Next, apply the discrete isoperimetric inequality of Lemma 2.2 of [29, Preliminaries] to the function $u(\cdot,t)$, for t in the range $(-\xi\omega\rho,0]$, over the ball B_ρ, for the levels

$$k=\mu_-+\xi\omega \quad \text{and} \quad \ell=\mu_-+2\xi\omega \quad \text{so that} \quad \ell-k=\xi\omega.$$

This inequality is stated and proved in [29] for functions in $W^{1,1}_{\rm loc}(E)$. It continues to hold for $u\in BV_{\rm loc}(E)$, by virtue of the approximation procedure of [20, Theorem 1.17]. Taking also into account (11.2) this gives

$$\xi\omega|[u(\cdot,t)<\mu_-+\xi\omega]\cap B_\rho| \le \gamma\rho\|Du\|([u(\cdot,t)>k]\cap B_\rho).$$

Integrating in dt over the time interval $(-\xi\omega\rho, 0]$, gives

$$\frac{\Big|\big[u < \mu_- + \xi\omega\big] \cap Q_\rho(\xi\omega)\Big|}{\big|Q_\rho(\xi\omega)\big|} \le \frac{\gamma}{(\xi\omega_o)^2}\,\frac{\rho}{|Q_\rho|}\int_{-\rho}^{0} \|Du(\cdot,t)\|(B_\rho)dt.$$

By the assumption, the right-hand side tends to zero as $\rho \searrow 0$. Hence, there exists ρ so small that

$$\frac{\Big|\big[u < \mu_- + \xi\omega\big] \cap Q_\rho(\xi\omega)\Big|}{\big|Q_\rho(\xi\omega)\big|} \le \nu_-$$

where ν_- is the number claimed by Lemma 9.1 for such choice of parameters. The Lemma then implies

$$\operatorname*{ess\,inf}_{Q_{\frac{1}{2}\rho}(\xi\omega)} u \ge \mu_- + \tfrac{1}{2}\xi\omega,$$

and hence

$$\operatorname*{ess\,osc}_{Q_{\frac{1}{2}\rho}(\xi\omega)} u \le \eta\omega \qquad \text{where} \quad \eta = 1 - \tfrac{1}{2}\xi \in (0,1).$$

Setting $\rho_1 = \frac{1}{2}\xi\omega\rho$ gives

$$\omega_{\rho_1} = \operatorname*{ess\,osc}_{Q_{\rho_1}} u \le \eta\omega.$$

Repeat now the same argument starting from the cylinder Q_{ρ_1}, and proceed recursively to generate a decreasing sequence of radii $\{\rho_n\} \to 0$ such that

$$\omega_o \le \operatorname*{ess\,osc}_{Q_{\rho_n}} u \le \eta^n\omega \quad \text{for all } n \in \mathbb{N}. \qquad \blacksquare$$

12 Proof of Proposition 6.1

The proof uses an approximation procedure of [25]. Observe first that the assumption $u_t \in L^1_{\rm loc}(E_T)$ permits to cast (1.1) in the form

$$\|Du(t)\|(E) \le \|D(u+\varphi)(t)\|(E) + \int_E u_t\varphi dx \tag{12.1}$$

for a.e. $t \in (0,T)$ for all

$$\varphi \in BV_{\rm loc}(E) \cap L^\infty_{\rm loc}(E) \quad \text{with } \operatorname{supp}\{\varphi\} \subset E. \tag{12.2}$$

We only prove the estimate for $(u-k)_+$, the one for $(u-k)_-$ being similar. Fix a cylinder

$$\big[(x_o,t_o)+Q_\rho(\theta)\big] \subset E_T.$$

Up to a translation, assume that $(x_o,t_o)=(0,0)$ and fix a time $t \in (-\theta\rho^2,0)$ for which

$$\int_{B_\rho} |u_t(x,t)|dx < \infty, \quad \text{and} \quad u(\cdot,t) \in BV(E) \cap L^\infty(B_\rho).$$

The next approximation procedure is carried out for such t fixed and we write $u(\cdot,t)=u$. By [20, Theorem 1.17], there exists $\{u_j\} \subset C^\infty(B_\rho)$ such that

$$\lim_{j\to\infty} \int_{B_\rho} |u_j-u|dx = 0 \quad \text{and} \quad \|Du\|(E) = \lim_{j\to\infty} \int_E |Du_j|dx. \tag{12.3}$$

Test (12.1) with $\varphi = -\zeta(u-k)_+$, where $\zeta \in \mathscr{C}\big(Q_\rho(\theta)\big)$. This is an admissible choice, since $u \in BV(E) \cap L^\infty(B_\rho)$. Set $\varphi_j = -\zeta(u_j-k)_+$ for $j \in \mathbb{N}$. For a given $\varepsilon > 0$ there exists $j_o \in \mathbb{N}$ such that

$$\int_E |Du_j|dx < \|Du(\cdot,t)\|(E) + \frac{1}{2}\varepsilon \quad \text{for all } j \geq j_o.$$

Here we have used the second of (12.3). By the first, $\{(u_j+\varphi_j)\} \to (u+\varphi)$ in $L^1(E)$. Therefore, for any $\psi \in [C^1_o(E)]^N$ with $\|\psi\| \leq 1$,

$$\begin{aligned}\int_E (u+\varphi)\operatorname{div}\psi\, dx &= \lim_{j\to\infty} \int_E (u_j+\varphi_j)\operatorname{div}\psi\, dx \\ &\leq \liminf_{j\to\infty} \int_E |D(u_j+\varphi_j)|\, dx.\end{aligned}$$

Taking the supremum over all such ψ gives

$$\|D(u+\varphi)(t)\|(E) \le \liminf_{j\to\infty} \int_E |D(u_j+\varphi_j)|\,dx.$$

Therefore, up to redefining j_o we may also assume that

$$\int_E |D(u_j+\varphi_j)|dx \ge \|D(u+\varphi)\|(E) - \frac{1}{2}\varepsilon \quad \text{for all } \ j \ge j_o.$$

Combining the preceding inequalities gives that

$$\begin{aligned}\int_E |Du_j|dx &< \|Du(\cdot,t)\|(E) + \frac{1}{2}\varepsilon \\ &\le \|D(u+\varphi)(\cdot,t)\|(E) + \int_E u_t(\cdot,t)\varphi dx + \frac{1}{2}\varepsilon \\ &\le \int_E |D(u_j+\varphi_j)|dx + \int_E u_t(\cdot,t)\varphi dx + \varepsilon\end{aligned} \tag{12.4}$$

for all $j \ge j_o$. Next, estimate the first integral on the right-hand side as,

$$\begin{aligned}\int_E |D(u_j+\varphi_j)|dx &= \int_E |D(u_j - \zeta(u_j-k)_+)|dx \\ &\le \int_E |Du_j - \zeta D(u_j-k)_+|dx + \int_E |D\zeta|(u_j-k)_+dx \\ &\le \int_E (1-\zeta)|Du_j| + \zeta|Du_j - D(u_j-k)_+|dx + \int_E |D\zeta|(u_j-k)_+dx.\end{aligned}$$

Put this in (12.4), and absorb the first integral on the right-hand side into the left-hand side, to obtain

$$\begin{aligned}\int_E \zeta|D(u_j-k)_+|dx &= \int_E \zeta\left[|Du_j| - |Du_j - D(u_j-k)_+|\right]dx \\ &\le \int_E |D\zeta|(u_j-k)_+dx + \int_E u_t(\cdot,t)\varphi dx + \varepsilon.\end{aligned}$$

From this

$$\int_E |D(\zeta(u_j-k)_+)|dx \le 2\int_E |D\zeta|(u_j-k)_+dx+\int_E u_t(\cdot,t)\varphi dx+\varepsilon.$$

Next let $j\to\infty$, using the lower semicontinuity of the total variation with respect to L^1-convergence. This gives

$$\begin{aligned}\|D(\zeta(u-k)_+)\|(B_\rho) &\le \liminf_{j\to\infty}\int_E |D(\zeta(u_j-k)_+)|dx\\ &\le \lim_{j\to\infty} 2\int_E |D\zeta|(u_j-k)_+dx+\int_E u_t\varphi dx+\varepsilon\\ &= 2\int_E |D\zeta|(u-k)_+dx+\int_E u_t\varphi dx+\varepsilon.\end{aligned}$$

Finally let $\varepsilon\to 0$ and use the definition of φ to get

$$\|D(\zeta(u-k)_+)\|(B_\rho) \le 2\int_{B_\rho} |D\zeta|(u-k)_+dx-\int_{B_\rho}\zeta u_t(u-k)_+dx.$$

To conclude the proof, integrate in dt over $(-\theta\rho,0)$. ■

13 Boundedness of Minimizers

Proposition 13.1 *Let $u:E_T\to\mathbb{R}$ be a parabolic minimizer of the total variation flow in the sense of (1.1). Furthermore, assume that $u\in L^r_{\rm loc}(E_T)$ for some $r>N$, and that it can be constructed as the limit in $L^r_{\rm loc}(E_T)$ of a sequence of parabolic minimizers satisfying (2.1). Then, there exists a positive constant γ depending only upon N,γ,r, such that*

$$\begin{aligned}\sup_{B_\rho(y)\times[s,t]} u_\pm \le \gamma\Big(\frac{\rho}{t-s}\Big)^{\frac{N}{r-N}}\Big(\frac{1}{\rho^N(t-s)}\int_{2s-t}^t\int_{B_{4\rho}(y)} u_\pm^r\,dxd\tau\Big)^{\frac{1}{r-N}}\\ +\gamma\frac{t-s}{\rho}\end{aligned} \tag{13.1}$$

for all cylinders

$$B_{4\rho}(y)\times[s-(t-s),s+(t-s)]\subset E_T.$$

The constant $\gamma(N,\gamma,r)\to\infty$ *as either* $r\to N$, *or* $r\to\infty$.

Remark 13.1 It is not required that the approximations to u satisfy (2.1) uniformly. The latter is only needed to cast a function satisfying (1.1) into a DeGiorgi class. The proof of the proposition only uses such a membership, and turns such a *qualitative*, non-uniform information into the *quantitative* information (13.1).

Proof (of Proposition 13.1). Let $\{u_j\}$ be a sequence of approximating functions to u. Since u_j satisfy (2.1), they belong to the classes $[DG](E_T;2)$, by Proposition 6.1. It will suffice to establish (13.1) for such u_j for a constant γ independent of j. Thus in the calculations below we drop the suffix j from u_j. The proof will be given for non-negative $u\in[DG]^+(E_T;2)$, the proof for the remaining case being identical; it is very similar to the proof of Proposition A.2.1 given in [29, § A.2]. Assume $(y,s)=(0,0)$ and for fixed $\sigma\in(0,1)$ and $n=0,1,2,\dots$ set

$$\begin{aligned}\rho_n&=\sigma\rho+\frac{1-\sigma}{2^n}\rho, &\qquad t_n&=-\sigma t-\frac{1-\sigma}{2^n}t,\\ B_n&=B_{\rho_n}, &\qquad Q_n&=B_n\times(t_n,t).\end{aligned}$$

This is a family of nested and shrinking cylinders with common "vertex" at $(0,t)$, and by construction

$$Q_o=B_\rho\times(-t,t)\quad\text{ and }\quad Q_\infty=B_{\sigma\rho}\times(-\sigma t,t).$$

We have assumed that u can be constructed as the limit in $L^r_{\rm loc}(E_T)$ of a sequence of bounded parabolic minimizers. By working with such approximations, we may assume that u is qualitatively locally bounded. Therefore, set

$$M=\operatorname*{ess\,sup}_{Q_o}\max\{u,0\},\qquad M_\sigma=\operatorname*{ess\,sup}_{Q_\infty}\max\{u,0\}.$$

We first find a relationship between M and M_σ. Denote by ζ a non-negative, piecewise smooth cutoff function in Q_n that equals one on Q_{n+1}, and has the form $\zeta(x,t)=\zeta_1(x)\zeta_2(t)$, where

$$\zeta_1=\begin{cases}1 & \text{in } B_{n+1}\\ 0 & \text{in } \mathbb{R}^N-B_n\end{cases}\qquad |D\zeta_1|\le\frac{2^{n+1}}{(1-\sigma)\rho}$$

$$\zeta_2=\begin{cases}0 & \text{for } t\le t_n\\ 1 & \text{for } t\ge t_{n+1}\end{cases}\qquad 0\le\zeta_{2,t}\le\frac{2^{n+1}}{(1-\sigma)t};$$

introduce the increasing sequence of levels $k_n=k-2^{-n}k$, where $k>0$ is to be chosen, and in $(5.2)_+$, take such a test function, to get

$$\begin{aligned}&\sup_{t_n\le\tau\le t}\int_{B_n}[(u-k_{n+1})_+\zeta]^2(x,\tau)dx+\int_{t_n}^t\|D[(u-k_{n+1})_+\zeta](\cdot,\tau)\|(B_n)\,d\tau\\ &\qquad\le\frac{\gamma 2^n}{(1-\sigma)\rho}\iint_{Q_n}(u-k_{n+1})_+\,dx\,d\tau\\ &\qquad+\frac{\gamma 2^n}{(1-\sigma)t}\iint_{Q_n}(u-k_{n+1})_+^2\,dx\,d\tau.\end{aligned}\tag{13.2}$$

Estimate

$$\begin{aligned}\iint_{Q_n}(u-k_{n+1})_+\,dx\,d\tau&\le\gamma\frac{2^{n(r-1)}}{k^{r-1}}\iint_{Q_n}(u-k_n)_+^r\,dx\,d\tau,\\ \iint_{Q_n}(u-k_{n+1})_+^2\,dx\,d\tau&\le\gamma\frac{2^{n(r-2)}}{k^{r-2}}\iint_{Q_n}(u-k_n)_+^r\,dx\,d\tau.\end{aligned}$$

Taking these estimates into account yields

$$\begin{aligned}&\sup_{t_n<\tau\le t}\int_{B_n}[(u-k_{n+1})_+\zeta]^2(x,\tau)dx+\int_{t_n}^t\|D[(u-k_{n+1})_+\zeta](\cdot,\tau)\|(B_n)\,d\tau\\ &\le\gamma\frac{2^{nr}}{(1-\sigma)t}\Big[\Big(\frac{t}{\rho}\Big)k^{1-r}+\frac{1}{k^{r-2}}\Big]\iint_{Q_n}(u-k_n)_+^r\,dx\,d\tau.\end{aligned}$$

Assuming that $k > \dfrac{t}{\rho}$, this implies

$$\sup_{t_n<\tau\le t}\int_{B_n}[(u-k_{n+1})_+\zeta]^2(x,\tau)dx+\int_{t_n}^{t}\|D[(u-k_{n+1})_+\zeta](\cdot,\tau)\|(B_n)\,d\tau \le \frac{\gamma 2^{nr}}{(1-\sigma)t}\frac{1}{k^{r-2}}\iint_{Q_n}(u-k_n)_+^r dx\,d\tau.$$

Set

$$Y_n=\frac{1}{|Q_n|}\iint_{Q_n}(u-k_n)_+^r dx\,d\tau$$

and estimate

$$Y_{n+1}\le \|u\|^{r-q}_{\infty,Q_o}\Big(\frac{1}{|Q_n|}\iint_{Q_n}(u-k_{n+1})_+^q dx\,d\tau\Big),$$

where $q \overset{\text{def}}{=} \frac{N+2}{N}$. Applying the embedding Proposition 4.1 of [29, Preliminaries], the previous inequality can be rewritten as

$$Y_{n+1}\le \gamma\|u\|^{r-q}_{\infty,Q_o}\Big(\frac{\rho}{t}\Big)\frac{b^n}{(1-\sigma)^{\frac{1}{N}(N+1)}}\frac{1}{k^{(r-2)\frac{N+1}{N}}}Y_n^{1+\frac{1}{N}},$$

where $b=2^{r\frac{N+1}{N}}$. Apply Lemma 5.1 of [29, Preliminaries], and conclude that $Y_n\to 0$ as $n\to+\infty$, provided k is chosen to satisfy

$$Y_o=\iint_{Q_o}u^r dx\,d\tau=\gamma(1-\sigma)^{N+1}\|u\|^{-(r-q)N}_{\infty,Q_o}\Big(\frac{t}{\rho}\Big)^N k^{(r-2)(N+1)},$$

which yields

$$M_\sigma\le\tilde\gamma\frac{M^{\frac{N(r-q)}{(N+1)(r-2)}}}{(1-\sigma)^{\frac{1}{r-2}}}\Big(\frac{\rho}{t}\Big)^{\frac{N}{(N+1)(r-2)}}\Big(\iint_{Q_o}u^r\,dx\,d\tau\Big)^{\frac{1}{(r-2)(N+1)}}.$$

The proof is concluded by the interpolation Lemma 5.2 of [29, Preliminaries]. ■

Chapter 3

p-Parabolic Approximation of Total Variation Flow Solutions

This chapter is presently under review at *Indiana University Mathematics Journal*.

We show that variational solutions to the Cauchy-Dirichlet problem for the total variation flow can be built as the limit of variational solutions to the same problem for the parabolic p–Laplacian.

1 Introduction

Consider a bounded, Lipschitz domain $\Omega \subset \mathbb{R}^N$ and $f : \partial\Omega \to \mathbb{R}$ a continuous function. The problem of minimizing the total variation of the vector-valued measure Du on Ω in the set

$$\left\{u : \ u \in BV(\Omega) \cap C(\bar{\Omega}), \ u = f \quad \text{on} \ \ \partial\Omega\right\}$$

has been studied in detail in [30]. Minimizers of the above problem are called *functions of least gradient*.

In [31] Juutinen proves that the unique function of least gradient u built in [30] is the uniform limit as $p \searrow 1$ of u_p, the unique p-harmonic function in Ω with Dirichlet datum f, that is, u_p is the solution to

$$\begin{cases} \Delta_p u_p = 0 & \text{in} \ \ \Omega, \\ u_p = f & \text{on} \ \ \partial\Omega. \end{cases}$$

As a consequence, he obtains that functions of least gradient satisfy

$$\Delta_1 u = 0$$

in the viscosity sense. Hence, functions of least gradient are viscosity solutions to the 1-laplacian equation. However, as pointed out in [31], the converse is not true: viscosity

solutions to the 1-laplacian are not necessarily least gradient functions. The connection between least gradient functions and proper solutions to the 1-laplacian is studied, for example, in [32].

The approximation of proper solutions to the 1-laplacian in terms of solutions to the p-Laplacian as $p \to 1$ has been widely studied in the last years: without pretending to collect all the relevant contributions to this issue, the interested reader can refer, for example, to [33, 34, 35, 36, 37] and the references therein. More recently, anisotropic least gradient problems, as in [38], have been dealt with too.

Motivated by the previous result, it is therefore natural to consider the following problem, which at this stage we state in a purely formal way.

Problem 1 *Let $T > 0$ and u_p be a solution to the Cauchy-Dirichlet Problem for the parabolic p-laplacian*

$$\begin{cases} \partial_t u - \operatorname{div}\left(|Du|^{p-2}Du\right) = 0 & \text{in } \Omega \times (0,T), \\ u = u_o & \text{on } \partial_{\mathscr{P}}(\Omega \times (0,T)), \end{cases}$$

and let $p \searrow 1$. One would like to obtain in this way a solution u_1 to the Cauchy-Dirichlet Problem for the total variation flow

$$\begin{cases} \partial_t u - \operatorname{div}\left(\frac{Du}{|Du|}\right) = 0 & \text{in } \Omega \times (0,T), \\ u = u_o & \text{on } \partial_{\mathscr{P}}(\Omega \times (0,T)). \end{cases}$$

Is this indeed the case?

A first important issue in the problem stated above concerns the topology. In [31] both u_p and u_1 are continuous and therefore the topology used is the one of the local uniform convergence. Here, we cannot assume in general continuity for solutions (a necessary and sufficient condition for continuity at a point is considered in [8]), and therefore, a different topology is needed, with the further requirement that it must also be shared both by u_p and u_1.

Another question, which is closely connected and somehow contributes to define the right topology, is a precise definition of solutions, both for the parabolic p-laplacian and for the total variation flow. There is a huge amount of literature that is concerned with the total variation flow, and contributions have been given by different authors. The interested reader can refer, for example, to [39, 24] and the list of references therein. Directly connected to the Cauchy-Dirichlet Problem we address here, is [40]. As for the elliptic framework, the anisotropic total variation flow has been considered too, both in $\mathbb{R}^N$ and in a bounded domain with proper boundary conditions (see, for example, [41]).

However, an important remark is due here: the notions of solution considered in [24], and the corresponding existence and uniqueness results, are based on the so-called *Anzellotti-pairing* (see [42], and also [43]). Moreover, one of the common features of the before-mentioned existence and uniqueness contributions, lies in the strategy of proof, based on nonlinear semi-group theory, in particular on techniques of completely accretive operators and the Crandall–Liggett semigroup generation theorem.

Recently a different approach has been developed by Bögelein, Duzaar and Marcellini in [44]–[25] (see also [26] for time-dependent boundary data), in turn based on previous results of [27]. In these works

1. The Anzellotti-pairing plays no role;

2. The approach is purely variational, and avoids the use of semi-group theory. Under this point of view, it is closer in spirit to the notion of parabolic minimizers of integral functionals with linear growth (parabolic minimizers were originally defined in [10]).

It turns out that the notion of solution given in [44]–[25] gives a natural framework to deal with Problem 1, and that is precisely what we will rely on in these notes.

In the following, by $B_r(x)$ we denote the euclidean ball of radius r centered at x; unless otherwise stated, $\Omega \subset \mathbb{R}^N$ will always be a bounded, convex domain with a compact boundary, which satisfies two further requirements:

(B1) It is of class C^1, that is, there exist a positive ρ and an open, locally finite covering $\{B_\rho(x_j)\}$ of $\partial\Omega$ such that for all $x_j \in \partial\Omega$ the portion of $\partial\Omega$ within the ball $B_\rho(x_j)$ can be represented, in a local system of coordinates with the origin at x_j, as the graph of function f_j of class C^1 in a neighborhood of the origin of the new local coordinates and such that $f_j(0) = 0$ and $Df_j(0) = 0$. Denote by K_j the $(N-1)$-dimensional domain where f_j is defined and set

$$\|\partial\Omega\|_1 = \sup_j \max_{K_j} |Df_j|.$$

This quantity depends upon the choice of the covering $\{B_\rho(x_j)\}$. However, having fixed one such covering, it is invariant under homothetic transformations of the coordinates. In particular it does not depend upon the size of Ω.

(B2) It has the segment property, namely there exist a locally finite, open covering of $\partial\Omega$ with balls $\{B_t(x_j)\}$, a corresponding sequence of unit vectors $\mathbf{n}_j$ and a number $t^* \in (0,1)$, such that

$$x \in \bar{\Omega} \cap B_t(x_j) \;\Rightarrow\; x + t\mathbf{n}_j \in \Omega \text{ for all } t \in (0,t^*).$$

These properties are widely used in the literature, but sometimes the same definition refers to slightly different notions. That is why we have given here the full statement.

By [45, Chapter 8, Proposition 18.1], these assumptions on $\partial\Omega$ ensure that Ω is an extension domain. This fact is going to play a central role for the datum u_o: indeed, u_o is originally given in Ω, but is then extended to $\Omega^* \supsetneq \Omega$ whenever necessary. Moreover, it is straightforward to check that $\partial\Omega$ is uniformly Lipschitz as defined in [46, Definition 12.10].

For any $T > 0$, we let $\Omega_T = \Omega \times (0,T]$, and $\Omega_\infty = \Omega \times (0,\infty)$. For any measurable set $E \subset \mathbb{R}^N$, $|E|$ denotes the Lebesgue measure of such a set. Finally, we take $1 < p < 2$.

1.1 Variational Solutions to the Parabolic p-Laplacian

For a given $u_o \in W^{1,p}(\Omega)$, we define

$$W^{1,p}_{u_o}(\Omega) = \left\{ u_o + v \,|\, v \in \mathring{W}^{1,p}(\Omega) \right\}$$

Definition 1.1 *Let $1 < p < 2$. Given a Cauchy-Dirichlet datum $u_o \in W^{1,p}(\Omega) \cap L^2(\Omega)$, we say a measurable map $u : \Omega_\infty \to \mathbb{R}^N$ in the class*

$$u \in L^p\left(0,T; W^{1,p}_{u_o}(\Omega)\right) \cap C^0\left([0,T]; L^2(\Omega)\right) \qquad \text{for any } T > 0 \tag{1.1}$$

is a variational solution associated to the Cauchy-Dirichlet Problem

$$\begin{cases} \partial_t u - \operatorname{div}\left(|Du|^{p-2}Du\right) = 0 & \text{in } \Omega_\infty \\ u = u_o & \text{on } \partial_{\mathscr{P}}\Omega_\infty \end{cases} \tag{1.2}$$

if and only if the variational inequality

$$\begin{aligned} \frac{1}{p}\int_0^T \int_\Omega |Du|^p \, dxdt \le \int_0^T \int_\Omega \left[\partial_t v\,(v-u) + \frac{1}{p}|Dv|^p \right] dxdt \\ + \frac{1}{2}\left\| v(\cdot;0) - u_o \right\|^2_{L^2(\Omega)} - \frac{1}{2}\left\| (v-u)(\cdot;T) \right\|^2_{L^2(\Omega)} \end{aligned} \tag{1.3}$$

holds true, when $T > 0$, and $v \in L^p\left(0,T; W^{1,p}_{u_o}(\Omega)\right)$ with $\partial_t v \in L^2(\Omega_T)$, and $v(\cdot,0) \in L^2(\Omega)$.

The chief result of [44] is the following.

Proposition 1.1 *There exists a* unique *variational solution u in the sense of Definition 1.1. Moreover, this solution satisfies*

$$\partial_t u \in L^2(\Omega_\infty) \text{ and } u \in C^{0,1/2}\left([0,T]; L^2(\Omega)\right) \quad \forall T > 0$$

with the quantitative bounds

$$\int_0^\infty \int_\Omega |\partial_t u|^2 \, dxdt \leq \frac{1}{p} \int_\Omega |Du_o|^p \, dxdt. \tag{1.4}$$

For any $0 \leq t_1 < t_2 < \infty$*, we also have*

$$\frac{1}{t_2 - t_1} \int_{t_1}^{t_2} \int_\Omega |Du|^p \, dxdt \leq 2e \int_\Omega |Du_o|^p \, dxdt. \tag{1.5}$$

With the *a priori* observation that $\partial_t u \in L^2(\Omega_T)$, we have the following equivalent formulation of (1.3).

Corollary 1.1 *Subject to the class restriction given in* (1.1)*, u is a variational solution for the parabolic p-Laplacian if and only if we have*

$$\frac{1}{p} \int_0^T \int_\Omega |Du|^p \, dxdt \leq \int_{\Omega_T} \partial_t u \, (v-u) \, dxdt + \frac{1}{p} \int_{\Omega_T} |Dv|^p \, dxdt \tag{1.6}$$

for $v \in L^p\left(0,T; W^{1,p}_{u_o}(\Omega)\right) \cap L^2(\Omega_T)$

Proof - In (1.3) let $v \in L^p\left(0,T; W^{1,p}_{u_o}(\Omega)\right)$ with $\partial_t v \in L^2(\Omega_T)$, and $v(\cdot,0) \in L^2(\Omega)$. After adding and subtracting the time derivative $\partial_t u$, write

$$\begin{aligned} \frac{1}{p} \int_0^T \int_\Omega |Du|^p \, dxdt \leq & \int_{\Omega_T} \partial_t u \, (v-u) \, dxdt + \int_{\Omega_T} \partial_t \, (v-u) \, (v-u) \, dxdt \\ & + \frac{1}{p} \int_0^T \int_\Omega |Dv|^p \, dxdt \\ & + \frac{1}{2} \|v(\cdot,0) - u_o\|^2_{L^2(\Omega)} - \frac{1}{2} \|(v-u)(\cdot,T)\|^2_{L^2(\Omega)}. \end{aligned}$$

Integrating the total time derivative cancels with the boundary data and returns the desired inequality

$$\frac{1}{p} \int_0^T \int_\Omega |Du|^p \, dxdt \leq \int_{\Omega_T} \partial_t u \, (v-u) \, dxdt + \frac{1}{p} \int_{\Omega_T} |Dv|^p \, dxdt.$$

In order to conclude, we need to enlarge the test class: given an arbitrary function $v \in L^p\left(0,T;W^{1,p}_{u_o}(\Omega)\right)$, we proceed with a smooth mollification in time over Ω_T and approximate it in the norm of $L^p\left(0,T;W^{1,p}_{u_o}(\Omega)\right)$. This is all that is needed in order to give (1.6) for the larger test class.

For the reverse equivalence, now restrict to those v which satisfy $\partial_t v \in L^2(\Omega_T)$, $v(\cdot,0) \in L^2(\Omega)$, and run a similar add and subtract program. ■

As mentioned before, Ω is an extension domain. Therefore, given $u_o \in W^{1,p}(\Omega)$ for any $1 \le p \le \infty$, there exists $\mathscr{E}(u_o) \in W^{1,p}(\mathbb{R}^N)$ such that

$$\begin{aligned}
&\mathscr{E}(u_o)(x) = u_o(x) \text{ for a.e. } x \in \Omega,\\
&\|\mathscr{E}(u_o)\|_{L^p(\mathbb{R}^N)} \le \gamma(1+\|\partial\Omega\|_1)\|u_o\|_{L^p(\Omega},\\
&\|D\mathscr{E}(u_o)\|_{L^p(\mathbb{R}^N)} \le \gamma(1+\|\partial\Omega\|_1)\left(\|Du_o\|_{L^p(\Omega)} + \frac{1}{t}\|u_o\|_{L^p(\Omega)}\right),
\end{aligned}$$

where $t \in (0,1)$ depends on the covering required by (**B1**)–(**B2**), and γ depends on N, p_o, and the covering. The extension of u_o from Ω to $\mathbb{R}^N$ is obviously not unique: in the following, we assume that we build one such extension, and then we work with it: in this sense, we will talk of *the* extension; moreover, for simplicity, we denote $\mathscr{E}(u_o)$ with u_o.

Consider

$$u \in L^p\left(0,T;W^{1,p}_{u_o}(\Omega)\right) \cap C^0\left([0,T];L^2(\Omega)\right)$$

and the extension of u_o from $W^{1,p}(\Omega)$ to $W^{1,p}(\mathbb{R}^N)$. It is obvious that $u_o \in W^{1,p}(\Omega^* \setminus \bar{\Omega})$ for a bounded open set $\Omega^* \supsetneq \Omega$. We define the *extension* $\tilde{u}(x,t)$ of $u(x,t)$ as

$$\tilde{u}(x,t) \stackrel{\text{def}}{=} \begin{cases} u(x,t) & \text{if } (x,t) \in \Omega_T,\\ u_o(x) & \text{if } (x,t) \in (\Omega^* \setminus \bar{\Omega}) \times (0,T]. \end{cases} \tag{1.7}$$

Since

$$\text{tr}\Big|_{\partial\Omega} u(\cdot,t) = \text{tr}\Big|_{\partial\Omega} u_o,$$

it is straightforward to check that $\tilde{u} \in L^p\left(0,T;W^{1,p}(\Omega^*)\right)$ (see also [46, Exercise 15.26]). We now re-define the space $W^{1,p}_{u_o}(\Omega)$.

Definition 1.2 *Given a function $u_o \in W^{1,p}(\Omega)$, consider the extension of u_o from $W^{1,p}(\Omega)$ to $W^{1,p}(\mathbb{R}^N)$, which we continue to denote by u_o. For a bounded open set $\Omega^* \supsetneq \Omega$, we let*

$$W^{1,p}_{u_o}(\Omega) = \left\{ v \in W^{1,p}(\Omega^*) \,|\, v = u_o \text{ in } \Omega^* \setminus \Omega \right\}.$$

Remark 1.1 We restrict from $\mathbb{R}^N$ to Ω^*, mainly because it is easier to work in a bounded domain.

Remark 1.2 Since Ω is an extension domain, the restriction of functions in $W^{1,p}_{u_o}(\Omega)$ to Ω is precisely the set of functions in $W^{1,p}(\Omega)$, whose trace on $\partial\Omega$ matches that of u_o.

Proposition 1.2 *Fix a bounded open set $\Omega^* \supsetneq \Omega$. Subject to the class restriction given in Definition 1.1, and further assuming that $\partial_t u \in L^2(\Omega_T)$, u is a solution to the parabolic variational problem (1.6) if and only if its extension $\tilde{u}$ satisfies*

$$\frac{1}{p}\int_{\Omega^*_T} |D\tilde{u}|^p \, dxdt \leq \int_{\Omega^*_T} \partial_t \tilde{u}\,(v-\tilde{u})\, dxdt + \frac{1}{p}\int_{\Omega^*_T} |Dv|^p \, dxdt \tag{1.8}$$

for all $v \in L^p\left(0,T;W^{1,p}_{u_o}(\Omega)\right) \cap L^2\left(\Omega^*_T\right)$.

Proof - In $\Omega^* \setminus \Omega$ we have $\tilde{u} = v = u_o$ which itself is a function independent of time. Accordingly, to pass from (1.6) to (1.8), one need only add the common term

$$\frac{1}{p}\int_{\Omega^*_T \setminus \Omega_T} |Du_o|^p \, dxdt$$

to both sides. To go in the reverse direction, one need only subtract it. ■

Remark 1.3 It goes without saying, that in the previous result it is of fundamental importance the fact that the boundary datum u_o is time-independent.

1.2 Variational Solutions to the Total Variation Flow

When dealing with parabolic variational inequalities with linear growth, i.e. with $p = 1$ in (1.2), the natural framework is given by functions in $BV(\Omega)$, not in $W^{1,1}(\Omega)$. However, there is an extra difficulty: boundary values of BV-functions are a delicate issue, since the trace operator is not continuous with respect to the weak* convergence in $BV(\Omega)$. We refer to [47, 20] as standard references for functions of bounded variation.

For a given $u_o \in W^{1,p}(\Omega)$, we follow the method used in [44, 25]: consider its extension to $W^{1,p}(\mathbb{R}^N)$, let $\Omega^* \supsetneq \Omega$ be a bounded open set, and define

$$BV_{u_o}(\Omega) = \{v \in BV(\Omega^*) \,|\, v = u_o \text{ in } \Omega^* \setminus \Omega\}.$$

It is through membership in this class that solutions will be said to take the Dirichlet datum u_o. In fact, the *exterior* trace on $\partial\Omega$ of these BV-functions is precisely u_o, see [20, Chapter 2].

It would be preferable to enforce the Dirichlet data using the interior trace on $\partial\Omega$, rather than the exterior one. However, due to the failure of the trace operator to be weak* continuous, working with the interior trace leads to a space which lacks the weak sequential compactness properties needed to pass to the limit.

Consider the following illustrative example. Let $f_n \in BV(-1,1)$ be given by

$$f_n(x) = \begin{cases} n|x| & | \text{ for } |x| \leq \frac{1}{n} \\ 1 & | \text{ for } |x| > \frac{1}{n} \end{cases}$$

This family is equibounded in the norm of $BV(-1,1)$, and its strong limit is 1. However, the trace of $\lim f_n$ does not coincide with the lim trace f_n on $x = 0$. Therefore, one cannot expect that a family of norm-equibounded BV-functions with merely a constant trace preserves that trace in the limit. In our definition of $BV_{u_o}(\Omega)$, this difficulty is bypassed because the

functions are held constant on a full region of space exterior to the domain, rather than just the trace.

It remains to show in which way the total variation $\|Dv\|(\Omega^*)$ for $v \in BV_{u_o}(\Omega)$, is related to the original $\|Dv\|(\Omega)$ for $v \in BV(\Omega)$. As observed in [20, Chapter 14], where this same approach is used in the nonparametric theory of minimal surfaces, for $v \in BV_{u_o}(\Omega)$ and Ω a compact domain with Lipschitz boundary,

$$\int_{\Omega^*} |Dv| = \int_{\Omega} |Dv| + \int_{\partial\Omega} \left|u_o - \mathrm{tr}^- v\right| dH^{N-1} + \int_{\Omega^*\setminus\Omega} |Du_o| \, dx, \tag{1.9}$$

where $\mathrm{tr}^- v$ refers to the interior BV trace of v on $\partial\Omega$. Accordingly, the total variation term in $BV_{u_o}(\Omega)$ is equivalent to the original total variation, with a penalty term measuring the difference between the obtained trace and the intended Dirichlet datum, plus a third term which is the total variation of u_o in $\Omega^*\setminus\Omega$. In our parabolic framework, this final term is a time-independent contribution on both sides of the variational inequality: thus, the arbitrary choice of extension domain Ω^* does not influence the variational problem.

Given $f \in BV(\Omega)$, by $\|Df\|(\Omega)$ we denote the total variation of Df on Ω. Moreover, if we let for simplicity $|f|_{BV(\Omega)} \stackrel{\text{def}}{=} \|Df\|(\Omega)$, as it is well-known, $\|f\|_{BV(\Omega)} \stackrel{\text{def}}{=} \|f\|_{L^1(\Omega)} + |f|_{BV(\Omega)}$. Finally, in this case the concept of variational solutions makes use of the space $L^1_w(0,T;BV_{u_o}(\Omega))$. It consists of those functions $v : [0,T] \to BV_{u_o}(\Omega)$ such that

- $v \in L^1(]0,T[\times\Omega)$;
- the maps $t \in [0,T] \ \to \ \langle Dv(t), \varphi\rangle$ are measurable for every $\varphi \in C^1_o(\Omega)$;
- $\int_0^T \|Dv(\cdot,t)\|(\Omega)\, dt < \infty$.

Definition 1.3 *Let $\frac{2N}{N+1} \le p_o < 2$. Given a Cauchy-Dirichlet datum*

$$u_o \in W^{1,p_o}(\Omega^*),$$

we say a measurable map $u : \Omega_\infty^* \to \mathbb{R}^N$ *in the class*

$$u \in L^1_w(0,T;BV_{u_o}(\Omega)) \cap C^0\left([0,T];L^2(\Omega^*)\right) \quad \text{for any } T>0$$

is a variational solution associated to the Cauchy-Dirichlet Problem for the total variation flow

$$\begin{cases} \partial_t u - \operatorname{div}\left(\frac{Du}{|Du|}\right) = 0 & \text{in } \Omega_\infty \\ u = u_o & \text{on } \partial_{\mathscr{P}}\Omega_\infty \end{cases} \tag{1.10}$$

if and only if the variational inequality

$$\begin{aligned} \int_0^T \|Du(\cdot,t)\|(\Omega^*)\,dt \le \int_0^T \int_{\Omega^*} \partial_t v\,(v-u)\,dxdt + \int_0^T \|Dv(\cdot,t)\|(\Omega^*)\,dt \\ + \frac{1}{2}\|v(\cdot,0)-u_o\|^2_{L^2_2(\Omega^*)} - \frac{1}{2}\|(v-u)(\cdot,T)\|^2_{L^2_2(\Omega^*)} \end{aligned} \tag{1.11}$$

holds true, when $T>0$*, and* $v \in L^1(0,T;\mathrm{BV}_{u_o}(\Omega))$ *with* $\partial_t v \in L^2(\Omega_T^*)$*,* $v(\cdot,0) \in L^2(\Omega^*)$*.*

Since $u_o \in W^{1,p_o}(\Omega^*)$ with $\frac{2N}{N+1} \le p_o < 2$, the Sobolev Embedding Theorem ensures that $u_o \in L^2(\Omega^*)$.

In [25, Theorem 1.2], Boegelein, Duzaar and Marcellini prove that there exists a *unique* variational solution u associated to the Cauchy-Dirichlet Problem (1.10).

However, their definition is slightly different with respect to Definition 1.3. Indeed, they take the test function v in the larger set $L^1_w(0,T;BV_{u_o}(\Omega))$.

Remark 1.4 Just as with the p–Laplacian case, when $\partial_t u$ exists in $L^2(\Omega_T^*)$, the above formulation is equivalent to

$$\int_0^T \|Du(\cdot,t)\|(\Omega^*)\,dt \le \int_0^T \|Dv(\cdot,t)\|(\Omega^*)\,dt + \int_{\Omega_T^*} \partial_t u\,(v-u)\,dxdt \tag{1.12}$$

for any test function v such that $v \in L^1(0,T;\mathrm{BV}_{u_o}(\Omega)) \cap L^2(\Omega_T^*)$.

Remark 1.5 Even though Definition 1.3 does not require anything on $\partial_t u$, nevertheless for the function u_1, which we will build in Theorem 1.1, the time derivative is well-defined, and turns out to be a function in $L^2(\Omega_T^*)$.

In the following, we will also consider the following space.

Definition 1.4 *The set $C^\infty_{o,\gamma,p}(\Omega)$ is the collection of all smooth functions, compactly supported in Ω, whose support is separated from $\partial\Omega$ by distance no less than $\gamma > 0$, endowed with the $W^{1,p}(\Omega)$ norm.*

1.3 The Main Result

As already discussed before, we assume that $\Omega \subset \mathbb{R}^N$ is a bounded, convex domain with a compact boundary, which satisfies conditions (**B1**)–(**B2**).

We let $p_o \in [\frac{2N}{N+1}, 2)$, consider $u_o \in W^{1,p_o}(\Omega)$ and its extension from $W^{1,p_o}(\Omega)$ to $W^{1,p_o}(\mathbb{R}^N)$, which we continue to denote by u_o.

Given a bounded open set $\Omega^* \supsetneq \Omega$, by the Sobolev Embedding Theorem we have that $u_o \in W^{1,p}(\Omega^*) \cap L^2(\Omega^*)$ for any $p \in (1, p_o]$.

Let $\{u_p\}$ be the sequence of the unique variational solutions to the Cauchy-Dirichlet Problem for the parabolic p-laplacian with $p \in (1, p_o]$. We define the *extension* $\tilde{u}_p(x,t)$ of $u_p(x,t)$ as

$$\tilde{u}_p(x,t) \stackrel{\text{def}}{=} \begin{cases} u_p(x,t) & \text{if } (x,t) \in \Omega_T, \\ u_o(x) & \text{if } (x,t) \in (\Omega^* \setminus \bar{\Omega}) \times (0,T]. \end{cases}$$

If we consider the trace on $\partial\Omega$ in the sense of functions in $W^{1,p}$ for $1 < p \leq p_o$, it is straightforward to verify that

$$\text{tr}\Big|_{\partial\Omega} u_p(\cdot,t) = \text{tr}\Big|_{\partial\Omega} u_o.$$

This yields that $\tilde{u}_p \in L^p\left(0,T; W^{1,p}_{u_o}(\Omega)\right) \cap C^0([0,T]; L^2(\Omega^*))$. In the following, for simplicity we continue to denote the extension $\tilde{u}_p$ with u_p.

Theorem 1.1 *Under all the previous assumptions, when $p \to 1$, we have that for any $T > 0$, $u_p \to u_1$ in $L^q(\Omega_T^*)$ for any $1 \leq q < \frac{N}{N-1}$, and $\partial_t u_p \to \partial_t u_1$ in $L^2_w(\Omega_T^*)$, where $u_1 \in L^1_w(0,T;BV_{u_o}(\Omega)) \cap C^0\left([0,T];L^2(\Omega^*)\right)$ is a variational solution to the Cauchy-Dirichlet Problem for the total variation flow.*

As already mentioned before, in [48] solutions are unique. This is an issue we will not deal with here.

1.4 Novelty and Significance

Theorem 1.1 shows that solutions to the Cauchy-Dirichlet problem for the parabolic p-Laplacian tend to a solution to the corresponding problem for the total variation flow. However, given its nature there is also a complementary way of looking at our result; indeed, we are showing that variational solutions to the 1–Laplacian can be built as the limit of solutions to the p–Laplacian, therefore providing an alternative construction, with respect to the one studied in [25, 26].

In [31, Section 4], Juutinen investigates also local convergence properties of p-harmonic functions as $p \to 1$. This is not the case here: local results corresponding to the global statement of Theorem 1.1, are not dealt with here.

Theorem 1.1 represents the main contribution of this work. Its proof relies on a density result, which we are going to present next.

Let $u_o \in L^2(\Omega) \cap W^{1,p}(\Omega)$, and define

$$
\begin{aligned}
u_o + C^\infty_{o,\gamma,p}(\Omega) &\stackrel{\text{def}}{=} \left\{ u_o + v \,|\, v \in C^\infty_{o,\gamma,p}(\Omega) \right\} \\
\left\{ u_o + C^\infty_{o,\gamma,p}(\Omega) \right\}_{\gamma>0} &\stackrel{\text{def}}{=} \bigcup_{\gamma>0} \left(u_o + C^\infty_{o,\gamma,p}(\Omega) \right) \\
\left\{ L^\infty\left(0,T; u_o + C^\infty_{o,\gamma,p}(\Omega)\right) \right\}_{\gamma>0} &\stackrel{\text{def}}{=} \bigcup_{\gamma>0} L^\infty\left(0,T; u_o + C^\infty_{o,\gamma,p}(\Omega)\right).
\end{aligned}
$$

In the sequel, whenever necessary, functions will be extended from Ω to Ω^*, relying on the

corresponding extension of u_o. Then

Theorem 1.2 $\left\{L^\infty\left(0,T;u_o+C^\infty_{o,\gamma,p_o}(\Omega)\right)\right\}_{\gamma>0}\cap L^\infty\left(0,T;L^2(\Omega)\right)$ *is dense in the space* $L^1\left(0,T;BV_{u_o}(\Omega)\right)$.

The chief technical difficulty of these notes is precisely the proof of Theorem 1.2, which requires a delicate approximation procedure, performed in multiple steps. Although here it is instrumental in the proof of the main result, nevertheless, we think that Theorem 1.2 can be of independent interest.

2 Proof of Theorem 1.1 Assuming Theorem 1.2

The compactness estimates that we need in order to pass to the limit in the approximating sequence, basically all follow from estimates (1.4)–(1.5). We work with the p-parametrized family of variational solutions associated to (1.2) for $1 < p \leq p_o$. For the moment, we strictly work inside the domain Ω; a corollary concerning how to pass to the larger domain $\Omega^* \supsetneq \Omega$ will be considered at the end of the section.

Lemma 2.1 *If u_o is such that $\|Du_o\|_{p_o} < \infty$ for some $p_o > 1$, then for $p \in [1, p_o]$,*

$$\frac{1}{p}\int_\Omega |Du_o|^p\,dx < \Gamma, \tag{2.1}$$

where $\Gamma > 0$ is a constant that depends on p_o, $|\Omega|$, $\|Du_o\|_{p_o}$.

Proof - It is a matter of straightforward computations to show that

$$\frac{1}{p}\int_\Omega |Du_o|^p\,dx \leq \frac{1}{p}\|Du_o\|^p_{p_o}|\Omega|^{\frac{p_o-p}{p_o}}. \tag{2.2}$$

Clearly for $p \in [1, p_o]$, the right-hand side may be upper bounded independently of p. ■

As a consequence of the previous result, we have:

Corollary 2.1 *Let $p_o \in (1,2]$, and $u_o \in L^2(\Omega) \cap W^{1,p_o}(\Omega)$. The variational solutions $\{u_p\}_{p<p_o}$ corresponding to the initial datum u_o, and their time derivatives $\{\partial_t u_p\}_{p<p_o}$ are uniformly bounded in $L^2(\Omega_T)$ by a positive constant Γ that depends on p_o, $|\Omega|$, $\|Du_o\|_{p_o,\Omega}$, $\|u_o\|_{2,\Omega}$, T.*

Proof - From (1.4) and (2.1), we conclude $\left\|\partial_t u_p\right\|_2 \leq \Gamma$ is a uniform bound. Now we use that the initial datum is bounded in $L^2(\Omega)$ and proceed with an argument justified up to mollification; for any $t \in (0,T]$

$$\begin{aligned}\int_\Omega \left|u_p(\cdot,t)-u_o\right|^2 dx &= \int_\Omega \left|\int_0^t \partial_\tau u_p d\tau\right|^2 dx = t^2 \int_\Omega \left|\frac{1}{t}\int_0^t \partial_\tau u_p \, d\tau\right|^2 dx \\ &\leq t\int_\Omega \int_0^t |\partial_\tau u_p|^2 \, dx d\tau \leq T\int_{\Omega_T} |\partial_\tau u_p|^2 \, dx d\tau \leq T\,\Gamma.\end{aligned}$$

Conclude using the initial data

$$\begin{aligned}\int_{\Omega_T} u_p^2 \, dx d\tau &= \int_{\Omega_T} \Big(u_o + u_p(\cdot,t) - u_o\Big)^2 dx d\tau \\ &\leq 2\int_{\Omega_T} [|u_o|^2 + \left|u_p(\cdot,t)-u_o\right|^2] dx d\tau \\ &\leq 2T\int_\Omega |u_o|^2 \, dx d\tau + 2T^2\Gamma.\end{aligned}$$

■

Remark 2.1 The above remarks hold merely for a family of initial datum u_o with a common $\|u_o\|_2$ and $\|Du_o\|_{p_o}$ bound.

Remark 2.2 Proceeding in a completely analogous way yields a uniform time continuity estimate

$$\int_\Omega \left|u_p(\cdot,t_2)-u_p(\cdot,t_1)\right|^2 dx \leq (t_2-t_1)\,\Gamma. \tag{2.3}$$

As for the space weak differentiability on time traces, we have the following.

Corollary 2.2 *For the above family* $\left\{u_p\right\}_{p<p_o}$*, the time trace of the gradient satisfies*

$$\left\|Du_p(\cdot,t)\right\|_{1,\Omega} \leq \Gamma. \tag{2.4}$$

Proof - From Jensen's inequality and (1.5), we may write

$$\int_\Omega \left(\frac{1}{h}\int_t^{t+h} |Du_p|\, d\tau\right)^p dx \leq \frac{1}{h}\int_\Omega \int_t^{t+h} \left|Du_p\right|^p d\tau dx \leq 2e\int_\Omega |Du_o|^p\, dx \leq \Gamma.$$

As the limit of Steklov averages gives a possible definition of time trace, we see that the trace of Du_p exists in L^p which, due to Hölder inequality, means that the L^1 norm is also bounded. By enforcing the definition of weak space derivative against a test function independent of time, dividing by h as in Steklov averages, we may conclude that

$$\operatorname{tr} Du_p = D\left[\operatorname{tr} u_p\right]. \qquad \blacksquare$$

We summarize the result of the previous corollaries, and collect our starting compactness estimates.

Lemma 2.2 *Let* $p_o \in (1,2]$*, and* $u_o \in W^{1,p_o}(\Omega)\cap L^2(\Omega)$*. The family of variational solutions* $\left\{u_p\right\}_{p<p_o}$ *to the initial datum* u_o *are uniformly bounded, and satisfy the following uniform estimates:*

$$\left\|u_p\right\|_{2,\Omega_T} \leq \Gamma, \tag{2.5}$$

$$\left\|\partial_t u_p\right\|_{2,\Omega_T} \leq \Gamma, \tag{2.6}$$

$$\left\|Du_p\right\|_{1,\Omega_T} \leq \Gamma, \tag{2.7}$$

$$\left\|Du_p(\cdot,t)\right\|_{1,\Omega} \leq \Gamma. \tag{2.8}$$

2.1 Extracting a Convergent Subsequence

Relying on Lemma 2.2 we can now extract a convergent subsequence, whose limit has several additional regularity features.

Proposition 2.1 *Under the same assumptions of Lemma 2.2 on u_o, for the family $\{u_p\}_{p<p_o}$, there is a subsequence, which we still denote with $\{u_p\}$, such that*

$$u_p(\cdot,t) \to_{L^1(\Omega)} u_1(\cdot,t) \in BV(\Omega) \quad as \quad p \to 1,$$

and the rate of $L^1(\Omega)$ convergence is uniform for all $t \in [0,T]$.

Proof - Using the first two estimates of Lemma 2.2 and a standard trace inequality, we have that $u_p(\cdot,t) \in L^2(\Omega) \subseteq L^1(\Omega)$ and the norms are uniformly bounded by Γ. Coupling this with (2.8), we have

$$\left\|u_p(\cdot,t)\right\|_{\mathrm{BV}(\Omega)} \leq \Gamma \quad \forall t \in [0,T].$$

Moreover, from (2.3) we have that the family of the time traces $\{u_p(\cdot,t)\}$ is equicontinuous in $L^2(\Omega)$, uniformly with respect to p. We can then proceed by the Ascoli-Arzelà Theorem.

Take an enumeration $\{t_i\}$ of all rational times in $[0,T]$. By the Rellich Compactness Theorem, we may take $\{u_{p_1}(\cdot,t_1)\}_{p_1}$ to be a subsequence converging strongly in $L^1(\Omega)$ to a $BV(\Omega)$-function denoted $u_1(\cdot,t_1)$, then $\{u_{p_2}(\cdot,t_2)\}_{p_2}$ to be a subsequence within u_{p_1} converging also at t_2. Continuing $\ldots, \{u_{p_k}(\cdot,t_k)\}_{p_k}, \ldots$ where the $\{p_k\}$-sequence strongly converges for $t_1,\ldots,t_k$. Note that we may pick the sequences so that $\left\|u_1(\cdot,t_k) - u_{p_{k,j}}(\cdot,t_k)\right\|_{L^1(\Omega)} < \frac{1}{j}$.

By the usual diagonalization procedure, we have a subsequence $\{u_p\}_p$ such that

$$u_p(\cdot,t_i) \to_{L^1(\Omega)} u_1(\cdot,t_i) \in BV(\Omega) \quad \forall t_i \in \mathbb{Q}.$$

We claim that this sequence actually converges strongly at any time, and that the rate of convergence is uniform for all t. To show this, we build an ε-net out of the equi-continuity estimate (2.3). For $\varepsilon > 0$ fixed, there exists a *finite* collection of $t_i \in \mathbb{Q}$, such that for any time t fixed, there is a rational number t_i satisfying

$$\left\| u_p(\cdot,t_i) - u_p(\cdot,t) \right\|_{L^1(\Omega)} < \varepsilon \quad \forall\, p \in [1, p_o].$$

Now let $p_1, p_2 \in [1, p_o]$ be given and observe

$$\begin{aligned}
\left\| u_{p_1}(\cdot,t) - u_{p_2}(\cdot,t) \right\|_{L^1(\Omega)} \leq & \left\| u_{p_1}(\cdot,t) - u_{p_1}(\cdot,t_i) \right\|_{L^1(\Omega)} \\
& + \left\| u_{p_1}(\cdot,t_i) - u_{p_2}(\cdot,t_i) \right\|_{L^1(\Omega)} \\
& + \left\| u_{p_2}(\cdot,t_i) - u_{p_2}(\cdot,t) \right\|_{L^1(\Omega)} \\
\leq & 2\varepsilon + \left\| u_{p_1}(\cdot,t_i) - u_{p_2}(\cdot,t_i) \right\|_{L^1(\Omega)}.
\end{aligned}$$

As our ε-net is finite, we have that the second term may be made uniformly smaller than ε.

■

Remark 2.3 Note that $u_1(\cdot,t) \in BV(\Omega)$ because of lower semicontinuity and in particular $\forall t \in (0,T)$, all the BV norms of $u_1(\cdot,t)$ share the same bound Γ.

Remark 2.4 The proof stated all results in the context of $L^1(\Omega)$, but the Rellich Compactness Theorem guarantees strong convergence in $L^q(\Omega)$ for $1 \leq q < \frac{N}{N-1}$. Since the time trace continuity is in $L^2(\Omega)$, the corresponding uniform continuity is inherited for $L^q(\Omega)$ with q in the range $[1, \frac{N}{N-1})$. Thus, the theorem also holds with respect to the $L^q(\Omega)$ strong convergence for $q < 1^*$ in lieu of $L^1(\Omega)$, where $1^* = \frac{N}{N-1}$.

Proposition 2.2 *By passing to a further subsequence, as $p \to 1$, we also have*

$$
\begin{aligned}
&(u_p; \partial_t u_p) \to_{L^2_w(\Omega_T)} (u_1; \partial_t u_1),\\
&u_p \to_{L^q(\Omega_T)} u_1 \qquad \textit{for all } \ 1 \le q < \frac{N}{N-1},\\
&u_p(\cdot,t) \to_{L^q(\Omega)} u_1(\cdot,t) \quad \textit{for all } \ 1 \le q < \frac{N}{N-1} \ \textit{ and for all } t \in (0,T],\\
&u_p(\cdot,0) \equiv u_o \to_{L^q(\Omega)} u_1(\cdot,0) \quad \textit{for all } \ 1 \le q < \frac{N}{N-1}.
\end{aligned}
$$

Moreover, $u_1 \in C^0([0,T]; L^2(\Omega))$, as the notion of variational solution requires.

Proof - The weak convergence of $(u_p; \partial_t u_p)$ follows from the boundedness estimates given by Lemma 2.2. Also the strong convergence in $L^q(\Omega_T)$ is a standard consequence of the boundedness estimates given by Lemma 2.2 and the observations concerning the Rellich Compactness Theorem given in Remark 2.4.

The time trace convergence follows from a standard trace inequality taken for $q < 1^*$, using that the $L^q(\Omega_T)$ space-time convergence is strong, and that $\left\|\partial_t u_p\right\|_{2,\Omega_T}$ is bounded.

From the previous convergence results, it follows that $\partial_t u_p \overset{L^q_w(\Omega_T)}{\to} \partial_t u_1$. This suffices to conclude that the limit of the $[t=0]$ traces converge to the $[t=0]$ trace of the limit: $u_p(\cdot,0) \overset{L^q(\Omega)}{\to} u_1(\cdot,0)$. Indeed, for any smooth cut-off function $\zeta = \zeta(t)$, which equals 1 at $t = 0$ and vanishes for $t = T$, the traces satisfy

$$
\begin{aligned}
\int_\Omega \left|u_1(\cdot,0) - u_p(\cdot,0)\right|^q dx &= \int_{\Omega_T} \frac{\partial}{\partial t}\left[-\left|u_1 - u_p\right|^q \zeta(t)\right] dxdt\\
&= \int_{\Omega_T} -q\left|u_1 - u_p\right|^{q-1} (\partial_t u_1 - \partial_t u_p)\,\zeta(t)\, dxdt - \int_{\Omega_T} \left|u_1 - u_p\right|^q \zeta'(t)\, dxdt\\
&\le q\left\|u_1 - u_p\right\|^{q-1}_{q,\Omega_T} \left\|\partial_t u_1 - \partial_t u_p\right\|_{q,\Omega_T} + \frac{1}{T}\left\|u_1 - u_p\right\|^q_{q,\Omega_T}.
\end{aligned}
$$

The above estimates are made rigorous by a regularized approximation in time. Because the sequence $\partial_t u_p$ converges weakly in $L^q(\Omega)$, the sequence $\left\|\partial_t u_1 - \partial_t u_p\right\|_{q,\Omega_T}$ is uniformly bounded by some absolute constant. It is now clear that the right-hand side can be made arbitrarily small by a sufficient choice of p. This shows that the traces must

strongly converge in $L^q(\Omega)$.

In particular, as the functions u_p have all the same initial time trace $u_o \in L^2(\Omega)$, we conclude that the limit must also have u_o as its initial time trace.

That $u_1 \in C^0([0,T];L^2(\Omega))$ follows from all the previous estimates, in a rather straightforward way using the square-integrable time derivatives. ■

Remark 2.5 From the above we have that, as long as for the original family $\left\{u_p\right\}_{p<p_o}$ it holds $u_p(\cdot,t) = \operatorname{tr} u_p(\cdot,t)$, then the same is true for the limit function u_1.

Corollary 2.3 *The compactness results of Proposition 2.1 and Proposition 2.2 hold verbatim when membership and limits are taken using the $W^{1,p}_{u_o}(\Omega)$ and $BV_{u_o}(\Omega)$ spaces, and $u_1 \in L^1_w(0,T;BV_{u_o}(\Omega))$.*

Proof - It is straightforward to check that the functions do not change along the sequence, and are independent of time over the set $\Omega^* \setminus \Omega$. Moreover, by the definition of the sequence $\{u_p\}$, Remark 2.3, and Proposition 2.2, all the assumptions of [25, Lemma 2.1] are satisfied, and therefore we can conclude that the limit function $u_1 \in L^1_w(0,T;BV_{u_o}(\Omega))$. ■

Since we have proved that

$$u_1 \in L^1_w(0,T;BV_{u_o}(\Omega)) \cap C^0([0,T];L^2(\Omega^*)),$$

we can now show that our compactness arguments suffice to pass from (1.8) to (1.12) along a subsequence of solutions $\left\{u_p\right\}$ to (1.2). The convergence in L^1 yields the lower semi-

continuity. Using formulation (1.6)

$$\begin{aligned}\int_0^T \|Du_1(\cdot,t)\|(\Omega^*)dt &\leq \liminf_{p\to 1}\frac{1}{p}\int_0^T\int_{\Omega^*}\left|Du_p\right|dxdt\\ &\leq \liminf_{p\to 1}\frac{|\Omega_T^*|^{1-\frac{1}{p}}}{p}\left[\int_{\Omega_T^*}|Du_p|^p\,dxdt\right]^{\frac{1}{p}}\\ &\leq \liminf_{p\to 1}\frac{|\Omega_T^*|^{1-\frac{1}{p}}}{p}\left\{\int_{\Omega_T^*}|Dv|^p\,dxdt\right.\\ &\left.+\int_{\Omega_T^*}\partial_t u_p\,(v-u_p)\,dxdt\right\}^{\frac{1}{p}},\end{aligned}$$

where the above holds for all $v\in L^{1+\varepsilon}\left(0,T;W^{1,1+\varepsilon}_{u_o}(\Omega)\right)\cap L^2(\Omega_T^*)$ and $\varepsilon>0$.

Now consider the restricted case where $v\in L^\infty\left(0,T;u_o+C^\infty_{o,\gamma,p_o}(\Omega)\right)\cap L^\infty\left(0,T;L^2(\Omega^*)\right)$ for any $\gamma>0$. Here u_o is directly regarded as defined on Ω^*.

$$\begin{aligned}\int_{\Omega_T^*}\partial_t u_p\,(v-u_p)\,dxdt &= \int_{\Omega_T^*}\partial_t u_p\,v\,dxdt-\frac{1}{2}\int_{\Omega_T^*}\partial_t\left[u_p^2\right]dxdt\\ &= \int_{\Omega_T^*}\partial_t u_p\,v\,dxdt+\frac{1}{2}\int_{\Omega^*}u_o^2\,dx-\frac{1}{2}\int_{\Omega^*}u_p^2(\cdot,T)\,dx.\end{aligned}$$

Take the limit inferior. In the first term, we have that $\partial_t u_p\to\partial_t u_1$ weakly in $L^2(\Omega_T^*)$. Observe that v is also in $L^2(\Omega_T^*)$. We get, using freely that the limit inferior of negative numbers is the negative of the limit superior of their magnitudes,

$$\begin{aligned}\liminf_{p\to 1}\int_{\Omega_T^*}\partial_t u_p\,(v-u_p)\,dxdt &\leq \int_{\Omega_T^*}\partial_t u_1\,v\,dxdt\\ &+\frac{1}{2}\int_{\Omega^*}u_o^2\,dx-\frac{1}{2}\limsup_{p\to 1}\int_{\Omega^*}u_p^2(\cdot,T)\,dx.\end{aligned}\tag{2.9}$$

From our *a priori* estimates, and particularly from the fact that

$$(u_p,\partial_t u_p)\to(u_1,\partial_t u_1)\qquad\text{weakly in }\ L^2(\Omega_T^*),$$

we have that $u_p(\cdot,T)\to u_1(\cdot,T)$ weakly in $L^2(\Omega^*)$. For all the details we refer to Lemma 4.2

of Section 4.

By the weak lower semicontinuity of the L^2 norm, we have

$$\int_{\Omega^*} u_1^2(\cdot,T)\,dx \le \liminf_{p\to 1}\int_{\Omega^*} u_p^2(\cdot,T)\,dx \le \limsup_{p\to 1}\int_{\Omega^*} u_p^2(\cdot,T)\,dx.$$

Substituting all this into (2.9), and a straightforward argument based on the Dominated Convergence Theorem showing that $\lim_{q\to p}\|f\|_q = \|f\|_p$ provided Ω^* is a finite-measure domain and $f \in L^{p+\delta}(\Omega^*)$, yields

$$\begin{aligned}\int_0^T \|Du_1(\cdot,t)\|(\Omega^*)\,dt \le &\int_{\Omega_T^*} |Dv|\,dxdt + \int_{\Omega_T^*} \partial_t u_1\, v\,dxdt + \frac{1}{2}\int_{\Omega^*} u_o^2\,dx\\ &-\frac{1}{2}\int_{\Omega^*} u_1^2(\cdot,T)\,dx\\ =&\int_{\Omega_T^*} |Dv|\,dxdt + \int_{\Omega_T^*} \partial_t u_1\,(v-u_1)\,dxdt\end{aligned}$$

for all $v \in L^\infty\left(0,T;u_o + C^\infty_{o,\gamma,p_o}(\Omega)\right) \cap L^\infty\left(0,T;L^2(\Omega^*)\right)$ with any $\gamma > 0$. The final point in the argument is now to show that taking the union over all $\gamma > 0$ of these spaces suitably approximates $L^1(0,T;BV_{u_o}(\Omega))$: this is exactly the content of Theorem 1.2.

As a consequence, the above test class recovers the full desired test class corresponding to the 1-Laplacian, and this concludes the proof.

3 Proof of Theorem 1.2

3.1 Elliptic Case: The Set $\left\{u_o + C^\infty_{o,\gamma,p}(\Omega)\right\}_{\gamma>0}$ is Dense in $BV_{u_o}(\Omega)$

Before getting to the actual details of the proof, let us first give a heuristic sketch of what we will be doing in the following.

Let $f \in L^1(0,T;BV_{u_o}(\Omega))$. By a parabolic extension of the original elliptic Giusti's approximation (see below what exactly we mean by that), we may approximate f within Ω

in the appropriate sense of $BV(\Omega)$ by a function

$$\varphi \in L^1\left(E_\eta; W^{1,1}(\Omega) \cap C^\infty(\Omega)\right),$$

where $\operatorname{tr}\varphi(\cdot,t) = \operatorname{tr} f(\cdot,t)$ at the interior side of the boundary, and $E_\eta \subset (0,T)$ is a proper set to be explained below. Still within Ω, now take

$$u_o + (\varphi - u_o)\,\zeta_n,$$

where ζ_n is a cut-off function properly decaying, and such as to separate the perturbation strictly away from the boundary. Extend this function to Ω^* through the u_o extension. This approximate now has both exterior and interior traces equal to u_o, as required by the p-Laplacian test classes. The necessary improvement in terms of integrability is not an easy task, but it is eventually obtained. We verify that

$$u_o + (\varphi - u_o)\,\zeta_n \overset{L^1(\Omega^*)}{\to} u_o + (\varphi - u_o)\,\chi_\Omega,$$

and that

$$\int_{\Omega^*} |D\left[u_o + (\varphi - u_o)\,\zeta_n\right]| \to \int_{\Omega^*\setminus\Omega} |Du_o| + \int_\Omega |D\varphi| + \int_{\partial\Omega} \left|u_o - \operatorname{tr}^- f\right| dH^{N-1}.$$

This would indeed suffice, because $D\varphi$ approximates the original quantities in the sense of the total variation on Ω. The other two remaining terms are the total variations of the original terms, when they are regarded as extended by u_o into $\Omega^* \setminus \Omega$. Thus, we capture all the term for the total variation in Ω^*.

So far for the sketch of the argument: we can now come to its technical implementation, which turns out to be quite delicate.

First, we work strictly within Ω and recall the construction Giusti uses to approximate a

given function $f \in BV(\Omega)$ with a sequence $\{f_\varepsilon\} \subset C^\infty(\Omega) \cap BV(\Omega)$ whose elements share the same interior trace as f (see [20, Theorem 1.17]). We will need this later on, and for that reason we include it here with all its details. For simplicity, we will refer to it in the sequel as *Giusti's approximation*, but it is actually due to Anzellotti and Giaquinta (see [49]).

Definition 3.1 (Giusti's approximation) *Let Ω be a bounded domain. Fix $\varepsilon > 0$ and let $m \in \mathbb{N}$ be so that*

$$\int_{\Omega \cap \left[\operatorname{dist}(\cdot,\partial\Omega) \leq \frac{1}{m}\right]} |Df| < \varepsilon.$$

Then let

$$A_1 = \Omega \cap \left[\frac{1}{m+2} < \operatorname{dist}(\cdot,\partial\Omega)\right]$$

and for $i = 2,3,\ldots$ define the sets

$$A_i = \Omega \cap \left[\frac{1}{m+(i+1)} < \operatorname{dist}(\cdot,\partial\Omega) < \frac{1}{m+(i-1)}\right].$$

Let $\mathscr{P} = \{\psi_{ij}\}$ be a partition of unity subordinate to the A_i and define $\psi_i = \sum_j \psi_{ij}$. As long as the domain is bounded, the set A_i will be compactly contained in Ω, and hence the sum that defines ψ_i consists of only finitely many terms. The approximation is defined as

$$f_\varepsilon = \sum_{i=1}^{\infty} J_{\varepsilon_i} * (f\psi_i),$$

where $J = J(x)$ is a standard, positive, symmetric mollifier, and the mollification parameter ε_i is chosen to satisfy

1. $\operatorname{supp} J_{\varepsilon_i} * (f\psi_i) \subseteq \Omega \cap \left[\frac{1}{m+(i+2)} < \operatorname{dist}(\cdot,\partial\Omega) < \frac{1}{m+(i-2)}\right]$,
2. $\int_\Omega |J_{\varepsilon_i} * (f\psi_i) - f\psi_i|\,dx < \varepsilon 2^{-i}$,
3. $\int_\Omega |J_{\varepsilon_i} * (fD\psi_i) - fD\psi_i|\,dx < \varepsilon 2^{-i}$.

Then one concludes that

$$\begin{aligned}
&\|f_\varepsilon - f\|_{1,\Omega} < \varepsilon,\\
&\int_\Omega |Df_\varepsilon|\, dx \le \|Df\|(\Omega) + 4\varepsilon,\\
&\lim_{\varepsilon\to 0}\int_\Omega |Df_\varepsilon|\, dx = \|Df\|(\Omega).
\end{aligned}$$

The next issue is to generalize this result to the time dependent setting. This is precisely the content of the following proposition, which can be seen as a uniform approximation in $W^{1,p_o}_{u_o}(\Omega)\cap L^2(\Omega)$.

Proposition 3.1 *Let Ω be a bounded, convex domain, with a compact boundary, which satisfies conditions* (**B1**)–(**B2**)*. Suppose that there exist $M>0$ and a function*

$$f \in L^1(0,T;BV(\Omega))$$

such that, uniformly over some measurable set $E\subseteq[0,T]$, we have

$$\|f(\cdot,t)\|_{BV(\Omega)} \le M \ \text{ whenever } \ t\in E.$$

Then for any $\eta>0$, we may find a measurable set $E_\eta\subseteq E$ such that $|E\setminus E_\eta|<\eta$, and the m-indexed functions

$$\left\{E\ni t\to\left[\|Df(\cdot,t)\|\left(\Omega\cap\left[d(\cdot,\partial\Omega)<\frac{1}{m}\right]\right)\right]\right\}_m$$

converge uniformly to 0 over E_η as $m\to\infty$. As a consequence, the Giusti approximation may be applied at once for a uniform choice of parameters ε_i, and for all $t\in E_\eta$ there exists

a sequence $\{f_\varepsilon(\cdot,t)\} \subset C^\infty(\Omega) \cap BV(\Omega)$ *with* $\varepsilon \to 0$ *such that*

$$\|f_\varepsilon(\cdot,t) - f(\cdot,t)\|_{1,\Omega} < \varepsilon \quad \textit{for all } t \in E_\eta, \tag{3.1}$$

$$\int_\Omega |Df_\varepsilon(\cdot,t)|\, dx \leq \|Df(\cdot,t)\|(\Omega) + 4\varepsilon \quad \textit{for all } t \in E_\eta, \tag{3.2}$$

$$\lim_{\varepsilon\to 0} \int_\Omega |Df_\varepsilon(\cdot,t)|\, dx = \|Df(\cdot,t)\|(\Omega) \quad \textit{for all } t \in E_\eta, \tag{3.3}$$

$$\mathrm{tr}_{\partial\Omega} f_\varepsilon(\cdot,t) = \mathrm{tr}_{\partial\Omega} f(\cdot,t) \quad \textit{for all } t \in E_\eta. \tag{3.4}$$

In turn, the integrability of Giusti's family can be further improved, selecting a second family of approximating functions $g_{1/j}(\cdot,t) \in W^{1,p_o}_{u_o}(\Omega) \cap L^2(\Omega)$*, indexed by* $t \in E_{2\eta} \subseteq E_\eta$*, which are as regular as is permitted by the given* $u_o \in W^{1,p_o}(\Omega) \cap L^2(\Omega)$*, and satisfy*

$$\left\|g_{1/j}(\cdot,t) - f(\cdot,t)\right\|_{1,\Omega} < \frac{2}{j} \quad \textit{for all } t \in E_{2\eta}, \tag{3.5}$$

$$\int_\Omega \left|Dg_{1/j}(\cdot,t)\right| dx \leq L < \infty \quad \textit{for all } t \in E_{2\eta}, \tag{3.6}$$

$$\begin{aligned} &\lim_{j\to\infty} \int_\Omega \left|Dg_{1/j}(\cdot,t)\right| dx \\ &\qquad = \|Df(\cdot,t)\|(\Omega) + \|u_o - f(\cdot,t)\|_{1,\partial\Omega} \quad \textit{for all } t \in E_{2\eta}, \end{aligned} \tag{3.7}$$

$$\mathrm{tr}_{\partial\Omega} g_{1/j}(\cdot,t) = \mathrm{tr}_{\partial\Omega} u_o \quad \textit{for all } t \in E_{2\eta}, \tag{3.8}$$

$$g_{1/j} \in \left\{L^\infty\left(E_{2\eta}; u_o + C^\infty_{0,\gamma,p_o}(\Omega)\right)\right\}_{\gamma>0} \cap L^\infty(E_{2\eta}; L^2(\Omega)), \tag{3.9}$$

for some $L > 0$*, which depends only on* M, u_o *and* Ω*.*

Remark 3.1 By [20, Theorem 2.11], the previous constructions are such as to ensure the convergence of the corresponding traces in the topology of $L^1(\partial\Omega)$.

Proof - Consider the family of functions

$$\left\{ E \ni t \to \left[\|Df(\cdot,t)\| \left(\Omega \cap \left[d(\cdot,\partial\Omega) < \frac{1}{m} \right] \right) \right] \right\}_m .$$

Since $f \in L^1(0,T;BV(\Omega))$, for each m fixed the corresponding function above is measurable in t. Moreover, the total variation is a measure and over E they are in fact finite measures as shown by the uniform BV estimates; therefore, we have from the Dominated Convergence Theorem that the sequence tends to 0 as $m \to \infty$, pointwise for each t.

However, E is itself a finite measure space. The above family of measurable functions now pointwise tends to 0. A direct application of the Egorov Theorem shows the existence of the desired E_η.

By showing that for all $t \in E_\eta$ a single choice of m can attain the desired fundamental condition of Giusti's approximation, namely that

$$\int_{\Omega \cap \left[\mathrm{dist}(\cdot,\partial\Omega) \leq \frac{1}{m} \right]} |Df(\cdot,t)| < \varepsilon,$$

we may now fix a common geometric decomposition A_i for all times $t \in E_\eta$. The partition-of-unity functions ψ_i are now fixed and common for all these time levels.

As the function ψ_i are fixed for the time levels $t \in E_\eta$, and the functions $f(\cdot,t)$ satisfy a uniform BV estimate here, we argue that Conditions 1.–3. of Construction 3.1 may be achieved by a uniform choice of ε_i.

Condition 1. altogether depends only on the supports of the functions ψ_i, which again are the same for all these time levels.

As for Conditions 2.–3., in Lemma 4.1 of Section 4 we show that uniform BV estimates imply uniform translation continuity. Assuming this fact, $f(\cdot,t)\,\psi_i$ and $f(\cdot,t)\,D\psi_i$ will be uniformly translation continuous for all t, being the product of two such terms. This ensures that the approximation by mollification may be done uniformly.

By satisfying Conditions 1.–3., we now have from Giusti's approximation that (3.1)–

(3.4) are satisfied for a family contained in $C^\infty(\Omega)\cap BV(\Omega)$.

It remains to improve the integrability of such a family beyond $BV(\Omega)$. We now work with the particular sequence $\{f_{1/j}\}_{j\in\mathbb{N}}$.

Keeping in mind that obviously

$$f_{1/j}(\cdot,t) = u_o + \left[f_{1/j}(\cdot,t) - u_o\right],$$

let

$$g_{1/j,n}(\cdot,t) = u_o + \left[f_{1/j}(\cdot,t) - u_o\right]\zeta_n(x), \tag{3.10}$$

where ζ_n is a proper cut-off function, which we are going to build next.

First consider a local coordinate setting in which the boundary is flat at $[x_N = 0]$ and $\Omega \subseteq \{x_N \geq 0\}$. Define the piecewise linear functions $\chi_n \in W^{1,\infty}\left(\mathbb{R}^N\right)$ by

$$\chi_n(x) = \begin{cases} 0 & | \; x_N \in [0, 1/n] \\ n\left(x_N - \frac{1}{n}\right) & | \; x_N \in (1/n, 2/n] \\ 1 & | \; x_N \in (2/n, \infty) \end{cases}$$

These now given, let $\{U_i\}_{i=1}^k$ be an open covering of $\partial\Omega$ equipped with C^1, local chart maps $L_i : \bar{\Omega}\cap U_i \to [x_N \geq 0]$ with local inverse of the form

$$L_i^{-1}(\bar{x}, x_N) = \Phi_i(\bar{x}) + x_N\vec{\nu}_{\bar{x}}, \tag{3.11}$$

where $\bar{x} = (x_1, \ldots, x_{N-1})$, $\Phi_i(\bar{x})$ locally charts the boundary of Ω, and $\vec{\nu}_{\bar{x}}$ is the surface interior normal at $\Phi_i(\bar{x})$. The existence of such maps is guaranteed by the compactness and C^1 nature of Ω, together with an application of the inverse function theorem.

Up to inclusion of at most one more open set U_o, we may consider this a finite open cover of $\bar{\Omega}$. Notice that

- for the index i of the finite open cover, we have $0 \leq i \leq k$;
- for the index n of the piecewise linear functions χ_n, we have $n \geq 1$.

Now let $\{\Psi_i\}_{i=0}^k$ be initially constructed as a partition of unity subordinate to $\{U_i\}_{i=0}^k$, and then where all partition functions which are nonzero on $\bar{\Omega}$, whose supports have been designated as belonging to a fixed open set U_i, have been summed. Since $\bar{\Omega}$ is compact and is covered by the open sets U_i, all but finitely many partition functions vanish on it. Thus, these sums are classical and themselves sum to unity, while each of them is also compactly supported in its own respective U_i.

The function $\zeta_n : \mathbb{R}^N \to [0,1]$ may now be defined as

$$\zeta_n(x) = \Psi_o(x) + \sum_{i=1}^{k} \Psi_i(x) \left[\chi_n \circ L_i\right](x).$$

We can now go back to the functions $g_{1/j,n}$ defined in (3.10). Since $f_{1/j}(\cdot,t) \in C^\infty(\Omega)$, and $\zeta_n \in W^{1,\infty}(\Omega)$ is supported at a fixed distance from $\partial\Omega$, we conclude that $g_{1/j,n}(\cdot,t)$ belongs to the same Sobolev class as u_o. Moreover, $g_{1/j,n}(\cdot,t)$ is identically u_o in some small neighborhood of $\partial\Omega$. Altogether, we conclude that $g_{1/j,n}(\cdot,t) \in W_{u_o}^{1,p_o}(\Omega)$.

The argument is concluded, once we show (3.5)–(3.9). For (3.5), we have

$$\begin{aligned}
\left\| f_{1/j}(\cdot,t) - g_{1/j,n}(\cdot,t) \right\|_{1,\Omega} &\leq \int_\Omega \left| f_{1/j}(\cdot,t) - u_o \right| (1-\zeta_n)\, dx \\
&\leq \int_\Omega \left| f_{1/j}(\cdot,t) - f \right| (1-\zeta_n)\, dx \\
&\quad + \int_\Omega \left| f(\cdot,t) - u_o \right| (1-\zeta_n)\, dx.
\end{aligned}$$

The right-hand side can be made arbitrarily close to $1/j$, independently of t, by majorizing the first term with the L^1 norm. The second term may be controlled as like the prior use of Egorov's theorem by taking the support of $(1-\zeta_n)$ sufficiently near the boundary. Recall that $\lim \int \left| f_{1/j} - f \right| dx < 1/j$ is the lower limit to approximation power which is why the Proposition was given with a $2/j$ estimate.. Altogether this shows that $n = n(j)$ may be

picked to uniformly approximate the $f_{1/j}$ across all $t \in E_\eta$.

For (3.6), by direct computation we have

$$\int_\Omega \left|D\left[g_{1/j,n}(\cdot,t)\right]\right| dx = \int_\Omega \Big|Du_o + D\left[f_{1/j}(\cdot,t) - u_o\right]\zeta_n + \left[f_{1/j}(\cdot,t) - u_o\right] D\zeta_n\Big| dx.$$

It follows from (3.2) and *a priori* estimates of u_o, that the first two terms are bounded uniformly for all t by a quantity that depends only on M and u_o. The third term is similarly handled, namely

$$\begin{aligned}
&\left|\int_\Omega \left[f_{1/j}(\cdot,t) - u_o\right] D\zeta_n\, dx\right| \\
&= \left|-\int_\Omega D\left[f_{1/j}(\cdot,t) - u_o\right]\zeta_n dx + \int_{\partial\Omega}\left[f_{1/j}(\cdot,t) - u_o\right]\zeta_n \vec{n} dH^{N-1}\right| \\
&\leq \int_\Omega \left|D\left[f_{1/j}(\cdot,t) - u_o\right]\right| dx + N\int_{\partial\Omega}\left|f_{1/j}(\cdot,t) - u_o\right| dH^{N-1}.
\end{aligned}$$

The first term above is controlled just as before. The second term, the trace on the boundary, is bounded by its BV norm, up to a constant depending only on Ω (see [47, page 180]). This establishes (3.6).

As for (3.7), we have

$$\begin{aligned}
\int_\Omega \left|D\left[g_{1/j,n}(\cdot,t)\right]\right| dx = &\int_{\Omega\cap[\operatorname{supp} D\zeta_n]^c} \left|Du_o + D\left[f_{1/j}(\cdot,t) - u_o\right]\zeta_n\right| dx \\
&+ \int_{\Omega\cap[\operatorname{supp} D\zeta_n]} \Big|Du_o + D\left[f_{1/j}(\cdot,t) - u_o\right]\zeta_n \\
&+ \left[f_{1/j}(\cdot,t) - u_o\right] D\zeta_n\Big| dx
\end{aligned} \tag{3.12}$$

We apply Egorov's Theorem a second time to the family of functions

$$\left\{E_\eta \ni t \to \int_{\Omega\cap\left[d(\cdot;\partial\Omega)<\frac{1}{m}\right]} \left(|Du_o| + \left|D\left[f_{1/j}(\cdot,t) - u_o\right]\right|\right) dx\right\}_m.$$

By absolute continuity, they tend to zero pointwise. From Egorov's Theorem, it now holds that the limit in m is uniform for all t, up to the exclusion of an arbitrary small set. Next, n may be picked so that

$$\Omega \cap [\mathrm{supp} D\zeta_n] \subseteq \Omega \cap \left[d(\cdot; \partial\Omega) < \frac{1}{m} \right].$$

These remarks show that the second term on the right-hand side of (3.12) reduces to

$$\int_{\Omega \cap [\mathrm{supp} D\zeta_n]} \left| \left[f_{1/j}(\cdot,t) - u_o \right] D\zeta_n \right| dx,$$

up to negligible terms, by choosing $n > n(j)$ for all $t \in E_{\frac{3}{2}\eta}$. (Note initially the Egorov sets would also depend on j, but by having the measure of their complements diminish geometrically in j, the intersection of those sets can have a complement with measure no greater than $\frac{3}{2}\eta$ in $[0,T]$. Thus while achieving the desired estimate requires $n = n(j)$, the time levels over which the estimate holds may be taken as independent of j.)

Recall that Ψ_o is fixed by the geometry of Ω. Accordingly, n may be picked so large, that its contribution to $D\zeta_n$ vanishes.

The final term is thus

$$\int_\Omega \left| \sum_{i=1}^{k} \left[f_{1/j}(\cdot,t) - u_o \right] \left(D\Psi_i(x) \left[\chi_n \circ L_i \right](x) + \Psi(x) D \left[\chi_n \circ L_i \right](x) \right) \right| dx \tag{3.13}$$

In the region where $\Psi_o \equiv 0$, it holds that $\sum_{i=1}^{k} D\Psi_i(x) \equiv 0$ by the partition of unity properties. Thus, the first quantity identically vanishes in $\cap_i [\chi_n \circ L_i = 1]$. The complement of this region by suitable choice of $n(j)$ can be made sufficiently close to the boundary for a modestly expanded use of Egorov to make this first integral quantity arbitrarily small over the common $E_{\frac{3}{2}\eta}$ set as well. We have used that the $D\Psi_i$ are fixed by Ω and are a priori bounded accordingly. Hence, the first quantity in (3.13) is negligible by a choice $n = n(j)$. The second quantity is handled by exploiting the structure inherent in (3.11).

We claim that

$$D\left[\chi_n \circ L_i\right] \circ L_j^{-1}(\bar{x}; x_N) = n\chi_{[1/n \leq x_N \leq 2/n]} \vec{\nu}_{\bar{x}}^{\,\mathrm{tr}}. \tag{3.14}$$

where $\vec{\nu}_{\bar{x}}$ is the surface normal at $\Phi_j(\bar{x})$. In order to show that (3.14) indeed holds true, first compute from the chain rule

$$\begin{aligned} D\left[\chi_n \circ L_i\right] \circ L_j^{-1} &= \left(D\left[\chi_n \circ L_i\right] \circ L_i^{-1}\right) \circ \left(L_i \circ L_j^{-1}\right) = \left(D\left[\chi_n\right]\left(D\left[L_i\right] \circ L_i^{-1}\right)\right) \circ \left(L_i \circ L_j^{-1}\right) \\ &= \left[\begin{pmatrix} 0 & \dots & 0 & n\chi_{[1/n \leq x_N \leq 2/n]} \end{pmatrix} \left(DL_i^{-1}\right)^{-1}\right] \circ \left(L_i \circ L_j^{-1}\right) \end{aligned}$$

The chain rule can surely be applied, since the functions χ_n are piecewise linear, and the maps L_i and their inverses are of class C^1. Exploiting the orthogonality between $\vec{\nu}_{\bar{x}}$ and the vectors of $D_{\bar{x}}\Phi$ as well as $D_{\bar{x}}\vec{\nu}_{\bar{x}}$, we have

$$D\left[L_i^{-1}\right] = \begin{pmatrix} D_{\bar{x}}\Phi_{\bar{x}} + x_N D_{\bar{x}}\vec{\nu}_{\bar{x}} & \vec{\nu}_{\bar{x}} \end{pmatrix} \text{ and } \left[DL_i^{-1}\right]^{-1} = \begin{pmatrix} \mathscr{F}_\Phi^{-1}(\bar{x}) & 0 \\ 0 & 1 \end{pmatrix} \left[DL_i^{-1}\right]^{\mathrm{tr}}$$

where we let $\mathscr{F}_\Phi(\bar{x}) = [D\Phi]^{\mathrm{tr}}[D\Phi]$.

Notice that there is a slight abuse of notation here, as, strictly speaking, $\mathscr{F}_\Phi$ is *not* the first fundamental form, but only a term that tends to it, as $x_N \to 0$. However, this is not crucial for the argument.

Combining the last result with the previous chain rule computation, yields

$$\begin{aligned} D\left[\chi_n \circ L_i\right] \circ L_i^{-1} &= \begin{pmatrix} 0 & \dots & 0 & n\chi_{[1/n \le x_N \le 2/n]} \end{pmatrix} \begin{pmatrix} \mathscr{F}_\Phi^{-1}(\bar{x}) & 0 \\ 0 & 1 \end{pmatrix} \left[DL_i^{-1}\right]^{\mathrm{tr}} \\ &= \begin{pmatrix} 0 & \dots & 0 & n\chi_{[1/n \le x_N \le 2/n]} \end{pmatrix} \left[DL_i^{-1}\right]^{\mathrm{tr}} \\ &= \begin{pmatrix} 0 & \dots & 0 & n\chi_{[1/n \le x_N \le 2/n]} \end{pmatrix} \begin{pmatrix} 0 \\ \vdots \\ 0 \\ \vec{\nu}_{\bar{x}}^{\mathrm{tr}} \end{pmatrix}, \end{aligned}$$

and simplifying the product we obtain

$$D\left[\chi_n \circ L_i\right] \circ L_j^{-1} = \left(n\chi_{[1/n \le x_N \le 2/n]} \vec{\nu}_{\bar{x}}^{\mathrm{tr}}\right) \circ \left(L_i \circ L_j^{-1}\right)$$

One checks from their explicit construction that $L_i \circ L_j^{-1} = \left(\Phi_i^{-1} \circ \Phi_j(\bar{x}); x_N\right)$; $\vec{\nu}_{\bar{x}}$ is the surface normal at $\Phi_i(\bar{x})$. Consequently $\vec{\nu}_{\bar{x}} \circ \left(L_i \circ L_j^{-1}\right)$ is the surface normal at $\Phi_i \circ \Phi_i^{-1} \circ \Phi_j(\bar{x}) = \Phi_j(\bar{x})$. This verifies (3.14).

We may also verify from the expression above that

$$\begin{aligned} \lim_{x_N \to 0} \left|\det D\left[L_i^{-1}\right]\right| &= \lim_{x_N \to 0} \sqrt{\left|\det\left(D\left[L_i^{-1}\right]^{\mathrm{tr}} D\left[L_i^{-1}\right]\right)\right|} \\ &= \sqrt{\left|\det\left(\mathscr{F}_\Phi\right)\right|}. \end{aligned} \tag{3.15}$$

The right hand-side is well known to be the surface area Jacobian under the parameterization Φ.

Altogether, we have

$$\begin{aligned}
&\int_\Omega \left| \sum_{i=1}^{k} \left(f_{1/j} - u_o\right) \Psi_i D\left[\chi_n \circ L_i\right] \right| dx \\
&\quad = \sum_{r=1}^{k} \int_{\text{Chart}_r} \left| \sum_{i=1}^{k} \left(\left(f_{1/j} - u_o\right) \circ L_r^{-1} \right) \left(\Psi_i \circ L_r^{-1}\right) \left(D\left[\chi_n \circ L_i\right] \circ L_r^{-1}\right) \right| \left(\Psi_r \circ L_r^{-1}\right) J_{L_r^{-1}} dx \\
&\quad = \sum_{r=1}^{k} \int_{\text{Chart}_r} \left| \sum_{i=1}^{k} \left(\left(f_{1/j} - u_o\right) \circ L_r^{-1} \right) \left(\Psi_i \circ L_r^{-1} \right) n\chi_{[1/n \le x_N \le 2/n]} \vec{\nu}_{\bar{x}} \right| \left(\Psi_r \circ L_r^{-1}\right) J_{L_r^{-1}} dx.
\end{aligned}$$

Since $\vec{\nu}_{\bar{x}}$ is in all terms the surface normal at $\Phi_r(\bar{x})$, the only terms participating in the sum over i are the partition of unity terms indexed by i which must then sum to 1. Letting $n \to \infty$, the term with $n\chi$ averages all terms to their $[x_N = 0]$ values. In particular, $J_{L_r^{-1}}$ becomes precisely the surface area Jacobian. We conclude

$$\lim_{n\to\infty} \int_\Omega \left| \sum_{i=1}^{k} \left(f_{1/j} - u_o\right) \Psi_i D\left[\chi_n \circ L_i\right] \right| dx = \sum_{r=1}^{k} \int_{\partial\Omega} \left| f - u_o \right| \Psi_r \, dH^{N-1} = \int_{\partial\Omega} \left| f - u_o \right| dH^{N-1}.$$

We have used that

$$\operatorname{tr} f_{1/j} = \operatorname{tr} f,$$

due to Giusti's approximation. The terms of (3.12) now become

$$\begin{aligned}
&\lim_{n\to\infty} \int_\Omega \left| D\left[g_{1/j,n}(\cdot,t)\right] \right| dx \\
&\qquad = \int_\Omega \left| D\left[f_{1/j}(\cdot,t)\right] \right| dx + \int_{\partial\Omega} \left| f - u_o \right| dH^{N-1}.
\end{aligned} \tag{3.16}$$

Recall that the total variations of $f_{1/j}$ do approximate the total variation of the f. Further, because the family $g_{1/j,n}(\cdot;t)$ was constructed from the original family $f(\cdot;t)$ by applying a *common*, measurable construction across all time levels uniformly, all the members of the family and their norms inherit measurablility in t. From (3.16) and Egorov's theorem, it holds that for j fixed, the limit in n is uniform up to the exclusion of a subset of $(0,T)$ of arbitrarily small measure. Though initially each j leads to its own subset, by again

diminishing the measures of the complements of the jth Egorov set geometrically, we may take a common set. This may be taken as saying the limit is uniform in $n(j)$ over a set $E_{\frac{5}{3}\eta} \subseteq (0,T)$ where the latter set is independent of j.

Now, after suitably choosing $n(j)$ in order to sufficiently approximate (3.16) independent of t, define the function

$$g_{1/j}(\cdot,t) = u_o + J_\alpha * \left[\left(f_{1/j}(\cdot,t) - u_o \right) \zeta_{n(j)}(x) \right].$$

At each t an α may be picked so that $J_\alpha * (\cdot)$ sufficiently approximates the $W^{1,1}$ norm of its argument because that argument is compactly supported in the interior of Ω. Clearly too, that mollified function does not perturb the u_o trace. These are achieved, because ζ_n vanishes at some fixed distance away from the boundary. Since the $W^{1,1}$ norm of $g_{1/j,n}(\cdot;t)$ was shown to satisfy (3.16), the α limit can be chosen to maintain that approximation. Thus, the mollification can attain that limit as well when $j \to \infty$ for a suitable choice of $\alpha(j,n(j),t)$.

The parameter $\alpha = \alpha(j,n(j))$ may be chosen independent of t and still respect the limit by a final appeal to Egorov over a suitable set $t \in E_{2\eta}$ by considering the functions (with $n(j)$ and j fixed)

$$\left\{ E_{\frac{5}{3}\eta} \ni t \to \left\| J_\alpha * \left[\left(f_{1/j}(\cdot,t) - u_o \right) \zeta_n \right] - \left(f_{1/j}(\cdot,t) - u_o \right) \zeta_n \right\|_{W^{1,1}(\Omega)} \right\}_{\alpha = \frac{1}{m}}.$$

By the same geometric series device as before, the Egorov set $E_{2\eta} \subseteq [0,T]$ of times for which the limit is uniform may be taken independent of j while the rate of convergence will depend on j. Further $g_{1/j}(\cdot;t) \in u_o + C_0^\infty(\Omega)$, and its support from the boundary may be quantified solely by $n(j)$ through $\zeta_{n(j)}(x)$ with correspondingly small α.

With $\alpha(j,n(j))$ and $n(j)$ fixed, $g_{1/j}(\cdot,t)$ is as regular as is permitted by u_o, and from the uniform L^1 estimates of $f_{1/j}$ and its derivatives, sup bounds for the mollifications and their derivatives may be obtained. Indeed the kernel $\|J_\varepsilon\|_\infty = O(\varepsilon^{-N})$, so each $g_{1/j}(\cdot,t) - u_o$

and its derivatives are uniformly L^∞–bounded, independent of t. Accordingly, $g_{1/j} \in L^\infty(E_{2\eta}; L^2(\Omega))$. Finally, due to the uniform BV estimates given in (3.6) and the α and n fixed, the perturbative term similarly belongs to $L^\infty\left(E_{2\eta}; u_o + C^\infty_{0,\gamma(j),p_0}(\Omega)\right)$ and accordingly $g_{1/j} \in \left\{L^\infty(E_{2\eta}; u_o + C^\infty_{0,\gamma,p_o}(\Omega))\right\}_{\gamma>0}$. ■

Remark 3.2 The proof actually shows the stronger estimate

$$\left\|g_{1/j}(\cdot;t) - u_o\right\|_{W^{1,\infty}(\Omega)} \leq \Lambda(j) < \infty \qquad \forall t \in E_{2\eta}$$

Remark 3.3 Estimates (3.5)–(3.8) imply that when all concerned functions are regarded as extended by u_o from Ω into Ω^* as defined in (1.7), the $g_{1/j}(\cdot,t)$ approximate the $f(\cdot,t)$ in the $BV(\Omega^*)$ norm.

3.2 Parabolic Case: $\left\{L^\infty(0,T;u_o + C^\infty_{0,\gamma,p_o}(\Omega))\right\}_{\gamma>0} \cap L^\infty\left(0,T;L^2(\Omega)\right)$ is Dense in $L^1\left(0,T;BV_{u_o}(\Omega)\right)$

Proposition 3.2 *The set* $\left\{L^\infty(0,T;u_o + C^\infty_{0,\gamma,p_o}(\Omega))\right\}_{\gamma>0} \cap L^\infty\left(0,T;L^2(\Omega)\right)$ *is dense in the space* $L^1\left(0,T;BV_{u_o}(\Omega)\right)$.

Proof - Let $v \in L^1(0,T;BV_{u_o}(\Omega))$ be fixed. Then, in particular, as discussed in (1.9),

$$\|Dv(\cdot,t)\|(\Omega^*) = \|Du_o\|\left(\Omega^* \setminus \bar{\Omega}\right) + \left\|\mathrm{tr}^- v(\cdot,t) - u_o\right\|_{L^1(\partial\Omega)} + \|Dv(\cdot,t)\|(\Omega),$$

and

$$\varphi(t) := \|v(\cdot,t)\|_{BV(\Omega^*)} \in L^1(0,T).$$

Next, we decompose this function. Write

$$\varphi(t) = \varphi(t)\chi_{[\varphi \leq M]} + \varphi(t)\chi_{[\varphi > M]} := \varphi_{1,M}(t) + \varphi_{2,M}(t).$$

Observe that both $\varphi_{1,M}, \varphi_{2,M} \leq \varphi$, which is an integrable function. In particular, integrability implies that for almost every $t \in (0,T)$, $\varphi(t)$ is finite and $\lim_{M\to\infty} \chi_{[\varphi(t)\geq M]} = 0$ for

almost every t, and so the Dominated Convergence Theorem applies.

We claim that it is sufficient to approximate v in the norm of the space $L^1\left(0,T;BV_{u_o}(\Omega)\right)$ over the set $[\varphi \leq M]$ by an element

$$\phi \in \left\{L^\infty(0,T;u_o + C^\infty_{0,\gamma,p_o}(\Omega))\right\}_{\gamma>0} \cap L^\infty\left(0,T;L^2(\Omega)\right),$$

which is identically u_o in $[\varphi > M]$. Note that at each time level such a function is regarded as extended to be u_o throughout all of Ω^*, as defined in (1.7). Let us first consider the contribution coming from the L^1-norm. For such a ϕ,

$$\begin{aligned}\int_0^T \|v-\phi\|_{1,\Omega^*}(t)\,dt \leq & \int_0^T \|v-u_o\|_{1,\Omega^*}(t)\,\chi_{[\varphi>M]}dt \\ & + \int_0^T \|v-\phi\|_{1,\Omega^*}(t)\,\chi_{[\varphi\leq M]}dt \\ \leq & \int_0^T \varphi(t)\chi_{[\varphi>M]}dt + \|u_o\|_1 \int_0^T \chi_{[\varphi>M]}dt \\ & + \int_{[\varphi\leq M]} \|v-\phi\|_{1,\Omega}(\cdot,t)\,dt.\end{aligned}$$

By suitably *a priori* picking M and using DCT, we can make the first two terms arbitrarily small. Thus, if $v\chi_{[\varphi\leq M]}$ can be approximated by such ϕ, the last term is small too, and netwise we may use them to approximate v in $L^1\left(0,T;L^1(\Omega^*)\right)$.

Similarly, for the total variation part over Ω^* we have

$$\begin{aligned}&\left|\int_0^T |v|_{BV}\,dt - \int_0^T |\phi|_{BV}\,dt\right| \\ &\qquad \leq \int_0^T \varphi_{2,M}dt + |u_o|_{BV}\int_0^T \chi_{[\varphi>M]}dt \\ &\qquad\quad + \left|\int_0^T |v|_{BV}\,\chi_{[\varphi\leq M]}dt - \int_0^T |\phi|_{BV}\,\chi_{[\varphi\leq M]}dt\right|.\end{aligned}$$

Once more, from the integrability of φ, we may choose M, so that the first terms are arbitrarily small. We are still assuming that ϕ may be picked to approximate our desired $v\chi_{[\varphi\leq M]}$ term. Thus, it is sufficient to approximate the latter term.

On the $\chi_{[\varphi\leq M]}$ time levels, the $|v(\cdot,t)|_{BV(\Omega^*)}$ norm is uniformly bounded by M. We may apply Proposition 3.1 and for $\eta>0$ fixed, we conclude that there exist a set $E_{2\eta}\subseteq[\varphi\leq M]$ such that $|\,[\varphi\leq M]\setminus E_{2\eta}|<2\eta$, and a corresponding family of functions $v_{1/j}(\cdot,t)$ as given in the proposition. For $t\in[\varphi\leq M]\setminus E_{2\eta}$, set $v_{1/j}(\cdot;t)=u_0$ like before.

At each time level these $W^{1,p}_{u_o}(\Omega)\cap L^2(\Omega)$ traces are now regarded as also extended to Ω^* through the u_o extension, as defined in (1.7). In particular,

$$\left\|Dv_{1/j}(\cdot,t)\right\|(\Omega^*)=\|Du_o\|\left(\Omega^*\setminus\bar{\Omega}\right)+\left\|Dv_{1/j}(\cdot,t)\right\|(\Omega)$$

We relied on the approximation (3.6)–(3.7), on the Dominated Convergence Theorem, and that $v_{1/j}$ may not charge the boundary due to its Sobolev regularity. Altogether, these facts yield that

$$\begin{aligned}
\lim_{j\to\infty}\int_{[\varphi\leq M]}\left\|Dv_{1/j}(\cdot,t)\right\|(\Omega^*)\,dt &= \lim_{j\to\infty}\left(\int_{E_{2\eta}}\left\|Dv_{1/j}(\cdot,t)\right\|(\Omega^*)\,dt+\int_{[\varphi\leq M]\setminus E_{2\eta}}\left\|Dv_{1/j}(\cdot,t)\right\|(\Omega^*)\,dt\right)\\
&=\int_{[\varphi\leq M]}\|Du_o\|\left(\Omega^*\setminus\bar{\Omega}\right)dt+\lim_{j\to\infty}\left(\int_{E_{2\eta}}\left\|Dv_{1/j}(\cdot,t)\right\|(\Omega)\,dt+\int_{[\varphi\leq M]\setminus E_{2\eta}}\left\|Dv_{1/j}(\cdot,t)\right\|(\Omega)\,dt\right)\\
&=\int_{[\varphi\leq M]}\|Du_o\|\left(\Omega^*\setminus\bar{\Omega}\right)dt+\int_{E_{2\eta}}\|\mathrm{tr}\,v(\cdot,t)-u_o\|_{1,\partial\Omega}\,dt+\int_{E_{2\eta}}\|Dv(\cdot,t)\|(\Omega)dt\\
&\quad+\lim_{j\to\infty}R_j
\end{aligned}$$

The R_j are bounded in magnitude by $|u_0|_{BV}*2\eta$. We may further ensure that $\chi_{E_{2\eta}}\to\chi_{[\varphi\leq M]}$ a.e. by choosing a subsequence $2\eta_i=2^{-i}$. Indeed, by the Borell-Cantelli lemma we would have that the measure of points belonging to infinitely many of the sets $[\varphi\leq M]\setminus E_{2\eta_i}$ is 0. Now appealing to dominated convergence over the sequence η_i – recall [47, page

180] guarantees the trace term is bounded by the BV norm – we obtain

$$\begin{aligned}
&\lim_{j\to\infty}\int_{[\varphi\le M]}\left\|Dv_{1/j}(\cdot,t)\right\|(\Omega^*)\,dt\\
&\quad=\int_{[\varphi\le M]}\|Du_0\|\left(\Omega^*\setminus\bar{\Omega}\right)dt\quad+\int_{[\varphi\le M]}\|\mathrm{tr}\,v(\cdot,t)-u_o\|_{1,\partial\Omega}\,dt+\int_{[\varphi\le M]}\|Dv\|(\Omega)\,dt\\
&\quad=\int_{[\varphi\le M]}\|Dv(\cdot,t)\|(\Omega^*)\,dt.
\end{aligned}$$

■

4 Some Technical Results

Lemma 4.1 *Assume that $\Omega\subset\mathbb{R}^N$ is an open, convex domain. Then uniform BV estimates imply uniform translation continuity.*

Proof - We recall an elementary step of the Rellich compactness argument for an arbitrary function $\varphi\in C^\infty(\Omega)\cap BV(\Omega)$. If, for a fixed $h\in\mathbb{R}^N$ we let $\Omega-h\overset{\text{def}}{=}\{x-h:\ x\in\Omega\}$, we have

$$\begin{aligned}
\int_\Omega|T_h\varphi-\varphi|\,dx&=\int_\Omega|\varphi(\cdot+h)\,\chi_{\Omega-h}-\varphi(\cdot)|\,dx\\
&=\int_{\Omega\cap\Omega-h}|\varphi(\cdot+h)-\varphi(\cdot)|\,dx+\int_{\Omega\setminus\Omega-h}|\varphi(\cdot)|\,dx.
\end{aligned}\tag{4.1}$$

In the first term on the right-hand side of (4.1), appealing to the convexity of Ω to justify the line integral, we may estimate

$$\begin{aligned}
\int_{\Omega\cap\Omega-h}|\varphi(\cdot+h)-\varphi(\cdot)|\,dx&\le\int_{\Omega\cap\Omega-h}\left|\int_0^{|h|}\frac{d}{dt}\left[\varphi\left(x+\frac{t}{|h|}h\right)\right]dt\right|dx\\
&\le\int_{\Omega\cap\Omega-h}\int_0^{|h|}\left|D\varphi\left(x+\frac{t}{|h|}h\right)\cdot\frac{h}{|h|}\right|dtdx\\
&\le\int_0^{|h|}\int_{\Omega\cap\Omega-h}\left|D\varphi\left(x+\frac{t}{|h|}h\right)\right|dxdt\\
&\le|h|\,\|D\varphi\|_{1,\Omega}.
\end{aligned}$$

In the last inequality, the convexity of Ω allows us to conclude that, even with the shift, we are still integrating in Ω. As for the second term of (4.1), we used the Hölder inequality and a Sobolev embedding:

$$\int_{\Omega\setminus\Omega-h} |\varphi|\,dx \leq \|\varphi\|_{\frac{N}{N-1}} |\Omega\setminus\Omega-h|^{\frac{1}{N}} \leq \gamma(\Omega)\,\|\varphi\|_{BV(\Omega)}\,|\Omega\setminus\Omega-h|^{\frac{1}{N}}.$$

Therefore, if an estimate for $\|\varphi\|_{BV(\Omega)}$ is given, then for any $\varepsilon>0$ fixed, we may find a suitable $\delta>0$, such that for $|h|<\delta$, we have

$$\int_{\Omega} |T_h\varphi-\varphi|\,dx<\varepsilon. \qquad \blacksquare$$

Lemma 4.2 *Let $p\to 1$. When Proposition 2.2 holds, if $(u_p;\partial_t u_p)\to(u_1,\partial_t u_1)$ weakly in $L^2(\Omega_T)$, then $u_p(\cdot,t)\to u_1(\cdot,t)$ weakly in $L^2(\Omega)$ for all t. As a consequence*

$$\|u_1(\cdot,t)\|_{2,\Omega} \leq \liminf_{p\to 1} \left\|u_p(\cdot,t)\right\|_{2,\Omega}.$$

Proof - By a standard approximation argument, for all $\varphi\in L^2(\Omega)$ we have

$$\int_{\Omega} u_p(x,t)\,\varphi(x)\,dx = \int_{\Omega} u_o(x)\varphi(x)\,dx + \int_{\Omega\times(0,t)} \partial_\tau u_p(x,\tau)\,\varphi(x)\,dxd\tau.$$

By weak convergence on the right side, we see that the functional

$$L^2(\Omega)\ni\varphi(x)\to\lim_{p\to 1}\int_{\Omega} u_p(x,t)\,\varphi(x)\,dx$$

is well-defined and by the Hölder inequality is also continuous. By the Riesz representation theorem, $\exists\, w(\cdot,t)\in L^2(\Omega)$, such that

$$\int_{\Omega} w(x,t)\,\varphi(x)\,dx = \lim_{p\to 1}\int_{\Omega} u_p(x,t)\,\varphi(x)\,dx.$$

By Proposition 2.2, we have that the traces converge strongly to $u_1(\cdot,t)$ in $L^q(\Omega)$ for $q < 1^*$. Thus, $\forall \varphi \in C_o^\infty(\Omega)$

$$\int_\Omega [w(x,t) - u_1(x,t)]\, \varphi(x)\, dx = 0.$$

As both functions belong to $L^q(\Omega)$, this suffices to conclude that the functions agree almost everywhere. Finally, weak lower semicontinuity of the trace L^2 norm follows by an elementary argument: for $\|\varphi\|_{2,\Omega} = 1$,

$$\int_\Omega u_1(\cdot,t)\, \varphi\, dx = \lim_{p\to 1} \int_\Omega u_p(\cdot,t)\, \varphi\, dx \leq \liminf_{p\to 1} \|u_p\|_{2,\Omega}.$$

Taking the supremum over all such φ allows us to conclude. ■

Chapter 4

Analysis of Diffusion in Curved Surfaces and its Applicationto Tubular Membranes

This chapter was published under this title in *Molecular Biology of the Cell* online October 2016, [15], at http://www.molbiolcell.org/content/27/24/3937.abstract .

1 Introduction

Lateral diffusion of proteins in membranes is ubiquitous and is known to play important roles in several cellular processes, including neuronal signaling, immunological reactions, receptor endocytosis, and many signaling pathways [50, 51, 52, 53, 54, 55] The diffusion of biomolecules in membranes is actively modulated in cells through several mechanisms, including actin barriers and active fluctuations [55, 56, 57, 58, 59, 60]. Diffusion of proteins in membranes is also sensitive to a number of factors, including the size of the protein, its confinement to domains, the viscosity of the environment, and crowding [61, 62, 63, 64, 65]. Classical studies on diffusion in cell membranes assume the surface to be planar and model diffusion in two dimensions [66]. This assumption, though valid in studying many phenomena, may not be correct in studying diffusion in membrane deformations [67, 68, 69].

Manifestations of curvature in membrane are ubiquitous and have observable biological functionality. For instance, curvature is highly regulated in development and retraction of outgrowths in neurons [70]. Many processes such as recruitment of proteins, changes in composition of lipids, and changes in membrane physical properties are curvature dependent [71, 72, 73, 74, 75, 76, 77]. Geometry is also known to play an important role in sorting of proteins. It has been hypothesized that the curvature of the transGolgi network (TGN) aids in protein sorting [72]. Interestingly, the relative concentration of proteins and lipids in the membrane and tubules emanating from the membranes are different [78, 79, 73].

This implies that molecular concentration in tubules and in the planar surface that they are connected to can be different, and this difference can have biological significance. Several researchers have elegantly shown that this sorting could arise through a variety of physical and biological mechanisms reviewed in [80].

As with most physical properties of biological systems, curvature and shape of various membranes and membrane-bound organelles are highly regulated [81, 82, 83]. In several cases, cells expend energy to maintain the geometry of these structures, as illustrated by recruitment of BAR domain proteins to sites of endocytosis [84]. Because geometry is tightly regulated in a cell, it is possible for the cells to modulate geometry to steer diffusion and concentration gradients. An important factor responsible for this, although less understood, is how biomolecules diffuse differently simply as a result of the nonplanarity of the surface [85, 86]. This influence of geometry on diffusion has been demonstrated for tubular geometries. Experimentally determined diffusion constants measured for a protein KvAP have been shown to be directly proportional to the radius of the tubule in which the protein diffuses [87, 12]. However, even the measurement of diffusion coefficients in nonplanar geometries could be inherently difficult due to the complexity of geometry [67, 88, 87, 89]. Thus there is a real need to develop models that accurately measure the diffusion of molecules in complex geometries.

In this paper, we examine how the geometry of a surface plays a role in diffusion of molecules and, consequently, how concentration gradients of diffusing species develop. To address this, we developed a numerical implementation of the Laplace-Beltrami mathematical model to understand diffusion in geometrically complex surfaces using membrane tubules as a biologically relevant example. Tubular membrane geometries are typical of many structures found in cells, including dendritic spines, the endoplasmic reticulum, membrane nanotubes, primary cilia, clathrin-independent carriers, and sorting tubules emanating from endosomes and the TGN [90, 91, 92, 72, 93, 94, 87, 95]. We report numerical simulations of the mathematical model that incorporate the cylindrical nature of tubules

and the effect of the cylindrical geometry on diffusion of molecules along the tubule surface. We show by adapting standard diffusion paradigms that geometry has a nontrivial influence on diffusion and thereby the concentration of molecules that diffuse into tubules. These mathematical considerations predict that nonplanarity of membranes prolongs concentration gradients across a tubular surface. The amplitude and temporal spread of the concentration gradient is systematically dependent on the curvature of the tubule and the diffusion coefficient of the molecule. Thus our results imply that biological regulation can emerge from a strategic coupling of these geometric constraints with the cellular sorting machinery.

2 Results

Diffusion in membranes has been characterized by a wide variety of theoretical techniques, including some that describe a tubular geometry [66, 96, 85, 86]. Many of these methods use random-walk simulations, which apply stochastic models to describe diffusion. While these methods have been highly successful in addressing many interesting biological questions, they only asymptotically solve the diffusion equation of inherent interest and so add an extra order of approximation. Therefore, to understand how diffusion scales with different geometric parameters on a tubular surface, we described classical motion of diffusion set on a surface. We then derived a Laplace-Beltrami operator for the diffusion equation and solved it using finite element methods (FEM) for a symmetric condition (Supplemental Text S1). See also Supplemental Text S2 for the more general case of nonsymmetric conditions.

We solved the Laplace-Beltrami equations to understand how various geometric parameters affect diffusion and thereby the concentration gradient of a diffusing species along the surface of a tubule for a prescribed boundary condition. A tubule is modeled as a cylinder with length h and radius r attached to a hemispherical cap of radius r. A cartoon representation of a tubule is shown in Figure 1A. We considered a range

of radii and lengths that mimic various dimensions of membrane tubules found in cells or generated in vitro (Table 1 and Figure 1C). The geometry of the tubule is assumed to be constant as a function of time. This implies that molecules diffuse into pre-existing tubules. Such tubules are common in biological systems. Unless otherwise specified, we assume that diffusing species enter the tubule from the open rim and diffuse into the body of the tubule. We want to emphasize that all diffusion conditions described in this paper refer solely to surface diffusion along tubules and not diffusion in the lumen of the tubule. A reservoir of molecules is assumed to be present outside the rim and available to diffuse into the tubule. Diffusion from the rim into the tubule occurs with a defined diffusion coefficient k, which falls within a range of values previously reported for membrane-associated proteins [97, 98]. Note that the model only considers the effects of geometric factors on diffusion. Thus the diffusing species have no explicit size or shape, the surface of the tubule does not have a defined thickness, and the regions inside or outside the tubule have no viscosity. Correspondingly, hydrodynamic effects are not included in this model.

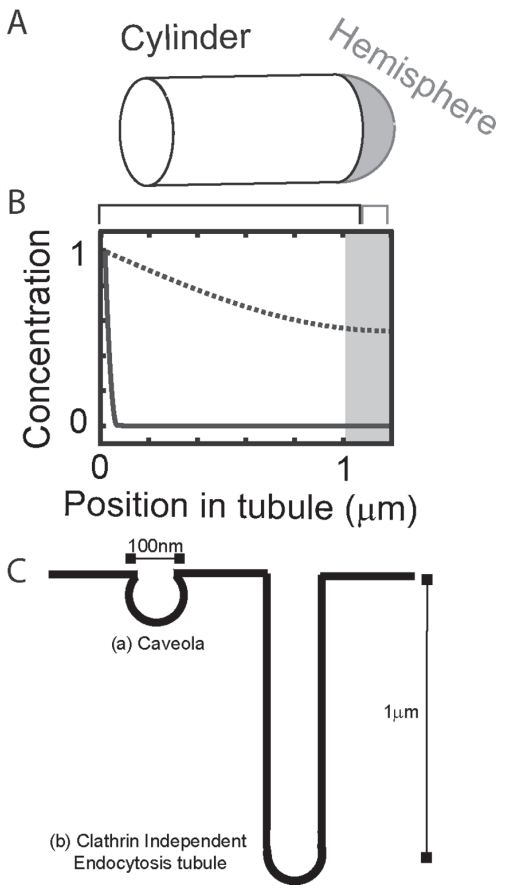

Figure 4.1: (A) A tubule is described as two geometric structures: a cylindrical portion (clear) and a hemispherical portion (gray). (B) Example of plots of concentration of diffusing species for a tubule with length 1 m and radius 200 nm. The shaded portion corresponds to the hemisphere region, and the white portion represents the cylindrical region of the tubules. The dotted and solid lines illustrate two different arbitrary concentration profiles. (C) Illustration of the difference in length scales of membrane tubules in biology.

Structure	**Radius(nm)**	**Height**	**Reference**
Calthrin-coated Pits	Pits 20-80; Coats 35-100		Kirchhausen, 2009
Caveolae	40-60	100nm	Westermann et al, 1999
Cholera toxin endocytic tubules	≤ 250	$5\mu m$	Day et al, 2015
Shiga toxin endocytic tubulues	≤ 250	$1 - 20\mu m$	Römer et al, 2007; Renard et al, 2015
Filopodia	100	$1 - 2\mu m$	Mogilner and Rubinstein, 2005
PACSIN2 tubes	10-100		Wang et al, 2009
Endophilin A2 tubulues	10-50		Farsad, 2001
Endoplasmic reticulum tubule	57		Upadhyaya and Sheetz, 2004
Golgi tubule	90		Upadhyaya and Sheetz, 2004
Inner mitochondrial tubule	18		Scorrano et al, 2002
Neurites	25-1250	$\geq 1\mu m$	Windebank et al, 1985; Briggman and Bock, 2012

Table 4.1: Examples of lengths and radii of membrane tubules.

To understand how material diffuses on the tubules as a function of time, we typically generate plots of the concentration of diffusing species along the length of the tubule, where the rim of the tubule is set as 0. Note that the coordinate system used in the figures is different from the coordinate system used while solving the Laplace Beltrami equation.

An explanation and the relationship between the coordinate system used in the figure and in the equation are described in Supplemental Text S3 and in Supplemental Figure 2. Examples of two possible concentration gradients are illustrated in Figure 1B. For these cases, the concentration of diffusing species is identical at the rim but differs along the length of the tubule.

3 How does geometry impact the time it takes for material to equilibrate along the surface of a tubule?

In subsequent sections, we simulate biologically relevant tubular dimensions and boundary conditions to understand how molecules in tubules diffuse. We expect the geometry of the tubule to control the diffusion of molecules along its surface in two ways. First, geometry should regulate the time it takes for a molecule to equilibrate completely across the length of the tubule. Second, geometry can influence how concentration scales spatially along the length of the tubule. We performed simulations to understand the magnitude of each of these effects. To carry out these studies, we considered tubule lengths and radii similar to those seen in biological membranes (Table 1 and Figure 1C). Diffusion coefficients ranging from 0.01 to 0.5 $\mu m^2/s$ were chosen to mimic those previously reported for membrane proteins [97, 98].

To investigate the impact of tubule geometry on the equilibration time, we simulated a condition in which the concentration of diffusing species within the surface of the tube is initially 0 except at the rim, where it is set as 1. We assume that the concentration of diffusing species available to enter the rim of the tube remains constant throughout the time course of the simulation. This boundary condition represents a unity Dirichlet data, and the simulations with this boundary condition are referred to subsequently as Dirichlet simulations purely for the sake of convenience. This represents a biological condition in which the surrounding membrane is saturated with molecules at all times. These molecules will then diffuse into the tubule until equilibrium is reached between the membrane and tubule.

We first characterized diffusion onto a tubule as a function of time under the Dirichlet boundary condition. For this, we selected a tubule with radius of 0.1 μm and length 1 μm and set the diffusion coefficient as 0.1 $\mu m^2/s$. We then simulated the concentration of diffusing material across the tubule surface at 0.25 s intervals for a total time of 10 s. Under these conditions, the magnitude of the concentration gradient across the tubule systemati-

cally decreases, and eventually the tubule fully equilibrates to a concentration of 1 (Figure 2A). Correspondingly, a plot of the average concentration of diffusing species in the tube saturates as a function of time (Figure 2B). From such plots, the half-time $t_{1/2}$ required for equilibration can be directly calculated.

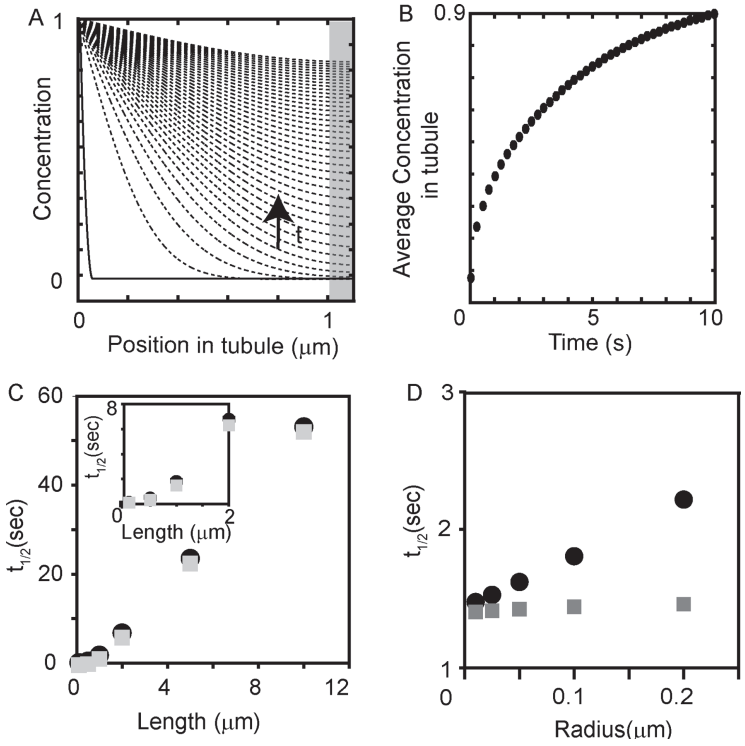

Figure 4.2: Variation of concentration along the tubule over time under Dirichlet boundary conditions. (A) Evolution of concentration gradients as a function of time for a Dirichlet simulation of molecules actively flowing into a tube of length 1 μm and radius 0.1 μm with a diffusion coefficient of 0.1 $\mu m^2/s$ shown for time steps of 0.25 s. The zero time point is indicated by the solid line and the subsequent time points are shown as dashed lines. The arrow indicates increasing time. (B) Change in average concentration of molecules in the tubule as a function of time for the case of the unity boundary conditions. (C) Half-time ($t_{1/2}$) required to fully equilibrate material along the entire tubule (black circles) or the cylindrical region only (gray squares) as a function of tubule length for a tubule of radius 0.1 μm. Inset shows $t_{1/2}$ for small lengths. (D) $t_{1/2}$ required to fully equilibrate material across the entire tubule (black circles) and the cylindrical portion only (gray squares) as a function of tubule radius for a tubule with length of 1 μm.

We next investigated how diffusion coefficient, tubule radius, and tubule length alter the equilibration time. For these studies, we varied each of the parameters individually, keeping the other two constant. First, we varied diffusion coefficients from 0.01 to 0.5 $\mu m^2/s$ on a tubule of length 1 μm and radius 0.1 μm for a total simulation time of 5 s. Not surprisingly, for faster diffusion coefficients (Supplemental Figure 3), the diffusing species equilibrates faster, while for slower diffusion coefficients, the equilibration is considerably slower. For example, diffusing species

with a diffusion coefficient of 0.5 $\mu m^2/s$ have a half-time of 0.5 s, whereas a 10-fold slower diffusion coefficient of 0.05 $\mu m^2/s$ yields a half-time of 4.5 s.

Next we simulated diffusion on tubules of variable lengths, assuming a constant radius of 0.1 μm and a diffusion coefficient of 0.1 $\mu m^2/s$. (Supplemental Figure 4A). While the shortest tubule (h = 0.1 μm) equilibrated rapidly, as expected, even lengths of 0.5 μm posed a significant barrier to the diffusion of molecules onto the tubule (Supplemental Figure 4B). To generalize how the length of the tubule affects equilibration, we calculated the half-time ($t_{1/2}$) of the tubule to equilibrate (Figure 2C). For tubules that had not reached half-saturation by the end of the simulation, we used extrapolation to obtain $t_{1/2}$. We found that $t_{1/2}$ is not linear for small lengths (Figure 2C, inset), but for lengths $> 2\mu m$, it increases linearly, since the contribution from the hemispherical region is negligible. We also determined the $t_{1/2}$ for the cylindrical portion only and found that this closely resembles the $t_{1/2}$ of the entire tube, especially for long tubules. When we attempted to do the same for the hemisphere, we found that, for longer length scales, the hemisphere was devoid of diffusers, and extrapolations were therefore not accurate. Thus these have not been reported here.

We next simulated diffusion in tubules with a constant length of 1 μm but radii ranging from 0.01 to 0.2 μm (Supplemental Figure 4D). These simulations were carried out for a time period of 5 s. As before, we determined the $t_{1/2}$ required for material to equilibrate along the entire tube or the cylindrical region (Figure 2D). The results of these simulations show that increasing the tubule radius from 0.01 to 0.2 μm slows down the entry of material onto the tubule. For example, the time it takes for the average tubule to become halfsaturated increases from almost 1.5 to 2.2 s when the radius is increased from 0.01 to 0.2 μm, translating to almost a 50 percent increase.

4 How does geometry influence the magnitude of concentration gradients across the surface of the tubules?

In the scenario outlined above, we considered a situation in which the material that enters the tubules is present at constant levels in the membrane reservoir. However, under some conditions, the concentration of material available to enter the tubes may itself vary as a function of time, for example, as the result of a chemical reaction or signaling event. To model this situation, we considered a second boundary condition, in which we assumed that the concentration of diffusing species is initially 0 both across the surface of the tube and at the rim at t = 0. A linearly increasing quantity of molecules was then added to the rim as a function of time, and the molecules then diffused onto the tubule. Because the flow is unity and increasing, this boundary conditions rep-

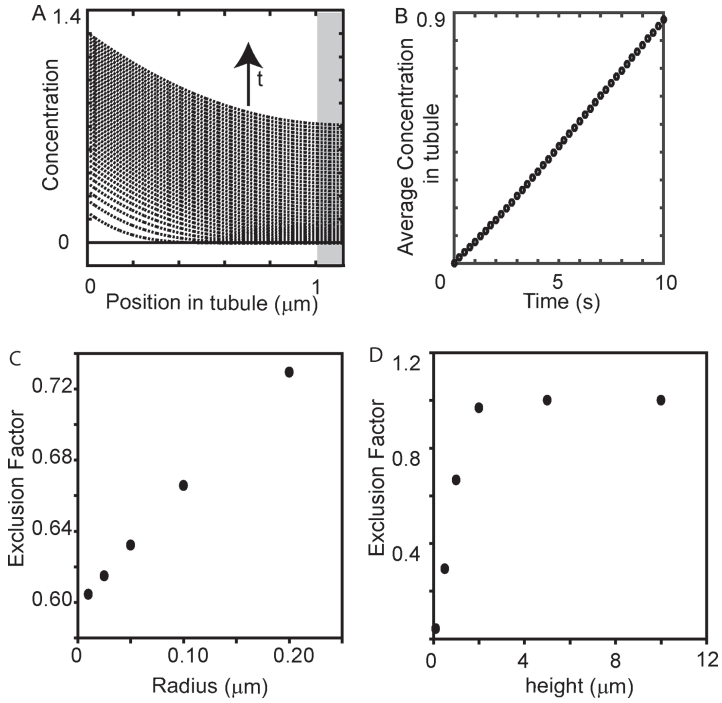

Figure 4.3: Variation of concentration along the tubule surface under Neumann boundary condition simulations. (A) Evolution of concentration gradients as a function of time for a Neumann simulation of molecules actively flowing into a tube of length 1 μm and radius 0.1 μm with a diffusion coefficient of 0.1 $\mu m^2/s$. The zero time point is indicated by the solid line and the subsequent time points are shown as dashed lines (time steps = 0.25 s). (B) Change in average concentration of molecules along the tubule surface as a function of time in the case of the unity Neumann boundary conditions. (C) Effect of changing the radius of a tubule on the exclusion factor for a molecule with diffusion coefficient of 0.1 $\mu m^2/s$ while keeping the length of the tubule constant at 1 m. (D) Effect of changing the length of a tubule on the exclusion factor for a molecule with diffusion coefficient of 0.1 $\mu m^2/s$ while keeping the radius of the tubule constant at 0.1 μm.

resents a unity Neumann data, and the simulations are henceforth referred to as Neumann simulations for the sake of convenience. We then examined how concentration evolves as a function of time for the same tubule dimensions and diffusion coefficients simulated for the Dirichlet boundary condition.

We first characterized how a typical Neumann boundary condition evolves by using as an example a molecule with a diffusion coefficient 0.1 $\mu m^2/s$ diffusing onto a tubule of radius 0.1 μm and length 1 μm. Figure 3A shows the concentration gradients along the length of the tubule as a function of time over 0.25 s time intervals (dashed lines) beginning at time t = 0 (solid line) for a total of 10 s. Unlike the Dirichlet boundary condition, here the concentration of material in the tubule grows without bounds as the result of the constant rate of influx of molecules at the rim for as long as that constant rate of influx is prescribed (Figure 3A). Consequently, for a given tubule, the overall shape of the gradient is maintained over time, and the total concentration rises linearly (Figure 3B). To provide a measure of the relative differences in concentration at the rim and the tip of the tubule at the end of these simulations, we define an exclusion factor term as

$$\text{exclusion factor } = \frac{C_0 - C_1}{C_0}$$

where C_0, C_1 are the concentrations of moleculus at the rim and at the end of the tubule. This factor ranges from 0 to 1, with 1 implying that the tubule bottom has 0 concentration and 0 representing an equilibrated state with equivalent concentrations at the tubule rim and tip.

To study how tubule geometry influences the way molecules are sorted into tubules, we varied the length and radius of the tubule and the diffusion coefficient of the diffusing species to determine the corresponding concentration gradients. We would like to stress that, in real biological systems, this condition would not continue indefinitely and would have an upper bound on the time up to which material flows. Hence we compare the con-

centration profiles and exclusion factor (Supplemental Text S4) between different conditions at a single time point (t = 5 s) for the different Neumann simulations. This time point was chosen arbitrarily to emphasize diversity in concentration gradients for the different parameters we compared. The flow rate was likewise held constant across our simulations.

First, we investigated how diffusion coefficients impact the evolution of concentration gradients across the surface of a tubule of constant length 1 μm and radius 0.1 μm for a simulation time of 5 s. Not surprisingly, as shown in Supplemental Figures 5 and 6, increasing the diffusion coefficient increased the absolute concentration of material present within the tubule. Interestingly, increasing the diffusion coefficient also decreased the exclusion factor (Supplemental Text S4). Thus the less mobile a molecule is, the less its gradient relative to the reservoir.

Next we studied the effect of tubule radius (Supplemental Figure 7A) by simulating molecules diffusing into tubules of a constant length 1 μm and diffusion coefficient of 0.1 $\mu m^2/s$ for a period of 5 s. For this analysis, we kept the concentration of molecules available at the rim for diffusion as a constant, implying that the total number of molecules available differs as a function of radius. We found that changing the radius does not substantially impact the underlying characteristics of the concentration profile in the tubule, although we did note that at the largest radius, r = 0.2 μm, a concentration gradient was present at the bottom of the tube. This presumably reflects the fact that the radius is comparable to the tube length. As the tube radius was decreased, a higher density of molecules accumulated in the bottom of the tubule. This behavior is also reflected in the exclusion factor increasing linearly with increasing radii for this range of values (Figure 3C).

Finally, we varied the length of the cylindrical region to determine the effects of tube length. We varied the tubule length over two orders of magnitude ranging from 0.1 μm up to 10 μm with a constant tubule radius of 0.1 μm under the Neumann boundary condition. We observed that overall concentration gradients are different for different tubule lengths with identical radii (Supplemental Figure 7B). As seen from the exclusion factor (Figure

3D) for very small length scales, for instance for h = 0.1 μm, the length is sufficiently small for the entire tubule to be exposed to diffusing molecules within 5 s, resulting in a relatively uniform concentration across the entire tubule. The plateau seen in the exclusion factor occurs because material has not yet reached the hemispherical region and, hence, for these geometries at this time point, the exclusion factor would remain the same. In the case of long tubules, the hemisphere and even some portions of the cylindrical region are not even exposed to the diffusing molecules. However, length of the tubule, more than radius is a chief contributing factor in determining the exclusion factor.

5 Comparison of diffusion of molecules in a tubular surface and a flat surface

Until now, we have compared the diffusion of molecules along a tubular surface of various dimensions. To understand the importance of tubular geometry on diffusion from a more general perspective, it is useful to compare diffusion on a tubule to diffusion on a flat surface. Such a comparison requires one to define a geometrically comparable noncurved surface. However, due to Gaussian curvature obstructions, we cannot expect these systems to be pointwise comparable in the mathematical sense of isometric equivalence. A Riemannian isometry would erase the very local curvature differences we aim to explore. Instead, we design surfaces that are comparable by enforcing that they share a common amount of total material (area). By this, we preserve global area, and the same total area is available to diffusion in both systems, though in one it is shaped like a curved tube and in the other like a flat disk. In this sense, differences in diffusion are solely due to differences in curvature between the systems. We designed such a control by defining a planar disk containing an outer annulus with an area corresponding to the cylindrical area of the tubule and an inner circular region with an area equal to the hemispherical region of the tubule (Supplemental Text S1 and Supplemental Figure 8).

In this manner, the vertical tube and flat annulus respectively surround the hemisphere and corresponding disk in two and three dimensions. We then described the flat surface

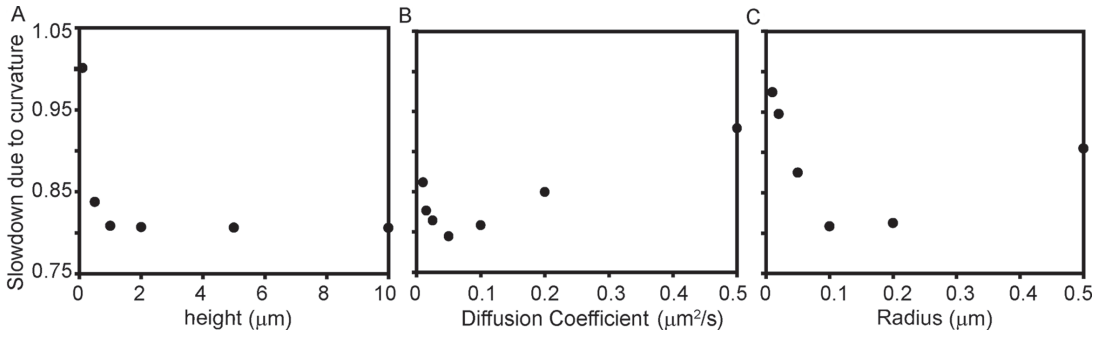

Figure 4.4: Comparison of concentration gradients in flat surfaces and in tubules. Slowdown of diffusion in the tubular geometry was quantified at the rim of the hemisphere-cylinder junction as slowdown $= \frac{(C_0 - C_{.25})_{\text{tubule}}}{(C_0 - C_{.25})_{\text{flat}}}$ t = 0 s and t = 0.25 s. (A) Effect of tubule length with tubule radius and diffusion coefficient held constant at 0.1 μm and 0.1 $\mu m^2/s$, respectively. (B) Effect of diffusion coefficient with tubule radius and length held constant at 0.1 and 1 μm, respectively. (C) Effect of tubule radius with tubule length and diffusion coefficient held constant at 1 μm and 0.1 $\mu m^2/s$, respectively.

using the same coordinate system used to describe the tubules.

Using this equivalent geometric description, we simulated conditions to compare diffusion in curved tubes with that on comparable planar disks. To carry out these simulations, we used an initial condition in which the molecules were present uniformly in the hemispherical region or its corresponding planar region and allowed them to diffuse into the cylindrical region or its flattened equivalent for a total time of 5 s. Thus, unlike the previous simulations, where the material diffused from the open rim of the cylindrical region of the tubule, in these simulations material diffuses from rim of the hemisphere into the cylindrical region of the tube. The initial value of concentration was arbitrary set at 1000 U. In addition, these simulations have a closed boundary condition, in that the molecules do not flow out of the tube.

We performed the simulation with the initial boundary conditions described above, except that, in this case, the hemisphere contained a uniform concentration of diffusing species at t = 0. Thus, for these simulations, the concentration gradient should dissipate outward toward the tubule rim given sufficient time. However, comparison of the diffusion as a function of time between two distinct geometries could be extremely arbitrary.

At the start of the simulation, the two conditions have similar concentration, and in many cases, both the tubule and the flat surfaces could be completely equilibrated at the end of the simulation. Hence it becomes important to compare them using a temporally equivalent parameter. Similarly, the difference between the two geometries could be spatial as well. Therefore, to compare the rate of dispersal of material between the two different geometries, we introduce a slowdown parameter, which incorporates both the spatial and temporal components as a single measure. This is calculated at the rim of the hemispherecylinder junction as

$$\text{slowdown} = \frac{(C_0 - C_{.25})_{\text{tubule}}}{(C_0 - C_{.25})_{\text{flat}}}$$

between time t = 0 s and t = 0.25 s (the first time step in these simulations). The numerator terms, C_0 and $C_{.25}$, denote the concentration at the junction of the two surfaces (cylinder and hemisphere) for the tubule for times t = 0 and 0.25 s, respectively, while the denominator denotes the concentration at the intersection of the two concentric annuli of the flat surface for the same two time steps. The slowdown parameter is in essence the ratio of how fast molecules can diffuse out of a tubular surface compared with a flat surface. By this measure, a value of 1 indicates the tubule and the flat geometry match. While this quantification of slowdown is arbitrary, it enables us to study the relative effects of flat versus tubular geometries on diffusion. The slowdown parameter is explained in detail in Supplemental Text S5.

As before, we varied the three parameters of interest (radius, length, and diffusion coefficient), but in this case, we carried out simulations for both flat and curved surfaces. In every case examined, we found that, compared with the flat geometry, the loss of material from the hemisphere was slowed in the tubular geometry (Figure 4). In some cases, the magnitude of this effect was nearly 20 percent. When we increased the length of the tubule, the effective slowdown due to tubular geometry reached an asymptotic value. This is because the effect of hemispherical region is minimal for lengths greater than 1 μm, and thus all longer tubules behave identically at the early time points. However, the effects of

radii and diffusion coefficient were nonsymmetrical paraboloids, suggesting that a complex relationship exists between these parameters.

6 Comparison with experimental results

To assess the validity of our models, we compared our simulations with a recent experimental work by Aimon et al. (2014), [12], who measured diffusion of proteins in membrane

tethers connected to a giant unilamellar vesicle using a fluorescence recovery after photobleaching (FRAP) assay. In these experiments, an entire tubule of a defined length and radius was photobleached and allowed to recover (Figure 5). The diffusion coefficient was then determined using a theoretical solution for diffusion in the special case of a long, thin cylinder connected to a sphere that acts as a reservoir for the diffusing molecules (Berk and Hochmuth, 1992). Both experiments were performed on tubes with a length of 6 μm but slightly different radii of 30 and 20 nm and contained two different proteins whose diffusion coefficients were quantified as 0.73 and 0.38 $\mu m^2/s$.

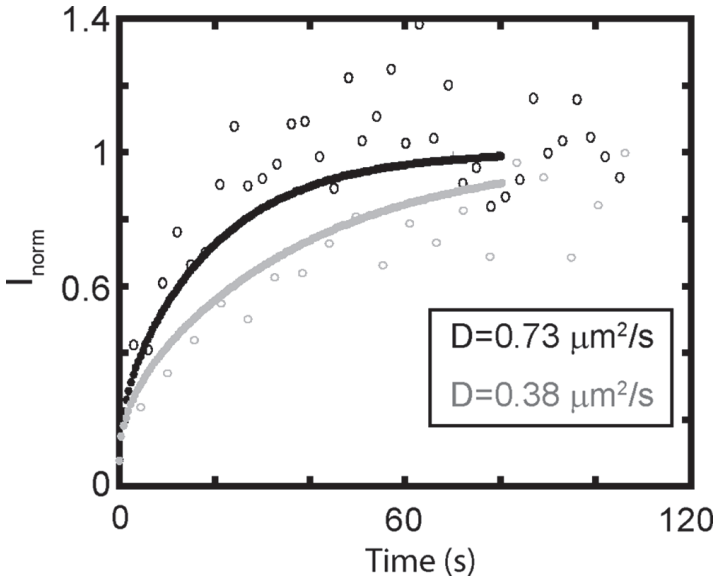

Figure 4.5: Comparison of simulated diffusion with previously published experimental data (Aimon et al., 2014). The experimental recovery curve data are adapted from Figure 3 (gray circles) and Figure S3B (black circles) of Aimon et al. (Original data depicted in the figure as gray/black open circles and the diffusion coefficients were kindly provided by Patricia Bassereau, Institut Curie.) The open circles denote the original FRAP data from the paper, and the lines denote the recovery curve from the simulation, adapting the geometry and diffusion coefficients measured in the paper.

To compare these experimental photobleaching data with our diffusion model, we simulated diffusion on these exact geometries using the experimentally determined diffusion coefficients. We assumed that, at time t = 0, the tubule contains no diffusing species except at the rim, which is attached to a reservoir with a uniform concentration of one. We simulated diffusion into the tubes for 80 s and then calculated the average concentration of diffusing species across the tubule surface over time. The data obtained from the simulation closely agree with the data obtained experimentally (Figure 5). Thus our simulations capture this special geometric scenario, corroborating our approach using the finite element model for solving the Laplace-Beltrami equation.

7 Discussion

Understanding how geometry influences diffusion of molecules on membrane surfaces has important cell biological implications. In this paper, we have developed a mathematical framework to describe how geometry influences diffusion using a tubular surface as a model system. This geometry occurs in a number of biologically important structures, including primary cilia, dendritic spines, endosomal tubules, and clathrin-independent endocytic carriers. For diffusion along the curved surface, the local area available for diffusion is different relative to a flat surface. This gives rise to a strong dependence of diffusion on the tubule geometry. We examined three key parameters that can potentially influence diffusion – the tube radius, the length of the tubule, and the diffusion coefficient of the diffusing species – using a range of biologically relevant values of these parameters. We found that each of these variables plays a distinct role in regulating diffusion, depending on the boundary conditions. We also compared diffusion in tubular structures with that in a comparable flat surface and showed that the tubular geometry slows down diffusion.

The model described in our paper represents a significantly different approach for understanding diffusion in surfaces with complex geometries compared with many other earlier models that typically use random-walk motion and escape times of molecules to

determine geometric effects on diffusion [85, 99, 80, 100, 101, 102]. Our model represents a simple but fundamental formulation of a diffusion equation in a static tube. Compared with random-walk approaches, in which the only modeling degree of freedom is the random variable describing the walk of an individual particle [103], a diffusion equation based method requires less restrictive assumptions about individual particle motions. In our model, the dynamics at the boundary are prescribed and not merely observed, and the a priori knowledge of the boundary reconstructs the system behavior. An alternate approach to solving diffusion equations would be to use analytical approaches. This approach is typically not feasible for complex geometries and boundary conditions. In case of a tubule, for example, the adjoin of the hemisphere and tube disallows the use of analytical methods due to the need to knit the solutions across the boundary of the two geometries. To obtain a solution in the whole tubule (i.e., across the separating boundary), one has to ensure continuity of the solution and continuity of fluxes across such a boundary. Enforcing such conditions could result in at least one of the two problems (in their own regions) being overdetermined. Iteration techniques typically lead to issues of convergence, and the limit may not be expected to be explicit in some topologies. In this paper, we have sought to present a method that may be directly applied to many future real-world geometries of interest. In these cases, numerical methods will be the only realistic recourse for determining solutions. Further, to broaden the scope of usage of our model, we have implemented another parallel approach of solving the LaplaceBeltrami using virtual coordinates, and this has been described in Supplemental Text S2. Thus, compared with the 1-D used in the simulation, this framework can model more general boundary conditions such as asymmetric initial boundary conditions (Supplemental Figure 1C), and the models presented here can be applied to any arbitrary surface geometry and boundary condition.

In this study, we focused on understanding how geometric effects impact concentration gradients under conditions that are relevant to tubular structures found in biological membranes. We acknowledge that this description is still incomplete, as other factors could

potentially impact how concentration gradients evolve for a given tubule geometry and diffusion coefficient. The most prominent of these factors that are not included in the present model is the effect of hydrodynamics [104, 105, 106, 107]. Membranes can be approximated as a viscous fluid enclosed by fluids on both sides. Recent studies have shown that hydrodynamics vary as a function of tubule geometry for membranes [88, 75, 108, 87], which in turn could alter the way molecules diffuse in tubules. Similarly, our model does not account for the size of the diffusing species, which could also be critical for understanding diffusion in a real membrane [109]. Earlier experiments have shown that the protein and lipid composition of membrane tubes themselves can be curvature dependent, which could potentially introduce additional constraints on diffusion [80, 12]. To delineate these factors from differences arising purely from geometry, we have included a program (Supplemental Text S6) that can determine the expected diffusion coefficient given $t_{1/2}$ (as measured in FRAP experiments) for concentration equilibration for a given tubule geometry. Comparison of diffusion coefficients obtained from the simulation with those obtained from other empirical models [96] that incorporate factors such as hydrodynamic effects [88] will decouple these two factors. In the case of long thin tubules, our simulated diffusion profile resembles but is not identical to the experimentally observed diffusion profiles [12], as demonstrated in Figure 5. In the two examples, we see that the difference in $t_{1/2}$ as predicted from our model is 20-30 percent different from the experimental values using an empirical model for this particular case [96]. The discrepancy between the two values could potentially arise from hydrodynamic effects.

Even just using first principles and varying only relative geometry, we can make several interesting predictions about material flow and concentration gradients arising from diffusion in tubules with relevance to biological processes occurring in membranes. One such prediction is that diffusion of a particle in a tubular structure appears to be slower than its diffusion in a flat surface, simply as a consequence of geometric effects. This can be thought about as a loss of freedom due to the constrained geometry imposed by the cur-

vature. Thus, while the total areas of the tubular and the flat surface are equal, the local area for the diffusion of molecules is reduced in a tubular geometry due to radial curvature, thus prolonging the gradient. This effect could potentially explain recent observations that diffusion of membrane proteins is slower in tubules than the surrounding flat membranes in vitro [87]. The predicted slowdown also confirms other theoretical works by groups who have investigated diffusion in curved surfaces. For instance, Kusters and Storm (2014) [102], using random-walk simulations of single particles diffusing on tubes, have shown that curved surfaces retain molecules for an increased period of time before the molecules escape. The predicted slowing down of diffusion due to curvature effects was shown to influence receptor egress from the dendritic spine [86]. This is analogous to the retention of a concentration gradient along the tubule length due to its inherent curvature. Most models and experiments assume that the changes in diffusion with curvature are due to the altered diffusion coefficients of molecules [96, 87, 110, 12]. However, from a fundamental standpoint, our results show that geometry itself can also contribute to such effects. This delineation between diffusion coefficient changes and geometric slowdown is a critical, yet underrealized aspect of diffusion that readily emerges from our work.

Our model also predicts a priori the conditions that would increase the entry or retention rate of molecules in tubules. Because the tubular nature of the membrane stretches out the concentration gradient temporally, it leads to an interesting hypothesis, that is, cells can tune the geometry of tubes as a mechanism to regulate the entry and exit of membrane-associated cargo. Modulation of concentration gradients could potentially be one reason why curvature in membrane tubules is tightly regulated by proteins such as BAR domain proteins [84, 111, 112]. Of the three parameters we examined (tubule length, tubule radius, and diffusion coefficient), within the limits of biological molecules, we found that tubule length was a key parameter affecting the equilibration of material across the surface of tubules. Variation of tubule radii found in cells could change equilibration times by almost 50 percent, and we expect this factor, along with hydrodynamics [87], to also play a crucial

role in setting up concentration gradients. Based on these findings, we predict that entry of membrane-bound cargo into tubes should occur most slowly in the case of slowly diffusing molecules moving into long tubes with large radii. Such a mechanism could potentially slow down the intake of cargoes to allow the cellular machinery the time to respond, for example, by scissioning the tubules and thus decoupling them from the membrane reservoir. This type of kinetic sorting model has been proposed to regulate the entry of the $\beta 2$ adrenergic receptor ($\beta 2$AR) into a specific class of endosomal tubules [113]. In that study, $\beta 2$AR was shown to diffuse four times more slowly than another cargo protein, transferrin receptor, on endosomal membranes. Consequently transferrin receptor was able to enter into endosomally derived bulk recycling tubules more rapidly than $\beta 2$AR could. These bulk recycling tubules scissioned from the endosomal membrane relatively rapidly, thus disfavoring the entry of $\beta 2$AR. Instead, $\beta 2$AR tended to accumulate in a longer-lived specialized class of endosomal tubules stabilized by actin. Interestingly, the $t_{1/2}$ for $\beta 2$AR to recover on a small region of the endosomal membrane by FRAP was 25 s. This is comparable to the lifetime of the short-lived bulk-recycling tubules ($<$30 s) [113]. Thus, even though the concentration gradients that develop across the tubules are transient, their temporal evolution ultimately has a significant biological impact on sorting.

Another prediction of our model is that, in situations in which increasing concentrations of cargo are available to flow into tubes, a concentration gradient along the length of the tube would be set up almost immediately. The geometry of tubes also dictates the temporal evolution of the shape and the magnitude of the concentration gradient along the tube surface. Such concentration gradients could play a biological role in clathrin-independent endocytosis of AB5 toxins. These toxins not only drive the formation of tubular endocytic structures but are also known to change membrane physical properties in a concentration-dependent manner [94]. The cell could in principle couple the geometry of the tubule with the regulation of endocytosis to sense the cargo concentration in the tubule.

In summary, we have developed a generalizable model of diffusion in tubular geome-

tries from fundamental diffusion equations and have simulated diffusion for various biologically relevant boundary conditions and parameters. Our findings emphasize that sorting and concentration gradients can be initiated merely by the presence of curvature in the system, without requiring that the surface embedded molecules themselves exhibit curvature preferences. These results provide a framework for modeling diffusion in complex surfaces and suggest new numerical models for how biological functions could emerge as a consequence of the nature of diffusion in tubular geometries.

8 Materials and Methods: Finite element approximations and simulation details of Laplace-Beltrami equations

We first derived a LaplaceBeltrami equation (Eq. 5 in Supplemental Text S1) for tubular surfaces. We would like to emphasize that complementary approaches for deriving the equation of continuity can be found elsewhere (Marsden et al., 1984; Frankel, 2011). To solve this equation for a tubular surface, we have developed a univariate FEM solver (Oden, 2006). This FEM solver is designed for tubular diffusion under symmetric conditions, that is, all prescribed solutions are independent of the angle about the tubes center axis. Consequently the data depend only on the position along the tubes center axis. Under such symmetric conditions, the tubular diffusion has only a single degree of freedom and is modeled in a univariate setting. The symmetric tubule diffusion using defined virtual coordinates reduces to the form $u_t - k\left[A(x)u_x\right]_x = 0$ for specific forms of $A(x)$ determined by the tube's geometry. This is then solved using our 1-D FEM solver. The numerical solution is computed by semidiscrete methods. First, the uniform mesh and approximating spline space are user specified. As the basis of the symmetric solver, we use normalized B-splines $S_d^r(\Delta)$ [16]. Generally their use increases approximation power and, unlike other methods such as nodal basis elements, avoids artifacts such as negativity while smoothing the splines. We then use the DeCastlejeau algorithm for the evaluation of the B-splines without having to construct individual basis spline in the $S_d^r(\Delta)$ space. Then a Galerkin procedure is

implemented. The integration is accomplished through a Gaussian quadrature exact up to polynomials of degree 11. For example, when the approximation is conducted in any of the recommended spaces $S_1^0, S_2^1, S_3^2(\Delta)$, the quadrature is exact. The remaining temporal part is then handled using Matlabs ODE45 solver. All our simulations were performed using Matlab R2014/R2015a on Windows computers. A more general two-dimensional code capable of handling even asymmetric boundary conditions is described in Supplemental Text S2. Finally, as a note, we do remind readers that numerical approximation of this model is entirely a different problem to solve and this is independent from the models theoretical justification and derivation. We have included ways to improve numerical solutions and avoid artifacts due to approximation in Supplemental Text S7.

9 Availability of the Code

The complete code has been made available online at https://my .vanderbilt.edu/kenworthylab/fem-software-for-diffusion. We have also included, as a part of the code, a diffusion coefficient mapper for FRAP experiments of tubules that, given the height, radius, and $t_{1/2}$ will give out the diffusion coefficient. Instructions for use of the code are given in Supplemental Text S6.

Chapter 5

Bridging Across Physical Scales: Homogenization and Concentrating Capacity Applied to Cone Visual Transduction

1 Comparative Advantages and Disadvantages of Wetbench versus Numerical Approaches in Cone Visual Transduction Models

1.1 The Signalling Cascade.

Visual transduction is a prototypical, system's biology example of a G-protein mediated signalling cascade. It is reviewed in [17, 114, 115]. Paradigmatically, rods and cones operate similarly though their kinetics are often quite different as are sometimes the proteins involved specific to one photoreceptor or the other.

Light acts as a ligand and triggers a conformational change in the cis retinal attachment of Rhodopsin, or Opsin in cones. Upon activation the G-protein coupled receptor Rhodopsin diffuses along a discal face and activates the G-protein Transducin which in turn activates the effector Phosphodiesterase. All these processes occur in the face of a membrane disc, naturally described as a two dimensional surface.

The activated effector, however, begins to hydrolyze the 2nd messenger cGMP, which lives in the volumic cytosol with its partner 2nd messenger Ca^{2+}. Their diffusion occurs in a distinct and dimensionally different domain than that of the GPCR, G-protein, and effector. As cGMP drops, gated channels sensitive to the levels of cGMP begin to close reducing a Na^{+} and Ca^{2+} current. This current drop is regarded as the chief output of a visual receptor's detection of light.

At the same time recovery processes begin to deactivate the GPCR. As the concentrations fall, Recoverin – Visinin in cones – is increasingly less bound by Ca^{2+} which allows the Rhodopsin Kinase to begin phosphorylating the GPCR. With successive phosphoryla-

tion the GPCR diminishes its catalytic activity for G-protein and increases its affinity for Arrestin. Upon binding with Arrestin, the GPCR is no longer able to activate G-protein for the duration of the photoresponses considered here. Cones are thought to possess two types of Arrestin, one of which may form shorter lived, more transient complexes than the other. It is speculated this may contribute to cone adaptation under continuous light illumination [17]. Both phosphorylation and Arrestin binding are stochastic events in contrast with the cytoslic diffusion of the 2nd messengers which is modeled deterministically. [116] takes 6 phosphorylation sites in rods. In the presence of less information with cones, the numerical experiments here modeled with a single step to Arrestin shutoff.

The G-protein effector complex deactivates through GTP-ase decay which is accelerated in cones through an increase of RGS9 expression. cGMP concentration is restored to its dark value through synthesis by Guanylate Cyclase. This synthesis of cGMP is accelerated in recovery through stimulus by Mg^{2+} bound GCAP's. Under dark conditions the GCAP's are Ca^{2+} bound and inhibited. The return of cGMP to dark levels reopens the gated channels and restores Ca^{2+} to its dark value.

1.2 Making the Case for Numerical Experimentation.

Historically, rod photoreceptors were fairly practical to isolate and their proteins to purify. This was done first from bovine retinas [114]. Through purification, experimentalists were able to isolate individual elements of rod transduction machinery and quantify their *in vitro* activation and deactivation rates as well as their native expression levels. This work is responsible for producing a large literature on the kinetics of rod biochemistry [117]. Except for some farily recent experimental designs however, see [118], cones have proven much more difficult to isolate and their proteins to purify. As a consequence, there is less literature and consensus on the kinetics demonstrated in cone photoreceptors.

Due to its inherent complexity, the visual cascade's processes are best regarded as a synergistic outcome of all their individual parts working in tandem. To understand the

relative importance of each part to its cascade, it would be best to study each part always in that context and not artifically extracted from it. Though possible, single cell recordings of cones are difficult to obtain [119]. Knockouts and genetically modified animals may be used to change the underlying biochemical kinetics in photoreceptors *in vivo*; however, that does not overcome the technical difficulty involved in isolating cones. Inevitably, too, this approach incurs costs both financially and in time. The animals must be bred and allowed to mature. Though scientists can control which genes are expressed, this control is not so surgical as to specify individual kinetics parameters at will for example.

Numerical experiments, conversely, supplement the indispensable work of experiments in the aforementioned areas. Once the interactions of a system have been encoded by a numerical model, the kinetics are very easily manipulated in real time through the adjustment of model parameters. Virtual genetic experiments can be conducted at essentially no financial cost and reduced amounts of time. Access to kinetics in numerical models *is* surgical, and individual components of the cascade may be altered with guarantee that no other biophysics is changed. Geometric variables may also be precisely manipulated. For example in cones, the consequences of the cGMP channels residing in different locations can be explored. The numerically modeled responses of the cone with channels in specified locations may be compared to one another to help shed light on where the channels physically reside.

2 Statement of the Non-homogenized Pointwise Diffusion of cGMP and Ca^{2+}.

2.1 The Geometrical Domain of Cone Photoreceptors.

Take a standard right cone with vertex angle α and R its greatest radius. Starting at the cross section of radius R mark a height of H along the cone's axis. Let r be the radius of the cross section found at H. This object now constitutes an initial truncated cone $\mathscr{C}$.

The datum ω_0 will be understood to mean an angle drawn at the origin of the xy plane

rotating out of the x-axis in a counter-clockwise direction. The values $\nu, \sigma, \varepsilon_0$ are arbitrary but fixed parameters except that ε_0 is subject to the integral restriction $n = \frac{H}{\varepsilon_0(1+\nu)} \in \mathbb{N}$. This ensures the number of chambers and interdiscal spaces are integers.

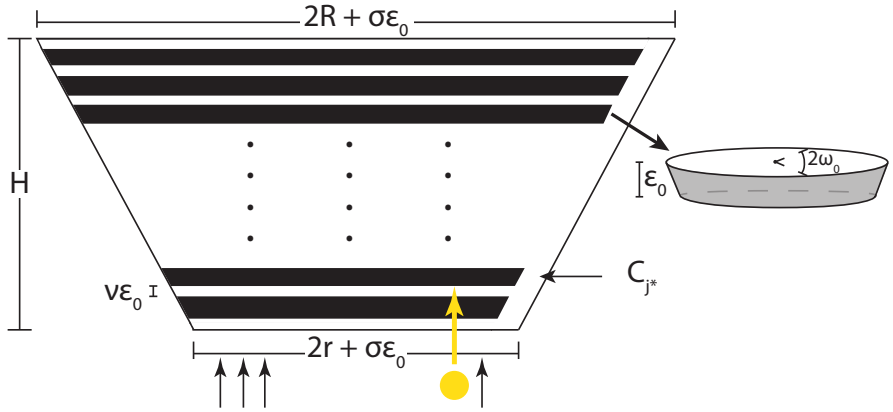

Figure 5.1: The nonhomogenized geometry is a cone with excised discal pieces and a sliver over a partial angle $2\omega_0$ of the rim.

For the given ε_0 and geometrical data, we will build a corresponding domain Ω. Along the height of the truncated cone take tick marks: the first and last are interdiscal heights of $\frac{1}{2}\nu\varepsilon_0$ and in between the sizings alternate in ε_0 $\nu\varepsilon_0$ pairs, ie disc to interdiscal space. Those segments of length ε extend outward to fill regions of the truncated cone which we designate the C_j's. We excise these regions form $\mathscr{C}_0 = \mathscr{C} \setminus \bigcup_j C_j$.

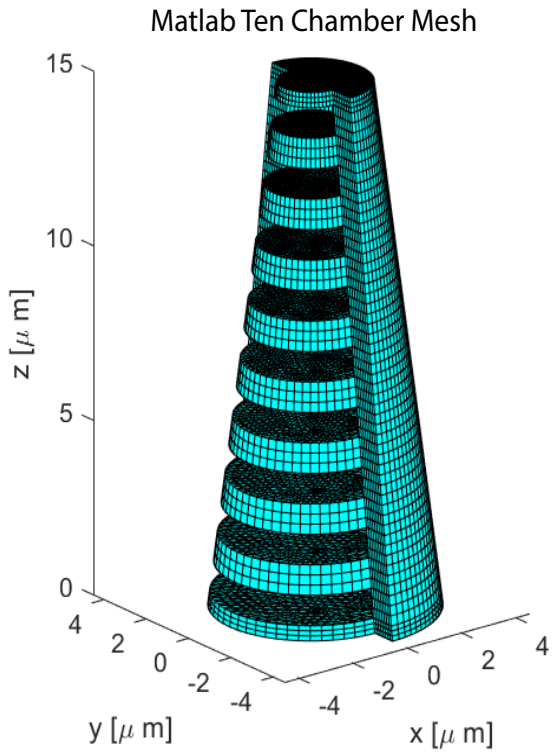

Figure 5.2: A Matlab generated nonhomogenized, 10 chamber geometry. In actual simulations, the number of chambers varies from 100-500. In this figure, the sliver size is exaggerated.

By inspection we see that

$\mathscr{C}_0$ is a disconnected stack of equispaced and equiheight conical cuts of $\mathscr{C}$ except for the first and last interdiscal space.

Recall the angle ω_0 defined earlier. A cone of angle α may be regarded as a volume of revolution about the z-axis, where the outer boundary of the rotated, planar region is a line emanating from the origin and with slope $\cot(\alpha)$.

To this interior region we now will attach a connecting sliver which models the geometric membrane. Take the vector direction $e_{\rho_{\text{cyl}}} = (\cos\theta, \sin\theta, 0)$. Over the angle range spanning $[-\omega_0, \omega_0]$ about the z-axis extend the cone along e_ρ in the length $\sigma\varepsilon_0$. Call this sliver $\mathscr{S}$.

The promised domain Ω we set equal to $\mathscr{C}_0 \bigcup \mathscr{S}$. It is comprised by a stack of conical cuts occupying our original truncated cone $\mathscr{C}$, with heights and separations of small order $O(\varepsilon_0)$. These chambers we hereafter refer to as the I_j's. They are connected only at the boundary of our cone along the angles $[-\omega_0, \omega_0]$, taken about the z-axis, and through the sliver possessing radial width also of $O(\varepsilon_0)$ order.

2.2 The Nonhomogenous, Pointwise Diffusion Law for the 2nd Messenger cGMP and Ca^{2+} System.

Let the volumic concentration of cGMP and Ca^{2+} be denoted respectively by u and v. The parameters referenced below are defined in Table 5.3-5.5. Let z_0 be a site level of photon absorption. Then the concentration of cGMP is governed by the diffusion law

$$u_t - D_{\text{cG}}\Delta u = 0 \tag{2.1}$$

with $u(\cdot;0) = u_0$, which is the dark equilibrium concentration of cGMP, and Neumann data

$$D_{\mathrm{cG}}\nabla u \cdot n = \begin{cases} -\frac{1}{2}\nu\varepsilon_0\Big(\beta_{\mathrm{dark}}u - f(v)\Big) - \chi_{[z=z_0]}uf_1(v;x;t) & \mid \text{on } \partial I_j^+ \\ -\frac{1}{2}\nu\varepsilon_0\Big(\beta_{\mathrm{dark}}u - f(v)\Big) & \mid \text{on } \partial I_j^- \\ 0 & \mid \text{on } L_j \text{ and } \partial\Omega_S \end{cases}$$

Note the factor $\frac{1}{2}\nu\varepsilon_0$ is a conversion factor to express volumic concentrations as surface densitites. Also, the above variational data is for a single photon isomerization. In the case of several photons, the $uf_1(v;x;t)$ hydrolysis term is present at each isomerization point. The role of $f(v)$ and $f_1(v;x;t)$ is to encode the cone biochemistry:

$$f(v) = \alpha_{\min} + \frac{\alpha_{\max} - \alpha_{\min}}{1 + (v/K_{cyc})^{m_{cyc}}}$$

expresses the synthesis of cGMP by guanylate cyclase. This synthesis is Ca^{2+} dependent due to the calcium inhibited GCAPS becoming magnesium activated and stimulating the cyclase.

$f_1(v;x;t)$ expresses the hydrolysis of cGMP due to light activated PDE. It encodes the activation and deactivation of the GPCR, G-protein, and effector at the activation disc. It does not have an explicit functional form. Rather it, too, is modeled through a series of diffusion processes [120]. In particular when a model where Rhodopsin is taken to have multiple phosphorylation sites is used, the deactivation process is modeled stochastically: Activated Rhodopsin generates G-protein which in turn diffuses throughout the activation disc. This leads to the equations

$$\begin{aligned} \frac{\partial [G^*]}{\partial t} - D_G\Delta_{x,y}[G^*] &= \sum_{j=1}^{N} \nu_j \chi_{[t_{j-1},t_j]}(t)\delta_{\mathbf{x}(t)} - \nu_{GE}[E][G^*] \\ \frac{\partial [E^*]}{\partial t} - D_E\Delta_{x,y}[E^*] &= \nu_{GE}[E][G^*] - k_E[E^*] \end{aligned}$$

Here $[E^*](x,y,z,t) + [E](x,y,z,t) = [E](0)$ due to mass conservation. The ν_j's are the catalytic activity of j-times phosphorylated GPCR which decreases exponentially in accordance with (6) of [116]: $\nu_i = \nu_{RG} e^{-k_\nu (i-1)}$. The t_j denote the random sojourn time intervals of the activated rhodopsin in each phosphorylation state. The $\mathbf{x}(t)$ is the position of the GPCR on the disc. Finally,

$$f_1(v;x;t) = k^*_{\sigma,\text{hyd}}[E^*]$$

While the code is written to handle the full generality of stochastic deactivation, for cones, the simulations use only a single step to Arrestin binding, and the time before Arrestin binding is deterministically taken to be the mean sojourn time. The activated Rhopdopsin is taken at a fixed position in space throughout time.

The concentration of Ca^{2+} is governed similarly by

$$v_t - D_{\text{Ca}} \Delta v = 0 \tag{2.2}$$

with $v(\cdot;0) = v_0$, which is the dark equilibrium concentration of Ca^{2+}, and Neumann data

$$D_{\text{Ca}} \nabla v \cdot n = \begin{cases} -g_1(v) + g_2(u) & \mid \text{ on } \partial\Omega_S \\ 0 & \mid \text{ on } \partial I_j^{\pm} \text{ and } L_j \end{cases}$$

In this case, the functions g_1, g_2 encode the efflux and influx of Ca^{2+} due to an exchanger and also the cGMP-gated channel. They are given explicity by

$$g_1(v) = \frac{1}{B_{\text{Ca}} \mathscr{F}} J_{ex} = \frac{1}{B_{\text{Ca}} \mathscr{F}} \left(\frac{j_{\text{ex}}^{\text{sat}}}{\Sigma_{\text{cone}}} \frac{v}{K_{ex} + v} \right)$$

which is a Michaelis-Menten relationship expressing the calcium efflux through its exchanger, and

$$g_2(u) = \frac{1}{B_{\text{Ca}} \mathscr{F}} \frac{1}{2} f_{\text{Ca}} J_{cG} = \frac{1}{B_{\text{Ca}} \mathscr{F}} \frac{1}{2} f_{\text{Ca}} \left(\frac{j_{cG}^{\max}}{\Sigma_{\text{cone}}} \frac{u^{m_{cG}}}{K_{m_{cG}} + u^{m_{cG}}} \right)$$

which is a Hill equation expressing cGMP binding to the channels which gate the influx of calcium. The Hill exponent, m_{cG}, is a measure of the cooperativity of cGMP molecules needed at once to bind the gated channel.

3 Statement of the Homogenized Pointwise Diffusion of cGMP and Ca^{2+}.

3.1 How Homogenization Informs cGMP and Ca^{2+} Diffusion.

While the form of the diffusion laws (2.1, 2.2) are themselves relatively simple, they are set to a cone geometry which itself exhibits competing physical scales which should not be neglected in modeling the photoreceptor response. Though the chambers are thin and numerous, each one of their faces contains the biochemistry which drives the cascade. Similarly, the volumic diffusion of cGMP and Ca^{2+} is global throughout the cone photoreceptor. At the same time its diffusion within thin regions like the sliver cannot be neglected because this opens and closes gated channels.

The presence of several, relevant geometric scales is computationally expensive to model numerically. Finite element meshes must be sufficiently refined to capture the fine features, but this taxes memory usage and incurs time costs to assemble the spline mass and stiffness matrices as well as perform the time integration.

The program of homogenization first handles the multi-scale complexity of the domain at a modeling level before the numerics are implemented. The intuitive idea is that because certain features of the domain are quite small now already, it would not perturb the process to continue diminishing those small features to an asymptotic limit.

Where the nonhomogenized problem consists of a standard diffusion law set to a geometrically complex domain, homogenization recasts that geometric complexity into a novel diffusion process set to a simplified and single scale geometry. In this way, information originally encoded by geometry is now encoded in the equation. This reshuffling of information into the other type can preserve the overall model (see Table 5.1). Moreover, the

final product is less computationally expensive to implement numerically than the original (see Table 5.2). The limiting process leads to a simplified form of geometry with an alternative governing law whose equation's terms reflect the small scale geometrical features present before the limit.

3.2 The Formal Homogenous Diffusion Law for the 2nd Messenger cGMP and Ca^{2+} System: Weak Form

The formal homogenized limit for the cGMP and Ca^{2+} system is presented in its weak form below. The symbol χ_{cGMP} is 1 when the cGMP diffusion equation is intended. It is 0 when the Ca^{2+} diffusion equation is intended. The symbol $\chi_{Ca^{2+}}$ is defined similarly with respect to Ca^{2+} diffusion. w below is a placeholder symbol which is u in the case of cGMP and v in the case of Ca^{2+}.

The Formal Homogenized, Global System Limit

The Ca^{2+} and *cGMP* are taken to satisfy the formally obtained homogenized, diffusion and coupled system below. The processes at different domains are linked through the common test function:

$$
\begin{aligned}
0 = (1-\theta_0)\Bigg\{ & \int_{\Omega_{0,T}} \Big(-\varphi_t w + D_w \nabla_{\bar{x}} \varphi \nabla_{\bar{x}} w + \chi_{cGMP} \left(\beta_{\text{dark}} u - f(v)\right) \varphi \Big) dx dt - \int_{\Omega_0} \varphi(\cdot,0) w_0 dx \Bigg\}_{\text{Int}} \\
+ \nu\varepsilon_0 \Bigg\{ & \int_{D_{z_0,T}} \Big(-\varphi_t \bar{w} + D_w \nabla_{\bar{x}} \varphi \nabla_{\bar{x}} \bar{w} + \chi_{cGMP} \left[\left(\beta_{\text{dark}} \bar{u} - f(\bar{v})\right) + \frac{1}{\nu\varepsilon_0} \bar{u} f_1(\bar{v}) \right] \varphi \Big) d\bar{x} dt \\
& \qquad - - \int_{D_{z_0}} \varphi(\cdot,0) w_0 d\bar{x} \Bigg\}_{\text{Act}} \\
+ \frac{\sigma\varepsilon_0}{\sqrt{1+\eta^2 r^2}} \Bigg\{ & \int_{\partial\Omega_{S,T}} \Big(-\varphi_t \hat{w} + D_w \nabla_S \varphi \cdot \nabla_S \hat{w} + \frac{\sqrt{1+\eta^2 r^2}}{\sigma\varepsilon_0} \chi_{Ca} \left(g_1(\hat{v}) - g_2(\hat{u})\right) \varphi \Big) dS dt \\
& \qquad - \int_{\partial\Omega_S} \varphi(\cdot,0) w_0 dS \Bigg\}_{\text{Sliver}}
\end{aligned}
$$

Here

$$\int_{\partial\Omega_S} \nabla_S \varphi \cdot \nabla_S \hat{w} dS = \int_{\theta=-\omega_0}^{\omega_0} \int_{z=0}^{H} \left(\frac{1}{[\lambda(z)]^2 r^2} \varphi_\theta \hat{w}_\theta + \frac{1}{1+\eta^2 r^2} \varphi_z \hat{w}_z \right) \lambda(z) r \sqrt{1+\eta^2 r^2} d\theta dz$$

Note that $\theta_0 = (1+\nu)^{-1}$, $\left(1+\eta^2 r^2\right)^{-1/2} = \cos\alpha$, and that the principal part in the sliver is a Laplace-Beltrami driven diffusion up to this latter geometric scaling factor. ■

Remark.
The factor $\left(1+\eta^2 r^2\right)^{-1/2}$ has a geometric meaning and is equal to $\cos\alpha$ where α is the aperture angle for the cone. The value $\sigma\varepsilon_0/\sqrt{1+\eta^2 r^2}$ is in fact the projection of the $\sigma\varepsilon_0 e_\rho$ *oblique* attachment vector onto the cone surface's exterior normal. Accordingly, this factor is the perpendicular length of the sliver off the cone surface. This quantity emerged from the formal application of concentrating capacity rather than being presupposed.

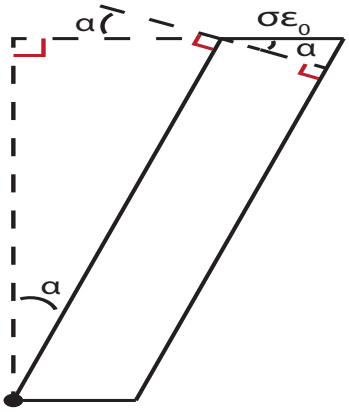

Figure 5.3: Concentrating capacity recovers the perpendicular width of the sliver.

3.3 The Formal Homogenous Diffusion Law for the 2nd Messenger cGMP and Ca^{2+} System: Pointwise Form

In turn there is a *formal* strong version of the homogenized limit which is reported here. Recall u will stand for $[cGMP]$ and v will stand for $\left[Ca^{2+}\right]$.

Limit in the Interior Volume: Test by a φ supported away from the activation site and cone boundary, it holds in the distributional sense

$$u_t - D_{\mathrm{cG}} \Delta_{\bar{x}} u = -\left(\beta_{\mathrm{dark}} u - f v \right) \tag{3.1}$$

$$v_t - D_{\mathrm{Ca}} \Delta_{\bar{x}} v = 0 \tag{3.2}$$

Limit at the Activation Site. For a fixed function defined on the two dimensional disc interior, regard it as a trace for some extension φ. In the weak formulation, test by $\zeta_A(z)\varphi$ where the latter is a bump function concentrating at the activation site. In the formal limit, we will recover a process independent of the choice of extension and depending only on the given trace. It holds distributionally that

$$\bar{u}_t - D_{\mathrm{cG}}\Delta_{\bar{x}}\bar{u} = -\left(\beta_{\mathrm{dark}}\bar{u} - f\bar{v}\right) - \frac{1}{\nu\varepsilon_0}\bar{u}f_1(\bar{v}) \tag{3.3}$$

$$\bar{v}_t - D_{\mathrm{Ca}}\Delta_{\bar{x}}\bar{v} = 0 \tag{3.4}$$

To show, observe that due to $\zeta_A\varphi$'s support, only interior and activation terms survive in the homogenized weak formulation. Because the interior terms only carry $\nabla_{\bar{x}}$ derivatives, even the interior terms vanish as the $\zeta_A(z)$ is concentrated to the activation disc.

Limit at the Sliver. As will be formally shown below, at the sliver there is the formal pointwise process

$$\hat{u}_t - D_{cG}\Delta_S\hat{u} = -\frac{(1-\theta_0)\sqrt{1+\eta^2r^2}}{\sigma\varepsilon_0}D_{cG}\nabla_{\bar{x}}u\cdot\vec{n} - \delta_{[z=z_0]}\frac{\nu\sqrt{1+\eta^2r^2}}{\sigma}D_{cG}\nabla_{\bar{x}}\bar{u}\cdot e_\rho \tag{3.5}$$

$$\begin{aligned}\hat{v}_t - D_{Ca}\Delta_S\hat{v} = &-\frac{\sqrt{1+\eta^2r^2}}{\sigma\varepsilon_0}\left(g_1\hat{v} - g_2\hat{u}\right) - \frac{(1-\theta_0)\sqrt{1+\eta^2r^2}}{\sigma\varepsilon_0}D_{Ca}\nabla_{\bar{x}}v\cdot\vec{n} \\ &- \delta_{[z=z_0]}\frac{\nu\sqrt{1+\eta^2r^2}}{\sigma}D_{Ca}\nabla_{\bar{x}}\bar{v}\cdot e_\rho\end{aligned} \tag{3.6}$$

To show (3.5),(3.6) take $\zeta_S\varphi$ where ζ_S concentrates to the bounding sliver surface and decays along the sliver's normal. Again, the φ as a trace on the sliver is meant to be in the sliver's interior. Once more, it's the gradient terms in the interior and activation that may additionally contribute to the formal sliver process. Other terms vanish as the domain's measure vanishes. For the gradient terms we will have a limit applied to

$$(1-\theta_0)\int_{\Omega_0} D_w\varphi\nabla_{\bar{x}}\zeta_S\nabla_{\bar{x}}w + \nu\varepsilon_0\int_{D_{z_0}} D_w\varphi\nabla_{\bar{x}}\zeta_S\nabla_{\bar{x}}\bar{w}$$

Because $\nabla_x \zeta_S \nabla_{\bar{x}} w = \nabla \zeta_S \nabla_{\bar{x}} w$ and distributionally the gradient of this bump function tends to the vector-valued normal surface measure, the first term becomes

$$\lim (1-\theta_0) \int_{\Omega_0} D_w \varphi \nabla_{\bar{x}} \zeta_S \nabla_{\bar{x}} w = (1-\theta_0) \int_{\partial \Omega_S} D_w \varphi \nabla_{\bar{x}} w \cdot \vec{n} dS$$

The second term is more delicate because the direction ζ_S decays is not contained in the domain of the integral. To compute we observe that $\nabla \zeta_S$ is directed along the inward normal rays originating from the sliver as we have taken ζ_S to be a bump function along the sliver's normal. The inward normal will be the direction of maximum decrease. Letting p_∂ be a point of origin for the inward ray normal at the boundary, its magnitude is found by

$$\left(1 - \frac{1}{\varepsilon} s\right) \chi_{[0,\varepsilon]}(s) = \zeta_S(p_\partial + s\vec{n}) \Rightarrow -\frac{1}{\varepsilon} \chi_{[0,\varepsilon]}(s) = \nabla \zeta_S(p_\partial + s\vec{n}) \cdot \vec{n} = -\left|\nabla \zeta_S(p_\partial + s\vec{n})\right|$$

Observe that $-|\nabla \zeta_S|$ is the coordinate of the gradient on the inward normal $\vec{n}$. If p_∂ is that point on the conical, sliver boundary parameterized by cylindrical coordinates (θ, z), then

$$p_\partial + s\vec{n} = \begin{pmatrix} \lambda(z) r \cos\theta \\ \lambda(z) r \sin\theta \\ z \end{pmatrix} + s \begin{pmatrix} -\cos\theta / \sqrt{1+\eta^2 r^2} \\ -\sin\theta / \sqrt{1+\eta^2 r^2} \\ \eta r / \sqrt{1+\eta^2 r^2} \end{pmatrix}$$

If given a point $p \in D_{z_0}$, we may find $p_\partial(p)$ as so: parameterize the disc by polar coordinates at the origin. Observe this θ coincides with the angle used in the parameterization at the sliver. Indeed, they are the rotation angle about the z-axis. It follows that p's θ coordinate defines its corresponding normal ray $\vec{n}$ since motion along that ray preserves θ. We need only follow the ray till the cone's boundary is crossed. This will occur when motion along the outward normal from p hits the boundary:

$$\rho + \frac{s}{\sqrt{1+\eta^2 r^2}} = \lambda \left[z_0 - s \frac{\eta r}{\sqrt{1+\eta^2 r^2}} \right] r = \eta \left(z_0 - s \frac{\eta r}{\sqrt{1+\eta^2 r^2}} \right) r + r$$

In particular, the value $z = z_0 - s\eta r/\sqrt{1+\eta^2 r^2}$ is the height value of p_∂. Eliminating s, we obtain p_∂ lies at the z-height

$$z = \frac{z_0 - \eta r^2 + \rho\eta r}{1+\eta^2 r^2}$$

Remember because the disc was parameterized with polar coordiantes $\rho \in \left[0, \lambda(z_0)r\right]$. The θ was already known from p. Together these determine the location of p_∂ through the relation

$$p_\partial = \begin{pmatrix} \lambda[z(z_0,\rho)]r\cos\theta \\ \lambda[z(z_0,\rho)]r\sin\theta \\ z(z_0,\rho) \end{pmatrix}$$

From this expression, we may evaluate the s associated to $p \in D_{z_0}$. Its value is used to compute $-\frac{1}{\varepsilon}\chi_{[0,\varepsilon]}(s) = -\left|\nabla\zeta_S\left(p_\partial + s\vec{n}\right)\right|$. Knowing $p - p_\partial = s\vec{n}$, we may look to any component to solve for s. We arbitrarily choose the z-component:

$$z_0 - \frac{z_0 - \eta r^2 + \rho\eta r}{1+\eta^2 r^2} = s\frac{\eta r}{\sqrt{1+\eta^2 r^2}} \Rightarrow s = \frac{\eta r z_0 + r - \rho}{\sqrt{1+\eta^2 r^2}}$$

Hereafter, we will write $\vec{n}_i$ for the interior normal as soon we will revert back to the usual exterior normal. Altogether we have

$$\begin{aligned} \nu\varepsilon_0 \int_{D_{z_0}} D_w\varphi\nabla_{\bar{x}}\zeta_S\nabla_{\bar{x}}\bar{w} &= \nu\varepsilon_0 \int_{\theta=-\pi}^{\pi}\int_{\rho=0}^{\lambda(z_0)r} D_w\varphi(\theta,\rho)\nabla\zeta_S(\theta,\rho)\nabla_{\bar{x}}\bar{w}(\theta,\rho)\rho d\rho d\theta \\ &= \nu\varepsilon_0 \int_{\theta=-\omega_0}^{\omega_0}\int_{\rho=0}^{\lambda(z_0)r} D_w\varphi(\theta,\rho)\nabla\zeta_S\Big(p_\partial(\theta,\rho) + s\vec{n}_i(\theta,\rho)\Big)\nabla_{\bar{x}}\bar{w}(\theta,\rho)\rho d\rho d\theta \\ &= \nu\varepsilon_0 \int_{\theta=-\omega_0}^{\omega_0}\int_{\rho=0}^{\lambda(z_0)r} D_w\varphi(\theta,\rho)\left(-\frac{1}{\varepsilon}\chi_{[0,\varepsilon]}\big(s(z_0,\rho)\big)\vec{n}_i\right)\nabla_{\bar{x}}\bar{w}(\theta,\rho)\rho d\rho d\theta \end{aligned}$$

Using the expression for s, we have

$$0 \le s = \frac{\eta r z_0 + r - \rho}{\sqrt{1+\eta^2 r^2}} \le \varepsilon \Leftrightarrow \eta r z_0 + r - \varepsilon\sqrt{1+\eta^2 r^2} \le \rho \le \eta r z_0 + r$$

Substitute this into the integral limits above after recognizing the non ε term is $\lambda(z_0)r$ and obtain

$$\nu\varepsilon_0\int_{D_{z_0}} D_w\varphi\nabla_{\bar{x}}\zeta_S\nabla_{\bar{x}}\bar{w} = \nu\varepsilon_0\int_{\theta=-\omega_0}^{\omega_0}\int_{\rho=\lambda(z_0)r-\varepsilon\sqrt{1+\eta^2r^2}}^{\lambda(z_0)r} D_w\varphi(\theta,\rho)\left(-\frac{1}{\varepsilon}\right)\nabla_{\bar{x}}\bar{w}(\theta,\rho)\cdot\vec{n}_i\rho d\rho d\theta$$

We now will have

$$\begin{aligned}&\lim_{\varepsilon\to 0}\nu\varepsilon_0\int_{D_{z_0}} D_w\varphi\nabla_{\bar{x}}\zeta_S\nabla_{\bar{x}}\bar{w}\\ &\qquad = \nu\varepsilon_0\sqrt{1+\eta^2r^2}\int_{\theta=-\omega_0}^{\omega_0} D_w\varphi(\theta,\lambda(z_0)r)\,(-1)\,\nabla_{\bar{x}}\bar{w}(\theta,\lambda(z_0)r)\cdot\vec{n}_i\lambda(z_0)rd\theta\end{aligned}$$

Note that $\vec{n}_i$ is the inward *cone* normal and not yet the disc's normal. Next get

$$(-1)\,\nabla_{\bar{x}}\bar{w}(\theta,\lambda(z_0)r)\cdot\vec{n}_i = \nabla_{\bar{x}}\bar{w}(\theta,\lambda(z_0)r)\cdot\begin{pmatrix}\cos\theta/\sqrt{1+\eta^2r^2}\\ \sin\theta/\sqrt{1+\eta^2r^2}\\ -\eta r/\sqrt{1+\eta^2r^2}\end{pmatrix} = \nabla_{\bar{x}}\bar{w}(\theta,\lambda(z_0)r)\cdot e_\rho/\sqrt{1+\eta^2r^2}$$

We now have formally

$$\begin{aligned}&lim_{\varepsilon\to 0}\nu\varepsilon_0\int_{D_{z_0}} D_w\varphi\nabla_{\bar{x}}\zeta_S\nabla_{\bar{x}}\bar{w} = \nu\varepsilon_0\int_{-\omega_0}^{\omega_0} D_w\varphi(\theta,\lambda(z_0)r)\nabla_{\bar{x}}\bar{w}(\theta,\lambda(z_0)r)\cdot e_\rho\lambda(z_0)rd\theta\\ &\qquad = \nu\varepsilon_0\int_{\partial D_{z_0}\cap S} D_w\varphi\nabla_{\bar{x}}\bar{w}\cdot e_\rho ds\end{aligned}$$

4 Validating the Homogenized Model Through Numerical Experiments and the Model's Advantages.

4.1 An Overview of the Finite Element Code.

Both the non-homogenized and homogenized models have been implemented as finite element code in Matlab. Maple was also used in the local element assembly to produce a master element coordinate representation of the PDE terms at each element. The non-homogenized and homogenized codes both have been included with this thesis and may be run in Matlab. For both models, the software divides into two parts.

The first part numerically models the activation process on the special disc. There are several variations of the code that account for the stochastic shut-off and diffusion of R^*, the activated GPCR. The simplest model takes the site of activation R^* as a dirac mass source term in a diffusion equation for G^*, activated G-protein. The G-protein and available effector generate source terms for diffusion of E^*, the activated effector, with its own parameter weight again reflecting the G-protein's catalytic activity and shut-off [120]. This concludes the processes on the special disc, and the E^* is now used in the boundary data terms of the volumic diffusion process for cGMP and Ca^{2+}. Each equation is integrated through a standard Galerkin, spatial discretization over a horizontal disc which is the cross section of the cone at the z-height where photon isomerization occurs. The user specifies the location of photon isomerization by giving its z-height and its horizontal location in polar coordinates. The horizontal location becomes the dirac mass site for R^*. The z-height specifies where the isomerization occurs along the length of the cone.

The R^* dirac mass generates G-protein, and its associated catalytic activity depends on time in oder to encode shut-off. This acitivity can be made stochastic by the user – by setting an option in the code – to express the random variability of phosphorylation and Arrestin binding. In the case of rods, a continuous time Markov chain was used to generate the probabilities of being in any phosphorylated or Arrestin state [116]. In the simulations

presented here, cones have been modeled with a single step direct to Arrestin binding. Consequently the probability of Rhodopsin staying active goes like an exponential decay. The code is sufficiently general to handle more complex stochastic events, but the modeling choice in the figures was to take a single step.

The time integration is handled through an implicit theta method. Both the non-homogenized and homogenized models use essentially the same numerical code to model activation. This holds because the small scale structures are along the height of the cone while activation occurs within a cross section.

The volumic diffusion is a system for the cGMP and Ca^{2+} concentrations coupled through their Neumann data. The non-homogenized and homogenized codes are critically different here. In the latter, the domain is a simple, truncated cone while in the nonhomogenized model it is a stack of conical chambers connected through a sliver. These meshes have been built in Matlab. See Figure 5.2 for reference. Note simulations were done with 500 chambers and a sliver scaled accordingly. In the homogenized model, the number of chambers is encoded through the parameters ν and ε_0 entered by the user.

Again a Galerkin, spatial discretization is used but now over the volume elements of the respective cone domain. The non-homogenized and homogenized models are distinct at this point for two reasons: One is that their three dimensional geometries are now different. The second is that their equation terms over the volume now also differ. Observe also that the couple between these two concentrations is in fact nonlinear owing to the presence of Michaelis-Menten and Hill laws at the channels and the synthesis of cGMP by Cyclase. This nonlinear system is solved through an implicit theta-method iteration which approximates the true solution through a numerical fixed point scheme at each consecutive time step. The *a posteriori* and relative error parameters, which the code uses to decide if it has found a numerical fixed point, are preset by the user.

4.2 Observed Numerical Convergence Rates Between the Models.

Simulations with both codes are compared to show numerical evidence that the homogenized model approximates the standard diffusion model as the spacing between chambers diminishes, equivalently, as the number of chambers in the cell geometry grows. These simulations were performed with the best known model parameters as of May 2017. The homogenized model is shown with a solid blue line. The nonhomogenized model is shown with a dashed red line. The single photon response is the left panel, while the ten phton response is the right panel. Simulations have been performed by changing the geometric number of chambers in the non-homogenized model and changing the parameter ε_0 which encodes the number of chambers in the homogenized model. Single photon and ten photon simulations were performed by changing the number of activation sites.

Single photon numerical experiments dropped a photon at $.4 * H$ of the height (H) of the cone in the center of the disc. Ten photon simulations dropped the photons at the center of discs at heights $.4 * H$ to $.58 * H$ in increments of $.02 * H$.

For convenience the errors are reported together in Table 5.1.

4.3 Benefits of a Homogenized Model

As Table 5.1 and the above figures show, the homogenized model better approximates the nonhomogenized one as the number of chambers increases. Further, the homogenized model requires far less time and computer memory. Table 5.2 gives the time it took a desktop computer to build just the mass and stiffness matrix in the volume for the finite element, nonhomogenized model. Recall that building these matrices is a necessary first

Relative Error	100ch	200ch	300ch	400ch	500ch
Single	8.38%	7.46%	6.67%	6.01%	5.60%
Ten	28.32%	17.13%	12.56%	9.89%	8.33%

Table 5.1: Numerical Errors Between Homogenized and Nonhomogenized Models.

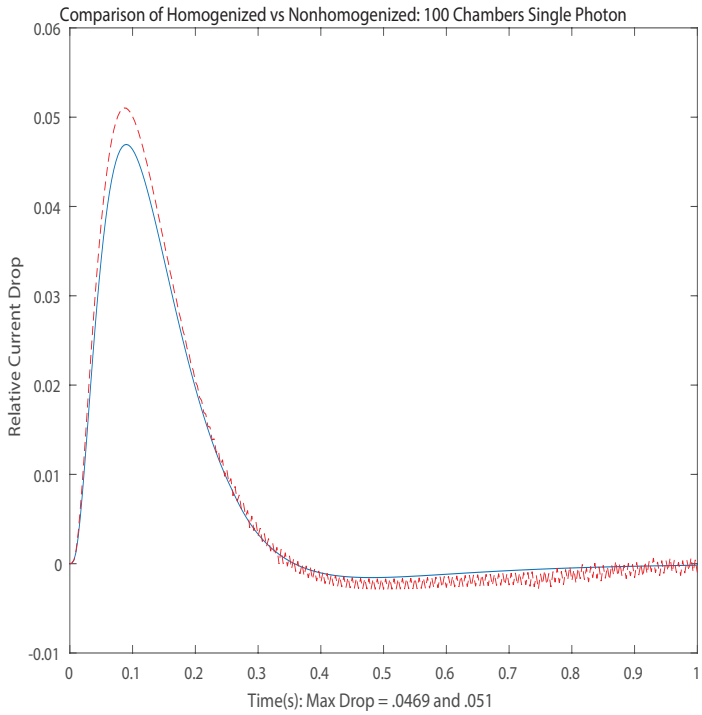

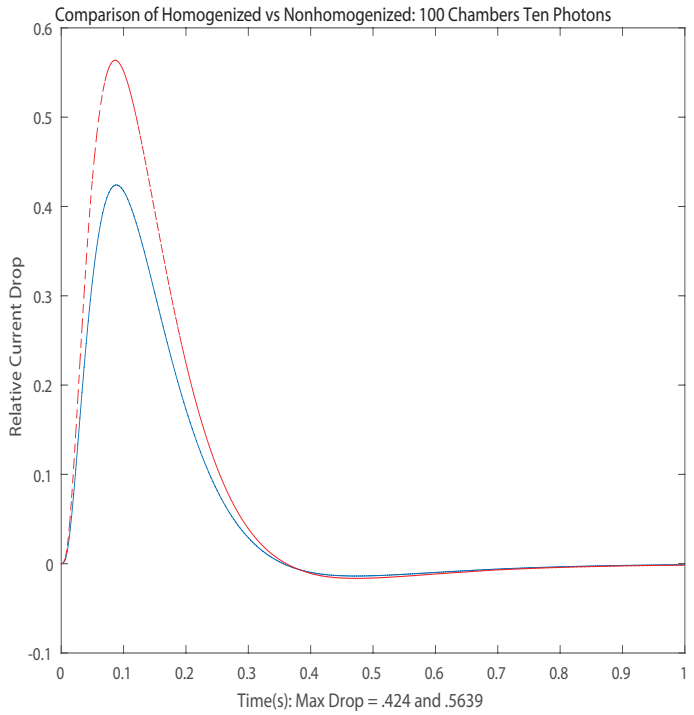

Figure 5.4: Comparison of homogenized and nonhomogenized models: 100 chambers. Relative errors of single and ten photons: 8.38% and 28.32%

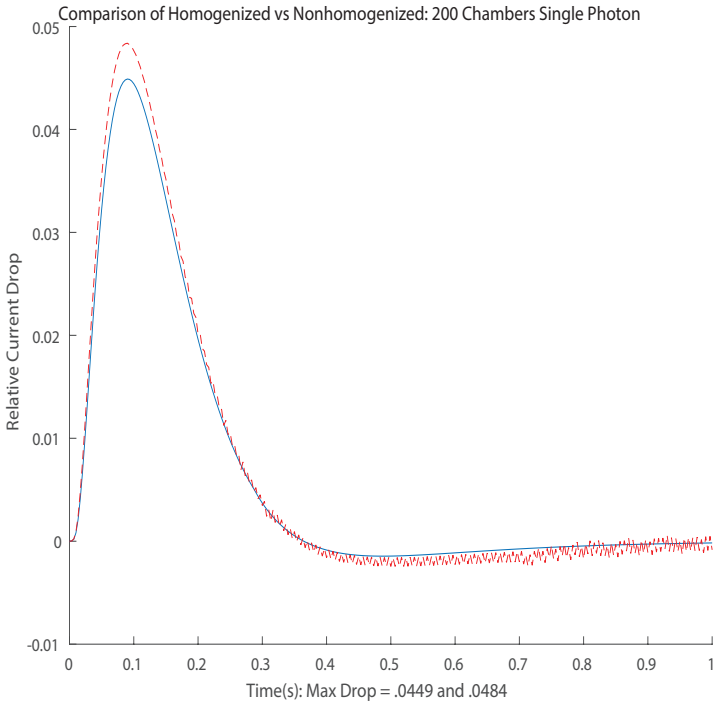

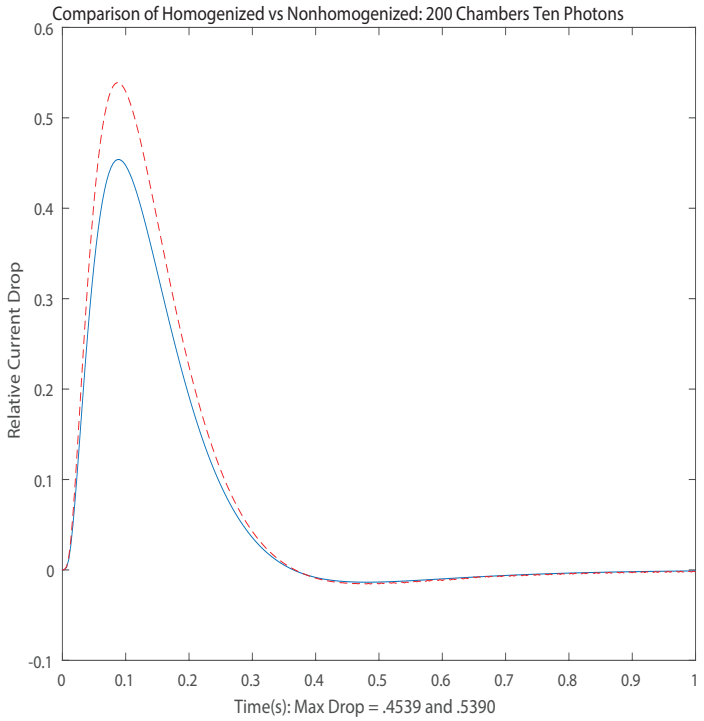

Figure 5.5: Comparison of homogenized and nonhomogenized models: 200 chambers. Relative errors of single and ten photons: 7.46% and 17.13%

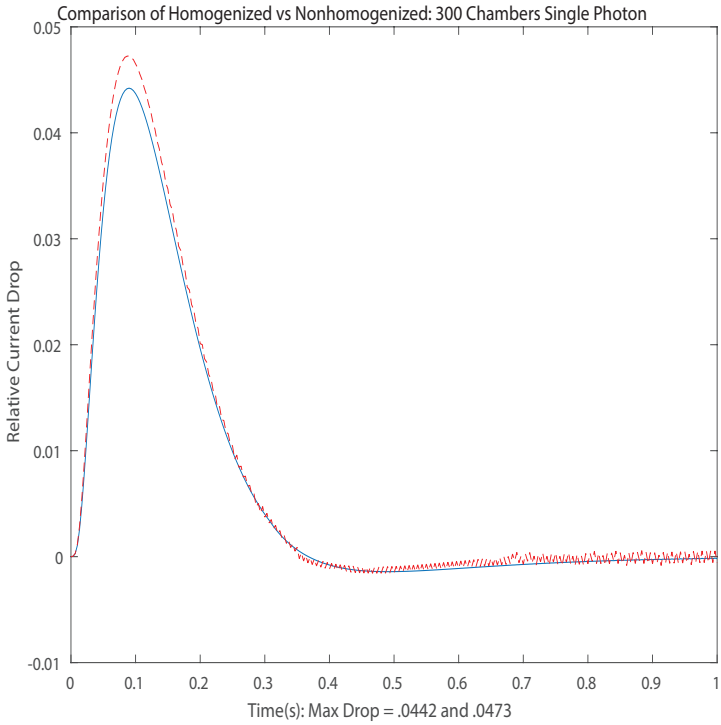

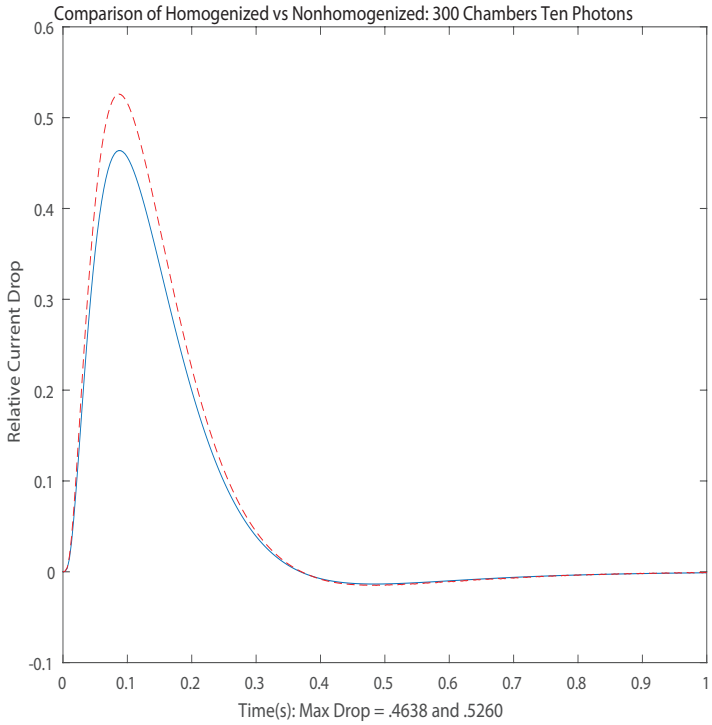

Figure 5.6: Comparison of homogenized and nonhomogenized models: 300 chambers. Relative errors of single and ten photons: 6.67% and 12.56%

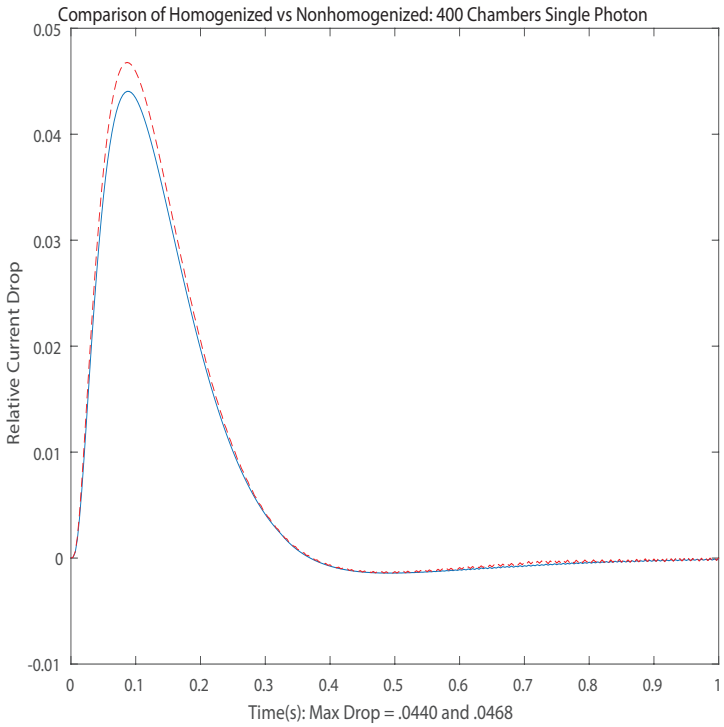

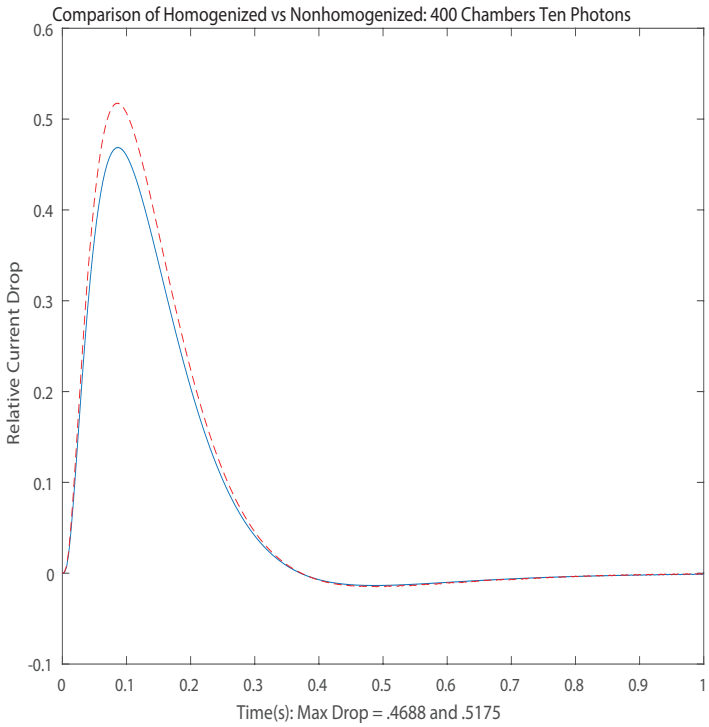

Figure 5.7: Comparison of homogenized and nonhomogenized models: 400 chambers. Relative errors of single and ten photons: 6.01% and 9.89%

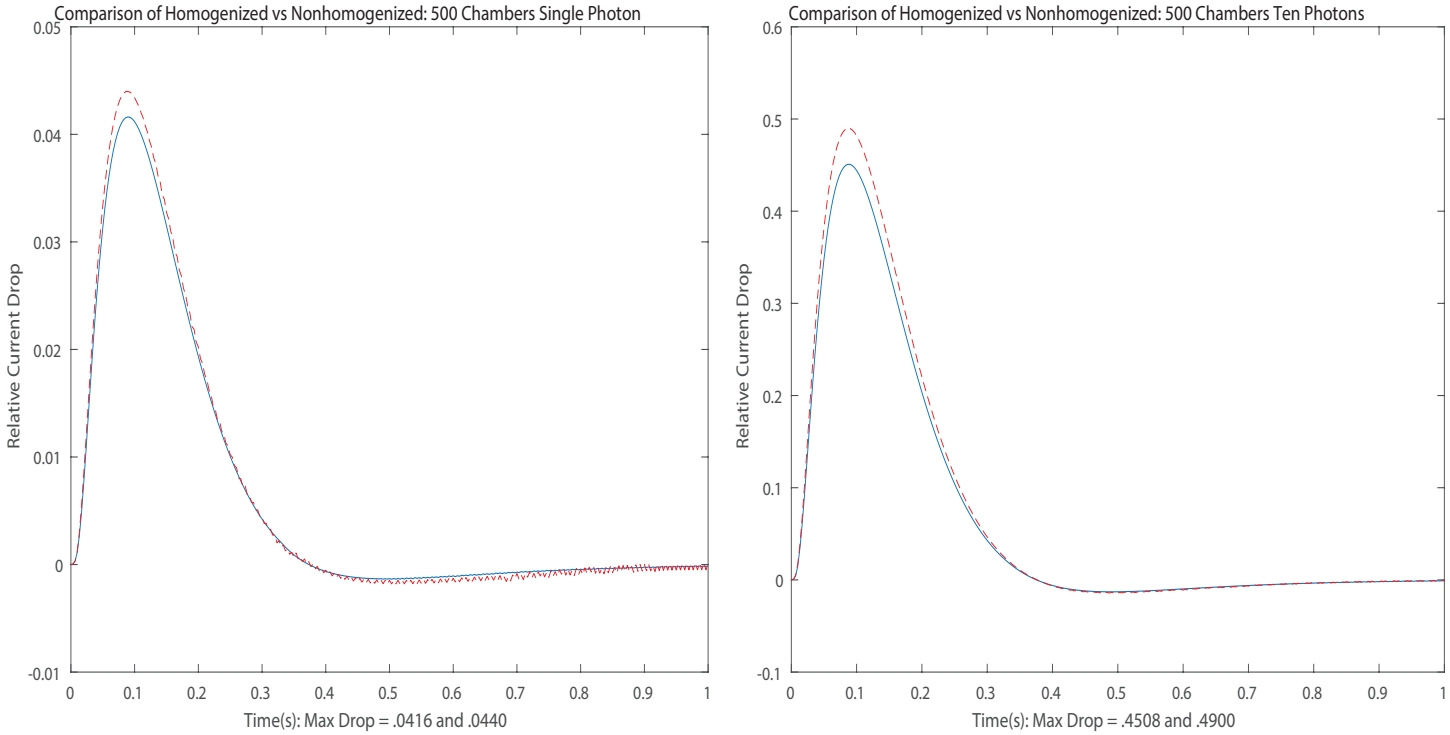

Figure 5.8: Comparison of homogenized and nonhomogenized models: 500 chambers. Relative errors of single and ten photons: 5.60% and 8.33%

Assembly Time	100ch	200ch	300ch	400ch	500ch
Nonhom	17.4 hr	56.8 hr	106.1 hr	171.9 hr	217.8 hr
Hom	10 sec	16 sec	17 sec	22 sec	26 sec

Table 5.2: Times to assemble volume mass and stiffness matrices on the prototype bass model geometry with sliver on half the rim's circumference. This assembly was performed by a computer with Intel(R) Core(TM) i5-4200U CPU @ 1.60 GHz and 2.30GHz with 4.00GB of ram.

step in running the model.

The nonhomogenized model's time integration was performed on Vanderbilt's supercomputer cluster ACCRE. ACCRE routinely reported that in the course of factoring the mass and stifness matrices and performing time integration, it used 80-120 gigabytes of virtual memory. Time integration on Accre could last anywhere from a couple hours to multiple days. Desktop computers with Intel(R) Core(TM) i7-6700 CPU @ 3.40 GHz 3.41 GHz and 16.0 GB Ram routinely returned a ran out of memory error when factoring the mass and stiffness matrix when chambers were given a 6 layer spatial discretization within

each chamber. Even at times when the desktop computers successfully obtained the matrix factorization, in ten photon simulations of 400 and 500 chambers and a 6 layer discretization, desktop computers would often run out of memory at the first or second step of time integration.

By contrast all homogenized models ran and finished in under ten minutes on desktop computers.

5 Biochemical and Geometrical Parameters for Cone Species.

We next report the parameters used in the non-homogenized and homogenized cone models. Compared to rods, the literature quantifying cone biochemistry is relatively small. We report the best numbers found to date. See Table 5.3-5.5. It should be noted that the table does not present parameters for a single model species, but gives the values for whatever species a parameter may have been found or computed. Some parameters have even been computed from measurements drawn from different species. In the absence of any information, the value for rods listed in [117] was substituted instead.

5.1 The Basis for Parameter Values

Any necessary comments on how parameter values reported in the table were derived are explained in detail here.

- $\alpha_{\max}$

  The concentration of guanylate cyclase in carp cones and carp rods respectively has been measured by Kawamura in [121] to be $72\mu M$ and $4.2\mu M$ respectively. Their ratio then scales the mouse rod value of $\alpha_{\max} = 76.5\mu M s^{-1}$ given in [117].

- $\alpha_{\max}/\alpha_{\min}$

  The rod value reported in [117] is taken.

- β_{dark}

  The synthesis rate of cGMP in the dark is proportional with the dark concentration of cGMP through the proportionality constant β_{dark}. This relationship is used both in [117] and [122]. In [117], the authors report the value of $.25 \pm .06 s^{-1}$. This estimate is based on a combination of measurement and empirifical fit and uses a $[cGMP]_{\text{dark}}$ value for bass which is more than 10 times larger than that measured elsewhere for Carp. In [123], the authors report that the *relative* PDE dark activity measured in cone membranes ($2.5 \pm 2.2\%$ of maximum activity) was similar to that of rod ($1.1 \pm 1.0\%$). In that paper, the maximum PDE activity was measured as $17.8 cGMP/R^*/s$. If $[cGMP]_{\text{dark}} = 25 \mu M$ as reported in [122] for bass and the concentration of visual protein is $3mM$ as measured for carp in [121], this would lead to an estimate in units s^{-1} of

  $$\beta_{\text{dark}} = 17.8 * (2.5\%) * (3 * 10^3)/25 = 53.4$$

  The value $\beta_{\text{dark}} = 66.9 s^{-1}$ was chosen and used in models because it expressed equilibrium balance between PDE hydrolysis and cyclase synthesis for the given choice of other model parameters. Indeed from text equation (11) and (13) in [117], we have the relation

  $$\alpha_{\text{min}} + \frac{\alpha_{\text{max}} - \alpha_{\text{min}}}{1 + \left([Ca^{2+}]_{\text{dark}}/K_{cyc}\right)^{m_{\text{cyc}}}} = \beta_{\text{dark}} [cGMP]_{\text{dark}}$$

  Upon substitution with model values, this becomes in the appropriate units:

  $$1311/13.9 + \frac{1311 - 1311/13.9}{1 + (.4/.1)^{2.45}} = \beta_{\text{dark}} * 2$$

- B_{cG}

  In [121], the total quantities of PDE in carp cone and rods were reported as similar, so that their ratio is taken as 1. The buffering power for cGMP is then taken as 1

times the mouse rod value $B_{cG} = 1$ reported in [117].

- B_{Ca}

  In [122] at text equation (1.12), a parameter value $\Omega = .15$ is reported where the influx of calcium is $J_{\text{in}}(t) = f_{\text{Ca}} \frac{\Omega}{zF} I_m(t)$ where $f_{\text{Ca}} = .33$ is the fraction of current I_m carried by calcium, $z = 2$ is the valence of Ca^{2+}, and F is Faraday's constant. By direct comparison with (12) of [117], it follows

  $$\frac{.5 * f_{\text{Ca}}}{B_{\text{Ca}} * F} = f_{\text{Ca}} \frac{\Omega}{zF}$$

  from whence the reciprocal relationship $B_{\text{Ca}} = \Omega^{-1}$ holds. Note that [115] believes that the calcium buffer mechanism is more complicated in cones, and should not be taken as a single number.

- c_{TE}

  c_{TE} is the ratio ν_{RE}/ν_{RG}. The mouse rod value, 1, in [117] is taken.

- $[cGMP]_{\text{dark}}$

  [115], as reported in Table 1, uses parameter fitting of the dark current to estimate the dark concentration of cGMP. This led to an estimate of 27.9 ± 14.2. In [124], the value is instead estimated as $2\mu M$ and is the value taken in the presented in simulations.

- $D_{cG} - D_R$

  Diffusion coefficients are taken as they are for rods per [117]

- η

  η is the asymptotic conversion ratio to pass from the volumic density defined in a chamber and the surface area densities defined on discal faces:

  $$\eta = \frac{\pi * r_z^2 * \nu * \varepsilon_0}{2 * \pi * r_z^2} = .5 * \nu * \varepsilon_0$$

- f_{Ca}

  [125] has found the fraction of current carried by calcium in cones to be larger than the .06 value reported for rods [117].

- j_{dark}

  In [126], the striped bass measurement was obtained through measuring current in 18 different striped bass cones.

- j_{ex}^{sat}

  In [126], the striped bass measurement was obtained through measuring current in 18 different striped bass cones.

- k_{cat}/K_M

  [122] reports for striped bass that the PDE hydrolysis rate of cGMP is given by

$$-\frac{k_{\text{cat}}}{K_M} N^* [cGMP]$$

  where N^* is the number of active PDE molecules and K_M is the Michaelis-Menten constant for cGMP. In this context k_{cat}/K_M was reported to be $(5*10^3 \text{molecules} s^1)/(10\mu M)$. This value is within the range reported in [117] for mouse rod.

- $k_{\sigma,\text{hyd}}$

  This quantity may be computed from the expression (23) in [117]:

$$k_{\sigma,\text{hyd}} = \frac{\eta\beta_{\text{dark}}}{[PDE]_\sigma} = \frac{(.0075\mu m)(66.9 s^{-1})}{1000 \text{ PDE molecules per } \mu m^2} = 5.02*10^{-4}\mu m^3 s^{-1}$$

  In simulations where $[PDE]_\sigma = 5\mu m^{-2}$ was taken, this parameter value was adjusted accordingly.

- $k_{\sigma,\text{hyd}}^*$

This quantity may be computed from the expression just after (24) in [117]:

$$k^*_{\sigma,\text{hyd}} = \frac{k_{\text{cat}}/K_M}{N_{\text{Av}}B_{\text{cG}}} = \frac{\left(500\mu M^{-1}s^{-1}\right)}{6.02*10^{23}/mol} = .83\mu m^3 s^{-1}$$

- k_R

  [117] gives the highest measured rate constant for inactivation of Rhodopsin in mouse rod as $12.5s^{-1}$. This value was used in the single step Arrestin shut-off in simulations presented here. Separately, [123] approximates rhodpsin quantities by an exponential decay and reports that the inverse of the exponential decay, time constant of R^* in the presence of phosphorylation (ATP+) is $1.0s$. The authors give experimental evidence here that phosphorylation plays a role in cones because in experiments without phosphorylation (ATP-), they measure of this time constant as 2.9s. The decay rate is taken as the inverse of the lifetime: $1s^{-1}$. Note that this value is less than rate constant of 12.5 reported for rods in [117].

- K_{cyc}

  [126] draws from the experimental data of [124] and the calcium dependence of [127] to produce this value.

- $K_{cG} - K_{ex}$

  The mouse rod values reported in [117] are taken.

- ν

  From the measurements of ε and $\nu_\varepsilon = \nu * \nu_\varepsilon$, it follows that this value is taken as unity.

- ν_{RG}

  Computed from c_{TE} and ν_{RE}.

- n

  Computed from H, ν and ε through the relation

$$n = \frac{H}{\nu\varepsilon + \varepsilon} = 15\mu m/(2 * .015\mu m) = 500$$

- m_{cyc}

  The rod value in [117] is reported.

- m_{cG}

  [126] draws from the experimental data of [124] and the calcium dependence of [127] to produce this value.

- $[PDE]_\sigma$

  The highest reported mouse rod value of [117] was taken in simulations. Literature does give quantities that could compute this density except they lead to numbers much less than those for rods. [123] reports that the PDE dark activity of cones is $2.5 \pm 2.2\%$ of the maximum PDE activity. [121] reports that the total concentration of PDE in the outersegment is $11\mu M$ in frog. By approximating the volume of the cone as a cylinder of same height and radius the average radius of the cone, this leads to the total number of active PDE molecules in the cone OS being approximately

$$(2.5\%)\,(11\mu M)\left[\pi * (2\mu m)^2 * (15\mu m) * 6.02 * 10^{23}/\text{mol}\right] = 31193.96$$

  There are 500 chambers with an average radius of approximately $2\mu m$, each of which has 2 faces. This would lead to a surface density of $[PDE]_\sigma = 31193.96/\left[500 * 2 * \pi * (2\mu m)^2\right] = 2.49\mu m^{-2}$. [122] reports that the total number of active PDE molecules in the dark is 60 and that the total number of PDE molecules is $3 * 10^6$. If 60 is regarded as too low, one could repeat the argument done

for [121] and obtain an estimate

$$5.96\mu m^{-2} = \frac{(2.5\%)\,(3 * 10^6 \text{ PDE molecules })}{500 * 2 * \pi * (2\mu m)^2}$$

A value of $5\mu m^{-2}$ was used in some simulations not shown to explore the effects of these values compared to the taken value of $1000\mu m^{-2}$. While the peak drops lowered and the time to peak grew, these differences were modest. More importantly, the same current response behaviors emerged in numerical experiments regardless of whether the density was 5 or 1000.

6 Numerical Transduction Experiments.

In this section, several virtual experiments are reported to explore cone photoreceptor system behavior. Unless otherwise stated, all cone geometries place the channels at the sliver only.

In the first set of panels the mouse rod parameters of [117] are used as a base model. Then first the geometry is changed to a striped bass cone geometry while the mouse rod biochemistry is fixed. Second the biochemistry is changed to the model cone biochemistry, in Tables 5.3-5.5, while the mouse rod geometry is fixed. The second set of panels does the same except uses the model cone as the base.

In [125], it is observed that the fraction of current carried by calcium is greater in cones than rods: .33 vs .06. The next virtual experiment compares differences brought about by this difference in calcium current. The virtual experiment after it compares the effect of fixing the biochemical parameters as in Tables 5.3-5.5 while varying the geometry dimensions to be those of Human, Salamander and Striped Bass.

Finally two virtual experiments are presented that highlight differences caused by the possible localization of the cGMP-gated channels either at the sliver only or instead throughout all the folds and sliver of the outersegment.

It would be desireable to use biochemical parameters specific to each species. However, at present the literature did not have a complete set of biochemical parameters for any species. For the aforementioned reasons, the parameters in Table 5.3 - 5.5 cannot be regarded as reflecting a physical cone pertaining to a single real species. Similarly the numerical experiments shown may be superseded in time as more parameters become available or are improved.

Table 5.3: Parameters

Symbol	Units	Definition	Species	Value	Reference
$\alpha_{\max}$	$\mu M s^{-1}$	Maximum rate of cGMP synthesis at low Ca^{2+} concentration	Carp-Mouse	1311	[117],[121]
$\alpha_{\max}/\alpha_{\min}$	-	Suppresion ratio of α from high to low Ca^{2+} concentration	Carp-Mouse	13.9	[117]
β_{dark}	s^{-1}	Rate of cGMP hydrolysis by dark activated PDE		$66.9, 53.4$	Computed
	s^{-1}		Striped Bass	.26; .51	[115], [126], [122]
	s^{-1}		Carp	$\cong$ rod	[123]
B_{cG}	-	Buffering power of cytoplasm for cGMP		1	[115], [122], [126]
B_{Ca}	-	Buffering power of cytoplasm for Ca^{2+}	Striped Bass	6.67	[122]
c_{TE}	-	Coupling coefficient from G^* to E^*		1	[117]
$[\text{cGMP}]_{\text{dark}}$	μM	Concentration of cGMP in the dark	Carp	2	[124]
			Striped Bass	27.9 ± 14.2	[115]
$\left[Ca^{2+}\right]_{\text{dark}}$	μM	Concentration of Ca^{2+} in the dark	Striped Bass	.4	[115], [128]
			Carp	.41	[129]
r_{base}	μm	Radius of COS base	Striped Bass	$3.08 \pm .31$	[130]
			Tiger Salamander	2.5; 2	[130], [131]
			Human	1.5	[130]
			Turtle	1.25	[131]
			Primate	1.5	[131]
r_{tip}	μm	Radius of COS tip	Striped Bass	$1.2, 1.15 \pm .15$	[130], [126]
			Tiger Salamander	1.1; 1.25	[130], [131]
			Human	.75	[130]
			Turtle	.5	[131]
			Primate	.5	[131]
ω_0	-	Open margin angle for sliver	Striped Bass	π	[130]
			Frog	π	[128]
D_{cG}	$\mu m^2 s^{-1}$	Diffusion coefficient for cGMP	Mouse	120	[117]
D_{Ca}	$\mu m^2 s^{-1}$	Diffusion coefficient for Ca^{2+}	Mouse	15	[117]
D_E	$\mu m^2 s^{-1}$	Diffusion coefficient for activated PDE	Mouse	1.2	[117]
D_T	$\mu m^2 s^{-1}$	Diffusion coefficient for activated G-protein	Mouse	2.2	[117]
D_R	$\mu m^2 s^{-1}$	Diffusion coefficient for activated Rh	Mouse	1.5	[117]
ε	nm	disc thickness	Striped Bass	15	[130]
η	nm	Volume to surface ratio	Striped Bass	7.5	[117]
$\mathscr{F}$	C/mol	Faraday's Constant		96 500	[117]
f_{Ca}	-	Fraction of current carried by Ca^{2+}	Striped Bass	$.33 \pm .08$	[125],[126]

Table 5.4: Parameters Cont...

Symbol	Units	Definition	Species	Value	Reference
H	μm	Length of COS	Striped Bass	15.2 ± 1.46	[130],[126]
			Tiger Salamander	8	[131]
			Mouse	20	[131]
			Turtle	15	[131]
			Primate	13	[131]
			Human	7	[130]
j_{dark}	pA	Dark current	Striped Bass	27.3 ± 10.5	[126], [115],[122]
			Tiger Salamander	50	[131]
			Primate	40	[131]
$j_{cG}^{\max}$	pA	Maximum cGMP gated channel current (when saturate by cGMP)		2500	[126],[132]
j_{ex}^{sat}	pA	Saturated exchanger current	Striped Bass	4.87 ± 1.88	[126]
k_{cat}/K_m	$\mu M^{-1}s^{-1}$	Hydrolytic efficiency of activated PDE dimer	Striped Bass	500	[122], [117]
$k_{\sigma,\text{hyd}}$	$\mu m^3 s^{-1}$	Surface hydrolysis rate of cGMP by dark-activated PDE		$5.02 * 10^{-4}$	[122], [117]
$k^*_{\sigma,\text{hyd}}$	$\mu m^3 s^{-1}$	Surface hydrolysis rate of cGMP by light-activated PDE	Carp	.83	[133],[126], [117]
k_E	s^{-1}	Rate constant for inactivation of PDE	Striped Bass	18.5	[122]
k_R	s^{-1}	Rate constant for inactivation of VP	Mouse	12.5	[117]
			Carp	1	[134], [135], [123]
K_{cyc}	nM	Half-saturation $\left[\text{Ca}^{2+}\right]$ for GC activity	Striped Bass	100	[126]
K_{cG}	μm	[cGMP] for half-maximum cGMP-gated channel opening	Mouse	20	[117]
K_{ex}	μM	$\left[\text{Ca}^{2+}\right]$ for half-maximum exchanger channel opening	Mouse	1.6	[117]
ν	-	Ratio between interdiscal space and disk thickness		1	Computed
ν_ε	nm	Interdiscal space	Striped Bass	15	[130]
ν_{RE}	s^{-1}	Rate of PDE formation per fully activated Rh	Striped Bass	125	[122]
			Carp	30,42	[121],[133]
ν_{RG}	s^{-1}	Rate of Transducin formation per fully activated Rh	Striped Bass	125	Computed
			Carp	30,33	[121],[134], [133]
n	-	Number of disks		500	Computed
N_{Av}	mol^{-1}	Avogadro number		$6.02 * 10^{23}$	[117]

Table 5.5: Parameters Cont...

Symbol	Units	Definition	Species	Value	Reference
m_{cyc}	-	Hill coefficient for GC effect	Mouse	2.45	[117]
			Striped Bass	2	[126], [124], [127]
m_{cG}	-	Hill coefficient for cGMP-gated channel	Striped Bass	2.5	[126], [136], [132]
$[\text{PDE}]_{\sigma}$	μm^{-2}	Surface density of dark activated PDE	Frog-Carp-Mouse	1000	[121],[123], [134], [122]
σ	-	Ratio between the disk thickness and sliver thickness	Striped Bass	1	[130]
σ_{ε}	nm	Distance between the disk rim and outer plasma membrane at the sliver	Striped Bass	15	[130]
V_{cyt}	μm^3	Cytoplasmic volume	Tiger Salamander	70; 35	[114],[131]
			Mouse	14;15	[119],[131]
			Turtle	30	[131]
			Primate	30;15	[131],[114]
			Striped Bass	125	[122]
			Carp	90	[114]

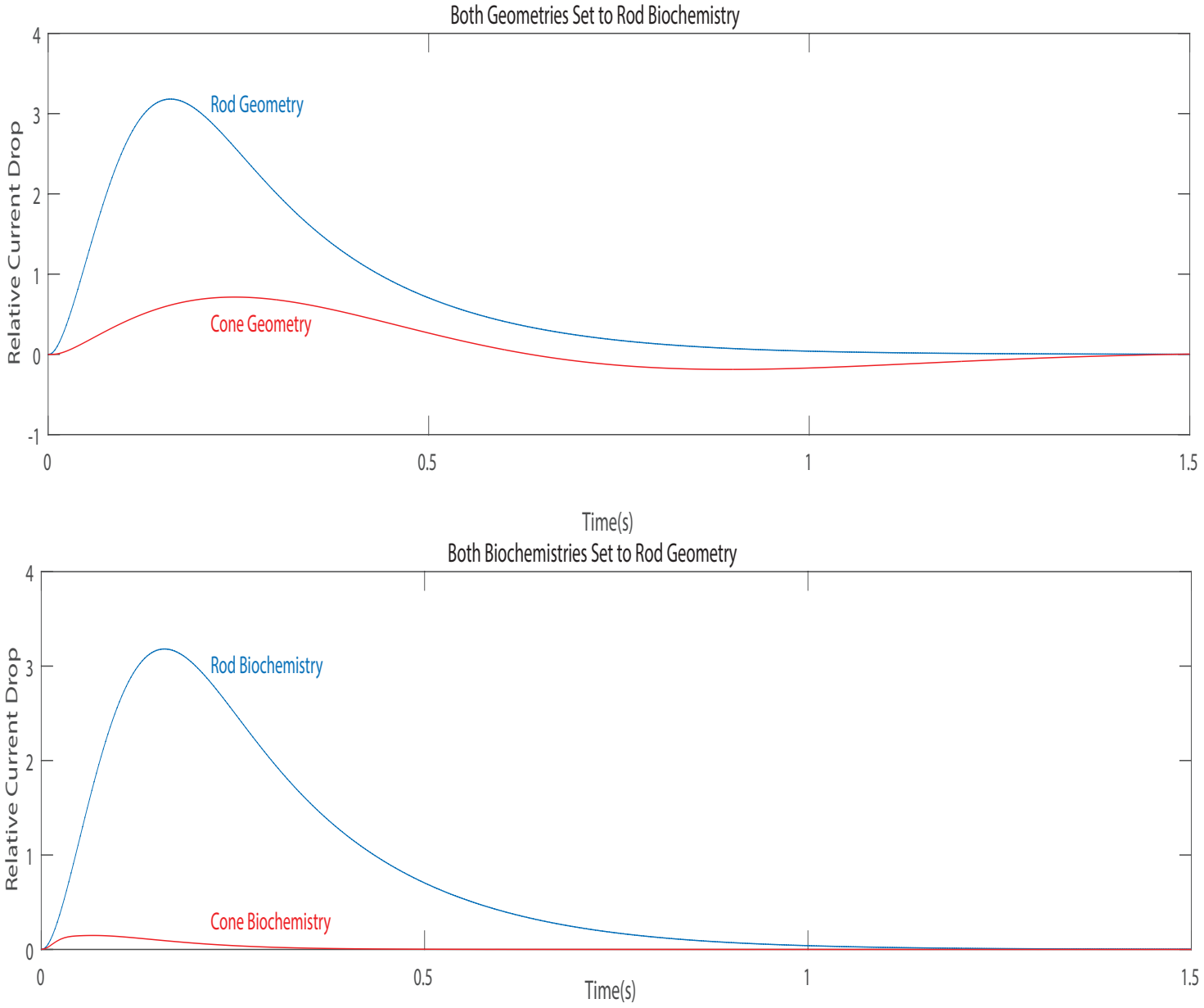

Figure 5.9: These panels compare the Mouse Rod SPR (blue) with a mutant (red) which expresses rod biochemistry on cone geometry (top) and then with a mutant which expresses the model cone biochemistry (bottom).

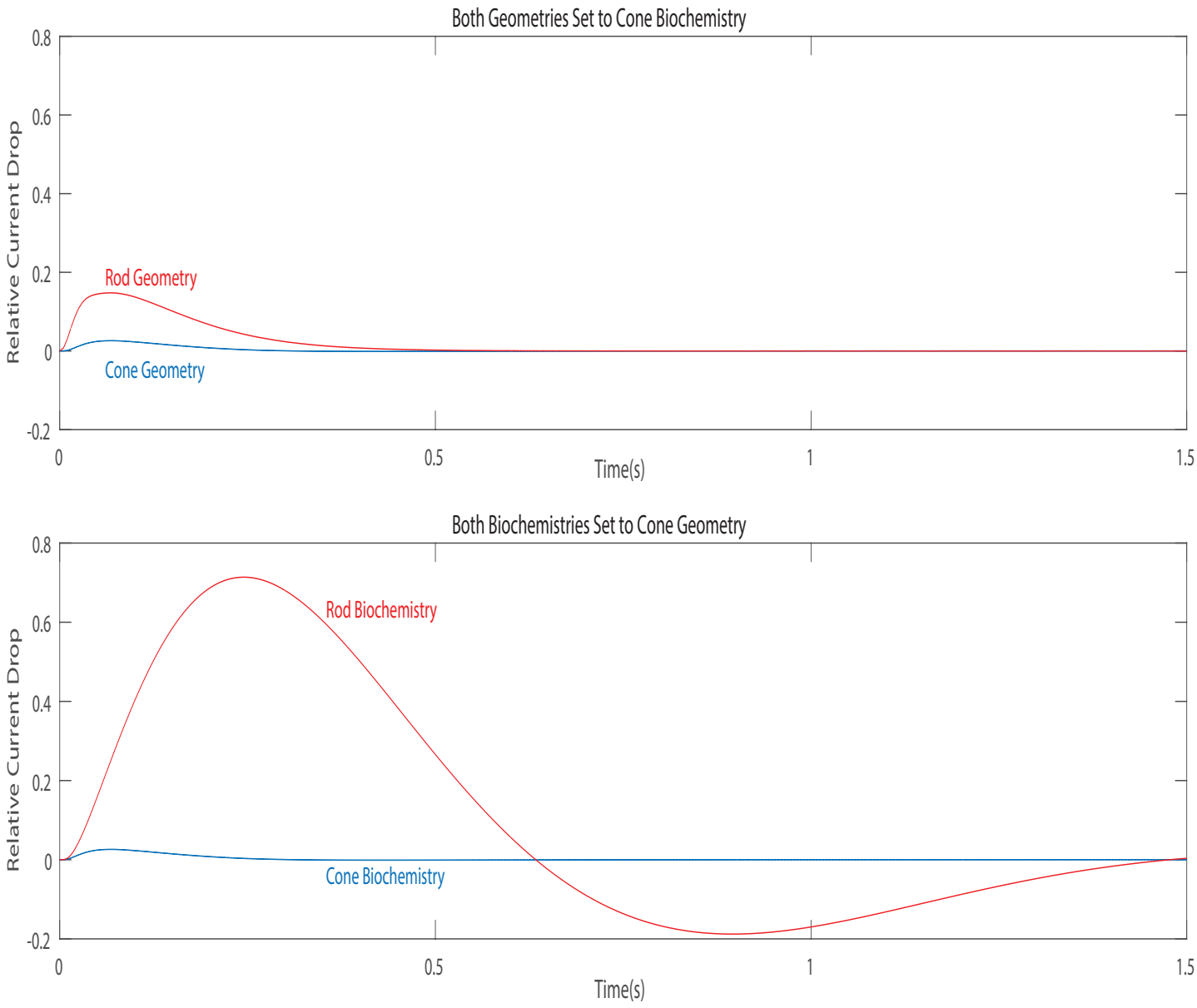

Figure 5.10: These panels compare the Model Cone SPR (blue) with a mutant (red) which expresses cone biochemistry on rod geometry (top) and then with a mutant which expresses the mouse rod biochemistry (bottom).

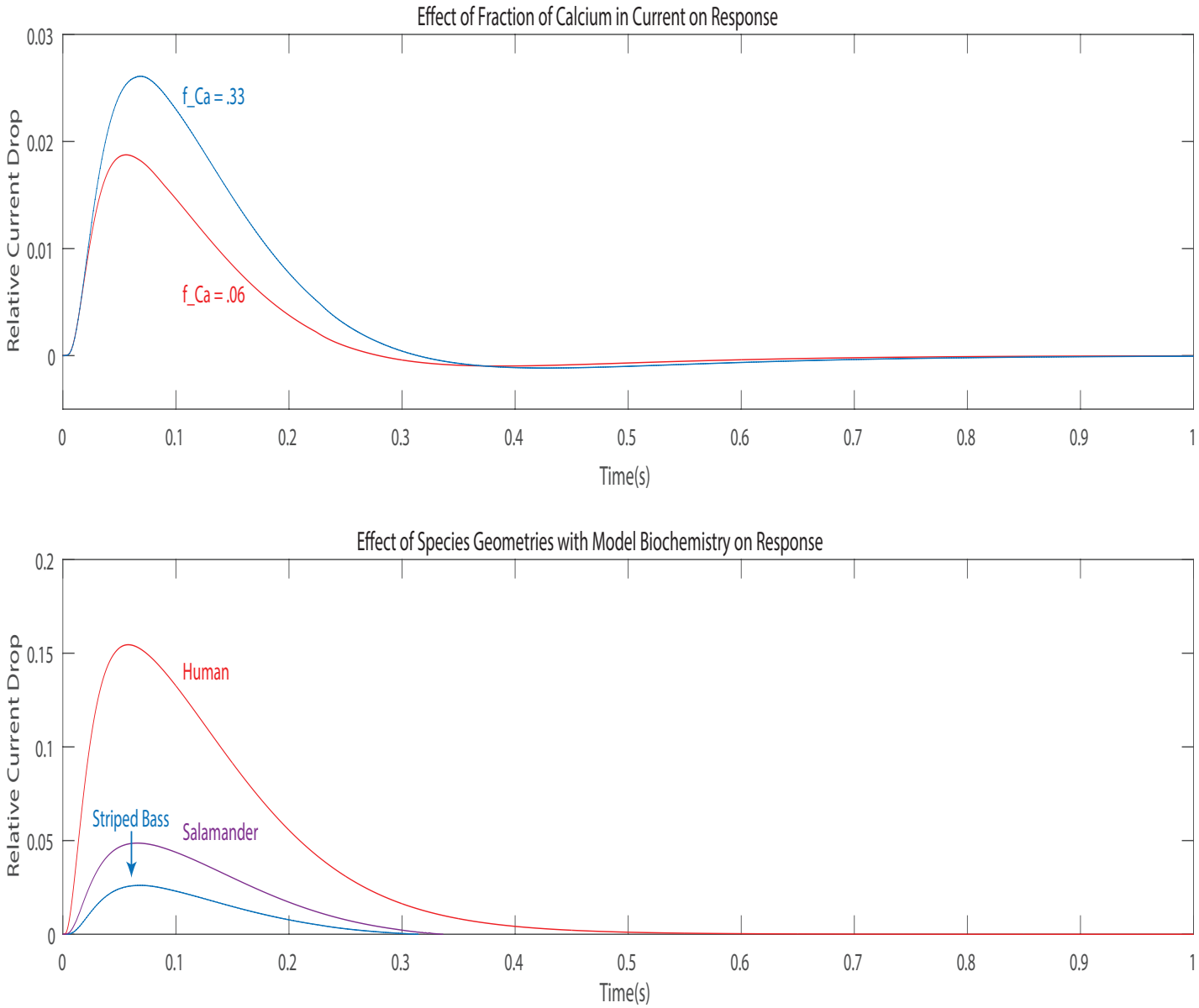

Figure 5.11: The top panel compares the response when the fraction of current carried by calcium, f_Ca, is the reported value (blue) or the rod value (red). The bottom panel shows the effect of different species geometries on response when the biochemistry has been fixed like in the Model parameter set. Human geometry is red. Salamander geometry is purple. Striped bass is blue.

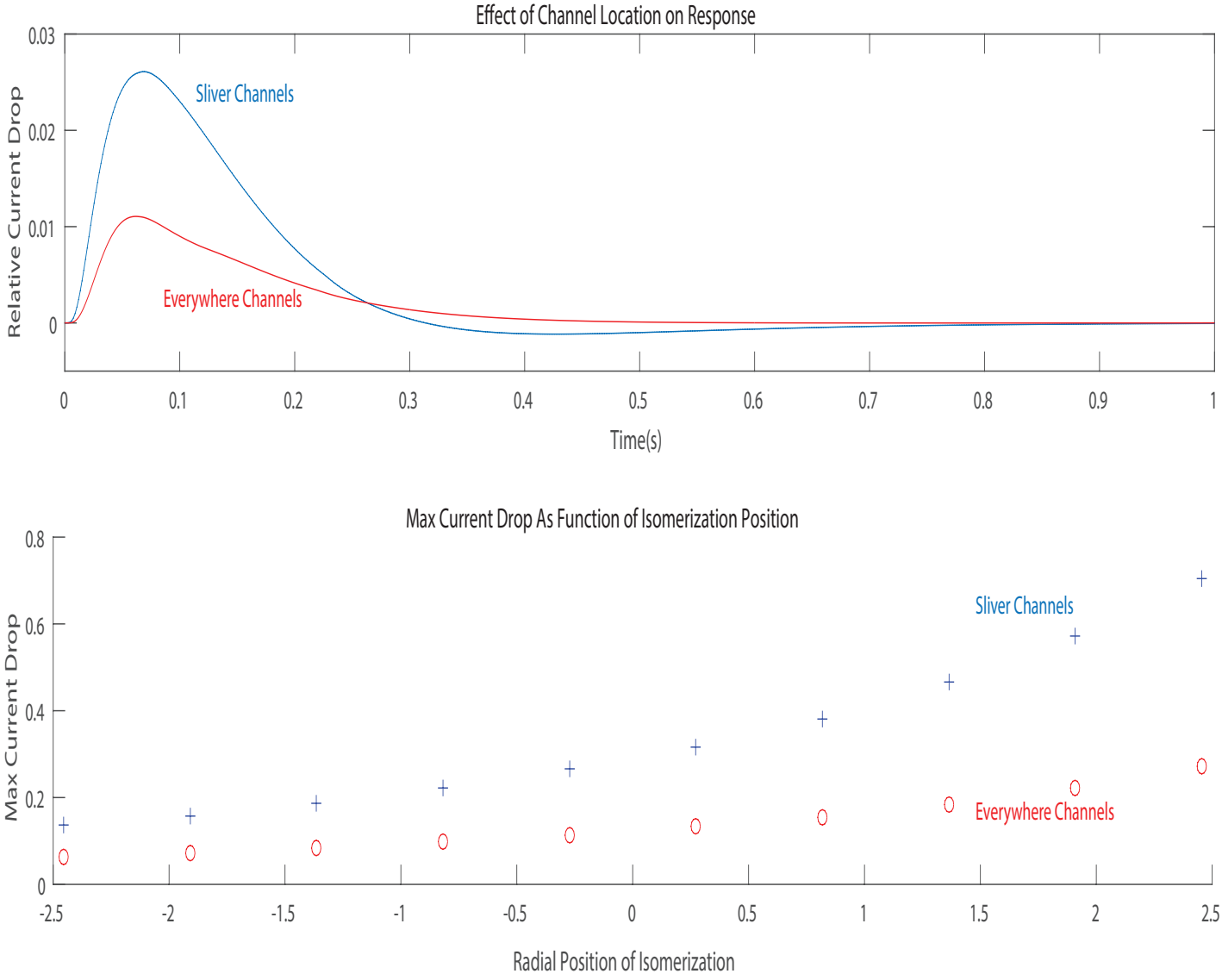

Figure 5.12: The top panel shows the effect on response of the channels being localized to the sliver (blue) or being present at the sliver, discs and folds (red). Each data point in the bottom panel is the maximum current drop of a 10 photon, numerical experiment: Draw a diameter in the disc of a cone, which evenly splits the channels. This figure's horizontal axis shows where on this diameter the isomerization occurs. As the values go from negative to positive, the isomerization spot approaches the sliver. Both cases where channels are only at the sliver (blue +) and where the channels are at the sliver, folds, and disc (red o) are shown.

BIBLIOGRAPHY

[1] L.V. Alfors. *Lectures on Quasiconformal Mappings*. Brooks/-Cole, Monterey, CA, 1987.

[2] K. Uhlenbeck. Regularity for a class of nonlinear elliptic systems. *Acta Math*, 138:219–240, 1977.

[3] L.K. Martinson and K.B. Paplov. The effect of magnetic plasticity in non-newtonian fluids. *Magnit. Gidrodinamika*, 3:69–75, 1969.

[4] L.K. Matrinson and K.B. Paplov. Unsteady shear flows of a conducting fluid with a rheological power law. *Magnit. Gidrodinamika*, 2:50–58, 1970.

[5] A. Chambolle and P.L. Lions. Image recovery via total variation minimization and related problems. *Numer. Math.*, 76:167–188, 1997.

[6] L. Rudin, S. Osher, and E. Fatemi. Nonlinear total variation based noise removal algorithms. *Phys. D*, 268:259–268, 1992.

[7] K. Ecker. *Progress in Nonlinear Differential Equations and their Applications*, chapter Regularity Theory for Mean Curvature Flow. Birkhäuser Boston Inc, Boston, MA, 2004.

[8] E. DiBenedetto, U. Gianazza, and C. Klaus. A necessary and sufficient condition for the continuity of local minima of parabolic variational integrals with linear growth. *Advances in Calculus of Variations*, 10(3):209–222, July 2017. doi: https://doi.org/10.1515/acv-2015-0014.

[9] V. Bögelein, F. Duzaar, and P. Marcellini. A time dependent variational approach to image restoration. *SIAM J. Imaging Sci*, 8(2):968–1006, 2015.

[10] W. Wieser. Parabolic q-minima and minimal solutions to variational flow. *Manuscripta Math*, 59(1):63–107, 1987.

[11] P.G. Saffman, M. Delbrück, and M. Delbrück. Brownian motion in biological membranes. *Proc. Natl. Acad. Sci. U.S.A.*, 72:3111–3113, 1975.

[12] S. Aimon, A. Callan-Jones, A. Berthaud, M. Pinot, G. S. Toombes, and P. Bassereau. Membrane shape modulates transmembrane protein distribution. *Dev. Cell*, 28:212–218, 2014.

[13] Y.A. Domanov, S. Aimon, G.E.S. Toombes, M. Renner, F. Quemeneur, A. Triller, M.S. Turner, and P Bassereau. Mobility in geometrically confined membranes. *Proc. Natl. Acad. Sci. U.S.A.*, 108:12605–12610, 2011.

[14] C.M. Waterman-Storer and E.D. Salmon. Endoplasmic reticulum membrane tubules are distributed by microtubules in living cells using three distinct mechanisms. *Curr. Biol.*, 8:798–806, 1998.

[15] C. Klaus, K. Raghunathan, E. DiBenedetto, and A. Kennworthy. Analysis of diffusion in curved surfaces and its applications to tubular membranes. *Molecular Biology of the Cell*, Dec 2016. doi: 10.1091/mbc.E16-06-0445.

[16] L. Schumaker. *Spline Functions: Computational Methods*. SIAM, 2015.

[17] V.V. Gurevich and Gurevich E.V. Phototransduction: Inactivation in cones. In Darlene A. Dartt, editor, *Encyclopedia of the Eye*, volume 3, pages 370–374. Oxford: Academic Press, 2010.

[18] E. DeGiorgi and S. Spagnolo. Sulla convergenza degli integrali dell'energia per operatori ellittici del secondo ordine. *Boll. Un. Mat. Ital.*, 4(8):391–411, 1973.

[19] P. Colli and J.F. Rodrigues. Diffusion through thin layers with high specific heat. *Asymptotice Anal*, 3:249–263, 1990.

[20] E. Giusti. *Minimal surfaces and functions of bounded variation*, volume 80 of *Monographs in Mathematics*. Birkhäuser Verlag, Basel, 1984.

[21] R. Hardt and D. Kinderlehrer. *Partial differential equations and the calculus of variations*, volume II of *Progr. Nonlinear Differential Equations Appl.*, chapter Variational principles with linear growth, pages 633–659. Birkhäuser Boston, Boston, MA, 1989.

[22] E. Bombieri. *Theory of minimal surfaces and a counterexample to the Bernstein conjecture in high dimensions*. Lecture notes. Courant Institute of Mathematical Sciences, New York, 1970.

[23] L.C. Evans. The 1-laplacian, the infinity laplacian and differential games. *Contemp. Math.*, 445:245–254, 2007.

[24] V. Caselles F. Andreu-Vaillo and J.M. Mazón. *Parabolic quasilinear equations minimizing linear growth functionals*, volume 223. Birkhäuser Verlag, Basel, 2004.

[25] V. Bögelein, F. Duzaar, and P. Marcellini. A time dependent variational approach to image restoration. *Siam J. Imaging Sci*, 8:968–1006, 2015.

[26] V. Bögelein, F. Duzaar, and C. Scheven. The total variation flow with time dependent boundary values. preprint, 2015.

[27] A. Lichnewsky and R. Temam. Pseudosolutions of the time-dependent minimal surface problem. *J. Differential Equations*, 30(3):340–364, 1978.

[28] W.P. Ziemer. *Weakly differentiable functions*. Number 120 in Graduate Texts in Mathematics. Springer-Verlag, New York, 1989.

[29] E. DiBenedetto, U. Gianazza, and V. Vespri. *Harnack's Inequality for Degenerate and Singular Parabolic Equations*. Springer Monographs in Mathematics. Springer-Verlag, New York, 2012.

[30] P. Sternberg, G. Williams, and W.P. Ziemer. Existence, uniqueness, and regularity for functions of least gradient. *J. Reine Angew. Math*, 430:35–60, 1992.

[31] P. Juutinen. p-harmonic approximation of functions of least gradient. *Indiana Univ Math J*, 54:1015–1029, 2005.

[32] J.-M. Mazón, J. Rossi, and S. Segura de León. Functions of least gradient and 1-harmonic functions. *Indiana Univ. Math. J.*, 63(4):1067–1084, 2014.

[33] B. Kawohl. On a family of torsional creep problems. *J. Reine Angew. Math*, 410:1–22, 1990.

[34] A. Mercaldo, S. Segura de León, and C. Trombetti. On the behaviour of the solutions to p-laplacian equations as p goes to 1. *Publ. Mat.*, 52(2):377–411, 2008.

[35] A. Mercaldo, S. Segura de León, and C. Trombetti. On the solutions to 1-laplacian equation with l^1 data. *J. Funct. Anal.*, 256(8):2387–2416, 2009.

[36] A. Mercaldo, J.D. Rossi, S. Segura de León, and C. Trombetti. Anisotropic p,q-laplacian equations when p goes to 1. *Nonlinear Anal.*, 73(11):3546–3560, 2010.

[37] A. Mercaldo, J.D. Rossi, S. Segura de León, and C. Trombetti. Behavior of p-laplacian problems with neumann boundary conditions when p goes to 1. *Commun. Pure Appl. Anal.*, 12(1):253–267, 2013.

[38] R.L. Jerrard, A. Moradifam, and A.I. Nachman. Existence and uniqueness of minimizers of general least gradient problems. *J. Reine Angew. Math,ahead of print*, 2015.

[39] G. Bellettini, V. Caselles, and M. Novaga. The total variation flow in $\mathbb{R}^N$. *J. Differential Equations*, 184(2):475–525, 2002.

[40] F. Andreu-Vaillo, C. Ballester, V. Caselles, and J.-M. Mazón. The dirichlet problem for the total variational flow. *J. Funct. Anal.*, 180(2):347–403, 2001.

[41] J.S. Moll. The anisotropic total variation flow. *Math. Ann.*, 332(1):177–218, 2005.

[42] G. Anzellotti. Pairings between measures and bounded functions and compensated compactness. *Ann. Mat. Pura Appl*, 135(4):293–318, 1983.

[43] R. Kohn and R. Temam. Dual spaces of stresses and strains, with applications to hencky plasticity. *Appl. Math. Optim.*, 10(1):1–35, 1983.

[44] V. Bögelein, F. Duzaar, and P. Marcellini. Existence of evolutionary variational solutions via the calculus of variations. *Journal of Differential Equations*, 256:3912–3942, 2014.

[45] E. DiBenedetto. *Real Analysis*. Birkhäuser Advanced Texts, 2002.

[46] G. Leoni. *A first course in Sobolev spaces*, volume 105. American Mathematical Society, Providence, RI, 2009.

[47] L. Ambrosio, N. Fusco, and D. Pallara. *Functions of bounded variation and free discontinuity problems*. Oxford Mathematical Monographs. The Clarendon Press, Oxford University Press, 2000.

[48] V. Bögelein, F. Duzaar, J. Kinnunen, and P. Marcellini. A variational approach to the total variation flow, preprint. 2014.

[49] G. Anzellotti and M. Giaquinta. Funzioni bv e tracce. *Rend. Sem. Mat.*, 60:1–21, 1978.

[50] D. Choquet and A. Triller. The role of receptor diffusion in the organization of the postsynaptic membrane. *Nat. Rev. Neurosci.*, 4(4):251–265, Apr 2003.

[51] A. D. Douglass and R. D. Vale. Single-molecule microscopy reveals plasma membrane microdomains created by protein-protein networks that exclude or trap signaling molecules in T cells. *Cell*, 121(6):937–950, Jun 2005.

[52] A. Kusumi, H. Ike, C. Nakada, K. Murase, and T. Fujiwara. Single-molecule tracking of membrane molecules: plasma membrane compartmentalization and dynamic assembly of raft-philic signaling molecules. *Semin. Immunol.*, 17(1):3–21, Feb 2005.

[53] S. Eisenberg, D. E. Shvartsman, M. Ehrlich, and Y. I. Henis. Clustering of raft-associated proteins in the external membrane leaflet modulates internal leaflet H-ras diffusion and signaling. *Mol. Cell. Biol.*, 26(19):7190–7200, Oct 2006.

[54] P. Lajoie, E. A. Partridge, G. Guay, J. G. Goetz, J. Pawling, A. Lagana, B. Joshi, J. W. Dennis, and I. R. Nabi. Plasma membrane domain organization regulates EGFR signaling in tumor cells. *J. Cell Biol.*, 179(2):341–356, Oct 2007.

[55] B. Treanor, D. Depoil, A. Gonzalez-Granja, P. Barral, M. Weber, O. Dushek, A. Bruckbauer, and F. D. Batista. The membrane skeleton controls diffusion dynamics and signaling through the B cell receptor. *Immunity*, 32(2):187–199, Feb 2010.

[56] S. Suetsugu and A. Gautreau. Synergistic BAR-NPF interactions in actin-driven membrane remodeling. *Trends Cell Biol.*, 22(3):141–150, Mar 2012.

[57] V. Jaumouille, Y. Farkash, K. Jaqaman, R. Das, C. A. Lowell, and S. Grinstein. Actin cytoskeleton reorganization by Syk regulates Fc receptor responsiveness by increasing its lateral mobility and clustering. *Dev. Cell*, 29(5):534–546, Jun 2014.

[58] D. Krapf. Mechanisms underlying anomalous diffusion in the plasma membrane. *Curr Top Membr*, 75:167–207, 2015.

[59] W. S. Trimble and S. Grinstein. Barriers to the free diffusion of proteins and lipids in the plasma membrane. *J. Cell Biol.*, 208(3):259–271, Feb 2015.

[60] D. V. Koster and S. Mayor. Cortical actin and the plasma membrane: inextricably intertwined. *Curr. Opin. Cell Biol.*, 38:81–89, Feb 2016.

[61] E. P. Petrov and P. Schwille. Translational diffusion in lipid membranes beyond the Saffman-Delbruck approximation. *Biophys. J.*, 94(5):L41–43, Mar 2008.

[62] C. Eggeling, C. Ringemann, R. Medda, G. Schwarzmann, K. Sandhoff, S. Polyakova, V. N. Belov, B. Hein, C. von Middendorff, A. Schonle, and S. W. Hell. Direct observation of the nanoscale dynamics of membrane lipids in a living cell. *Nature*, 457(7233):1159–1162, Feb 2009.

[63] A. Kusumi, Y. M. Shirai, I. Koyama-Honda, K. G. Suzuki, and T. K. Fujiwara. Hierarchical organization of the plasma membrane: investigations by single-molecule tracking vs. fluorescence correlation spectroscopy. *FEBS Lett.*, 584(9):1814–1823, May 2010.

[64] F. Harb, J. Sarkis, N. Ferte, and B. Tinland. Beyond Saffman-Delbruck approximation: a new regime for 2D diffusion of -hemolysin complexes in supported lipid bilayer. *Eur Phys J E Soft Matter*, 35(11):118, Nov 2012.

[65] E. Edwald, M. B. Stone, E. M. Gray, J. Wu, and S. L. Veatch. Oxygen depletion speeds and simplifies diffusion in HeLa cells. *Biophys. J.*, 107(8):1873–1884, Oct 2014.

[66] P. G. Saffman and M. Delbruck. Brownian motion in biological membranes. *Proc. Natl. Acad. Sci. U.S.A.*, 72(8):3111–3113, Aug 1975.

[67] I. F. Sbalzarini, A. Mezzacasa, A. Helenius, and P. Koumoutsakos. Effects of organelle shape on fluorescence recovery after photobleaching. *Biophys. J.*, 89(3):1482–1492, Sep 2005.

[68] S. M. Leitenberger, E. Reister-Gottfried, and U. Seifert. Curvature coupling dependence of membrane protein diffusion coefficients. *Langmuir*, 24(4):1254–1261, Feb 2008.

[69] J. Adler, A. I. Shevchuk, P. Novak, Y. E. Korchev, and I. Parmryd. Plasma membrane topography and interpretation of single-particle tracks. *Nat. Methods*, 7(3):170–171, Mar 2010.

[70] S. Guerrier, J. Coutinho-Budd, T. Sassa, A. Gresset, N. V. Jordan, K. Chen, W. L. Jin, A. Frost, and F. Polleux. The F-BAR domain of srGAP2 induces membrane protrusions required for neuronal migration and morphogenesis. *Cell*, 138(5):990–1004, Sep 2009.

[71] T. Baumgart, S. T. Hess, and W. W. Webb. Imaging coexisting fluid domains in biomembrane models coupling curvature and line tension. *Nature*, 425(6960):821–824, Oct 2003.

[72] J. Carlton, M. Bujny, B. J. Peter, V. M. Oorschot, A. Rutherford, H. Mellor, J. Klumperman, H. T. McMahon, and P. J. Cullen. Sorting nexin-1 mediates tubular endosome-to-TGN transport through coincidence sensing of high- curvature membranes and 3-phosphoinositides. *Curr. Biol.*, 14(20):1791–1800, Oct 2004.

[73] A. Roux, D. Cuvelier, P. Nassoy, J. Prost, P. Bassereau, and B. Goud. Role of curvature and phase transition in lipid sorting and fission of membrane tubules. *EMBO J.*, 24(8):1537–1545, Apr 2005.

[74] A. Tian and T. Baumgart. Sorting of lipids and proteins in membrane curvature gradients. *Biophys. J.*, 96(7):2676–2688, Apr 2009.

[75] M. L. Henle and A. J. Levine. Hydrodynamics in curved membranes: the effect of geometry on particulate mobility. *Phys Rev E Stat Nonlin Soft Matter Phys*, 81(1 Pt 1):011905, Jan 2010.

[76] Q. Y. Wu and Q. Liang. Interplay between curvature and lateral organization of lipids and peptides/proteins in model membranes. *Langmuir*, 30(4):1116–1122, Feb 2014.

[77] J. B. Larsen, M. B. Jensen, V. K. Bhatia, S. L. Pedersen, T. Bj?rnholm, L. Iversen, M. Uline, I. Szleifer, K. J. Jensen, N. S. Hatzakis, and D. Stamou. Membrane curvature enables N-Ras lipid anchor sorting to liquid-ordered membrane phases. *Nat. Chem. Biol.*, 11(3):192–194, Mar 2015.

[78] S. Mukherjee and F. R. Maxfield. Role of membrane organization and membrane domains in endocytic lipid trafficking. *Traffic*, 1(3):203–211, Mar 2000.

[79] S. Mukherjee and F. R. Maxfield. Membrane domains. *Annu. Rev. Cell Dev. Biol.*, 20:839–866, 2004.

[80] A. Callan-Jones, B. Sorre, and P. Bassereau. Curvature-driven lipid sorting in biomembranes. *Cold Spring Harb Perspect Biol*, 3(2), Feb 2011.

[81] J. Zimmerberg and M. M. Kozlov. How proteins produce cellular membrane curvature. *Nat. Rev. Mol. Cell Biol.*, 7(1):9–19, Jan 2006.

[82] M. M. Kozlov, F. Campelo, N. Liska, L. V. Chernomordik, S. J. Marrink, and H. T. McMahon. Mechanisms shaping cell membranes. *Curr. Opin. Cell Biol.*, 29:53–60, Aug 2014.

[83] H. T. McMahon and E. Boucrot. Membrane curvature at a glance. *J. Cell. Sci.*, 128(6):1065–1070, Mar 2015.

[84] Y. Rao and V. Haucke. Membrane shaping by the Bin/amphiphysin/Rvs (BAR) domain protein superfamily. *Cell. Mol. Life Sci.*, 68(24):3983–3993, Dec 2011.

[85] T. Yoshigaki. Theoretically predicted effects of Gaussian curvature on lateral diffusion of membrane molecules. *Phys Rev E Stat Nonlin Soft Matter Phys*, 75(4 Pt 1):041901, Apr 2007.

[86] R. Kusters, L. C. Kapitein, C. C. Hoogenraad, and C. Storm. Shape-induced asymmetric diffusion in dendritic spines allows efficient synaptic AMPA receptor trapping. *Biophys. J.*, 105(12):2743–2750, Dec 2013.

[87] Y. A. Domanov, S. Aimon, G. E. Toombes, M. Renner, F. Quemeneur, A. Triller, M. S. Turner, and P. Bassereau. Mobility in geometrically confined membranes. *Proc. Natl. Acad. Sci. U.S.A.*, 108(31):12605–12610, Aug 2011.

[88] D. R. Daniels and M. S. Turner. Diffusion on membrane tubes: a highly discriminatory test of the Saffman-Delbruck theory. *Langmuir*, 23(12):6667–6670, Jun 2007.

[89] M. Renner, Y. Domanov, F. Sandrin, I. Izeddin, P. Bassereau, and A. Triller. Lateral diffusion on tubular membranes: quantification of measurements bias. *PLoS ONE*, 6(9):e25731, 2011.

[90] C. M. Waterman-Storer and E. D. Salmon. Endoplasmic reticulum membrane tubules are distributed by microtubules in living cells using three distinct mechanisms. *Curr. Biol.*, 8(14):798–806, Jul 1998.

[91] K. E. Sorra and K. M. Harris. Overview on the structure, composition, function, development, and plasticity of hippocampal dendritic spines. *Hippocampus*, 10(5):501–511, 2000.

[92] G. J. Pazour and G. B. Witman. The vertebrate primary cilium is a sensory organelle. *Curr. Opin. Cell Biol.*, 15(1):105–110, Feb 2003.

[93] A. Upadhyaya and M. P. Sheetz. Tension in tubulovesicular networks of Golgi and endoplasmic reticulum membranes. *Biophys. J.*, 86(5):2923–2928, May 2004.

[94] W. Romer, L. Berland, V. Chambon, K. Gaus, B. Windschiegl, D. Tenza, M. R. Aly, V. Fraisier, J. C. Florent, D. Perrais, C. Lamaze, G. Raposo, C. Steinem, P. Sens, P. Bassereau, and L. Johannes. Shiga toxin induces tubular membrane invaginations for its uptake into cells. *Nature*, 450(7170):670–675, Nov 2007.

[95] C. A. Day, N. W. Baetz, C. A. Copeland, L. J. Kraft, B. Han, A. Tiwari, K. R. Drake, H. De Luca, D. J. Chinnapen, M. W. Davidson, R. K. Holmes, M. G. Jobling, T. A. Schroer, W. I. Lencer, and A. K. Kenworthy. Microtubule motors power plasma membrane tubulation in clathrin-independent endocytosis. *Traffic*, 16(6):572–590, Jun 2015.

[96] D. A. Berk and R. M. Hochmuth. Lateral mobility of integral proteins in red blood cell tethers. *Biophys. J.*, 61(1):9–18, Jan 1992.

[97] F. Daumas, N. Destainville, C. Millot, A. Lopez, D. Dean, and L. Salome. Confined diffusion without fences of a g-protein-coupled receptor as revealed by single particle tracking. *Biophys. J.*, 84(1):356–366, Jan 2003.

[98] A. K. Kenworthy, B. J. Nichols, C. L. Remmert, G. M. Hendrix, M. Kumar, J. Zimmerberg, and J. Lippincott-Schwartz. Dynamics of putative raft-associated proteins at the cell surface. *J. Cell Biol.*, 165(5):735–746, Jun 2004.

[99] H. Jiang and T. R. Powers. Curvature-driven lipid sorting in a membrane tubule. *Phys. Rev. Lett.*, 101(1):018103, Jul 2008.

[100] D. Holcman and Z. Schuss. Diffusion laws in dendritic spines. *J Math Neurosci*, 1(1):10, Oct 2011.

[101] P. Singh, P. Mahata, T. Baumgart, and SL. Das. Curvature sorting of proteins on a cylindrical lipid membrane tether connected to a reservoir. *Phys Rev E Stat Nonlin Soft Matter Phys*, 85:1–10, 2012.

[102] R. Kusters, S. Paquay, and C. Storm. Confinement without boundaries: anisotropic diffusion on the surface of a cylinder. *arXiv*, page 1407.3564.

[103] Gikhman II and Skorohod AV. *Introduction to the Theory of Random Processes*. Saunders, Philadelphia, 1969.

[104] Heltai L Arroyo M, DeSimone A. The role of membrane viscosity in the dynamics of fluid membranes. *arXiv*, (1007.4934), 2010.

[105] M. Rahimi and M. Arroyo. Shape dynamics, lipid hydrodynamics, and the complex viscoelasticity of bilayer membranes [corrected]. *Phys Rev E Stat Nonlin Soft Matter Phys*, 86(1 Pt 1):011932, Jul 2012.

[106] M. Rahimi, A. DeSimone, and M. Arroyo. Curved fluid membranes behave laterally as effective viscoelastic media. *Soft Matter*, 9:11033, 2013.

[107] A. J. Kosmalska, L. Casares, A. Elosegui-Artola, J. J. Thottacherry, R. Moreno-Vicente, V. Gonzalez-Tarrago, M. A. del Pozo, S. Mayor, M. Arroyo, D. Navajas, X. Trepat, N. C. Gauthier, and P. Roca-Cusachs. Physical principles of membrane remodelling during cell mechanoadaptation. *Nat Commun*, 6:7292, Jun 2015.

[108] M. L. Henle, R. McGorty, A.D. Dinsmore, and A. J. Levine. The effect of curvature and topology on membrane hydrodynamics. *EPL (Europhys Lett)*, 84, 48001, 2007.

[109] G. Guigas and M. Weiss. Size-dependent diffusion of membrane inclusions. *Biophys. J.*, 91(7):2393–2398, Oct 2006.

[110] C. Zhu, S. L. Das, and T. Baumgart. Nonlinear sorting, curvature generation, and crowding of endophilin N-BAR on tubular membranes. *Biophys. J.*, 102(8):1837–1845, Apr 2012.

[111] P. Ramesh, Y. F. Baroji, S. N. Reihani, D. Stamou, L. B. Oddershede, and P. M.

Bendix. FBAR syndapin 1 recognizes and stabilizes highly curved tubular membranes in a concentration dependent manner. *Sci Rep*, 3:1565, 2013.

[112] M. Simunovic, G. A. Voth, A. Callan-Jones, and P. Bassereau. When Physics Takes Over: BAR Proteins and Membrane Curvature. *Trends Cell Biol.*, 25(12):780–792, Dec 2015.

[113] M. A. Puthenveedu, B. Lauffer, P. Temkin, R. Vistein, P. Carlton, K. Thorn, J. Taunton, O. D. Weiner, R. G. Parton, and M. von Zastrow. Sequence-dependent sorting of recycling proteins by actin-stabilized endosomal microdomains. *Cell*, 143(5):761–773, Nov 2010.

[114] S. Kawamura and S. Tachibanaki. Rod and cone photoreceptors: molecular basis of the difference in their physiology. *Comp. Biochem. Physiol., Part A Mol. Integr. Physiol.*, 150(4):369–377, Aug 2008.

[115] J. I. Korenbrot. Speed, sensitivity, and stability of the light response in rod and cone photoreceptors: facts and models. *Prog Retin Eye Res*, 31(5):442–466, Sep 2012.

[116] G. Caruso, P. Bisegna, L. Lenoci, D. Andreucci, V. V. Gurevich, H. E. Hamm, and E. DiBenedetto. Kinetics of rhodopsin deactivation and its role in regulating recovery and reproducibility of rod photoresponse. *PLoS Comput. Biol.*, 6(12):e1001031, Dec 2010.

[117] L. Shen, G. Caruso, P. Bisegna, D. Andreucci, V. V. Gurevich, H. E. Hamm, and E. DiBenedetto. Dynamics of mouse rod phototransduction and its sensitivity to variation of key parameters. *IET Syst Biol*, 4(1):12–32, Jan 2010.

[118] S. Tachibanaki, Y. Shimauchi-Matsukawa, D. Arinobu, and S. Kawamura. Molecular mechanisms characterizing cone photoresponses. *Photochem. Photobiol.*, 83(1):19–26, 2007.

[119] S. S. Nikonov, R. Kholodenko, J. Lem, and E. N. Pugh. Physiological features of the S- and M-cone photoreceptors of wild-type mice from single-cell recordings. *J. Gen. Physiol.*, 127(4):359–374, Apr 2006.

[120] P. Bisegna, G. Caruso, D. Andreucci, L. Shen, V. V. Gurevich, H. E. Hamm, and E. DiBenedetto. Diffusion of the second messengers in the cytoplasm acts as a variability suppressor of the single photon response in vertebrate phototransduction. *Biophys. J.*, 94(9):3363–3383, May 2008.

[121] Kawamura. Unpublished table of biochemical parameters. Made available by request., Jan 2016.

[122] D. Holcman and J. I. Korenbrot. The limit of photoreceptor sensitivity: molecular mechanisms of dark noise in retinal cones. *J. Gen. Physiol.*, 125(6):641–660, Jun 2005.

[123] S. Tachibanaki, S. Tsushima, and S. Kawamura. Low amplification and fast visual pigment phosphorylation as mechanisms characterizing cone photoresponses. *Proc. Natl. Acad. Sci. U.S.A.*, 98(24):14044–14049, Nov 2001.

[124] N. Takemoto, S. Tachibanaki, and S. Kawamura. High cGMP synthetic activity in carp cones. *Proc. Natl. Acad. Sci. U.S.A.*, 106(28):11788–11793, Jul 2009.

[125] T. Ohyama, A. Picones, and J. I. Korenbrot. Voltage-dependence of ion permeation in cyclic GMP-gated ion channels is optimized for cell function in rod and cone photoreceptors. *J. Gen. Physiol.*, 119(4):341–354, Apr 2002.

[126] J. I. Korenbrot. Speed, adaptation, and stability of the response to light in cone photoreceptors: the functional role of Ca-dependent modulation of ligand sensitivity in cGMP-gated ion channels. *J. Gen. Physiol.*, 139(1):31–56, Jan 2012.

[127] K. W. Koch and L. Stryer. Highly cooperative feedback control of retinal rod guanylate cyclase by calcium ions. *Nature*, 334(6177):64–66, Jul 1988.

[128] J. M. Corless, E. Worniallo, and R. D. Fetter. Modulation of disk margin structure during renewal of cone outer segments in the vertebrate retina. *J. Comp. Neurol.*, 287(4):531–544, Sep 1989.

[129] D. Arinobu, S. Tachibanaki, and S. Kawamura. Larger inhibition of visual pigment kinase in cones than in rods. *J. Neurochem.*, 115(1):259–268, Oct 2010.

[130] D. Holcman and J. I. Korenbrot. Longitudinal diffusion in retinal rod and cone outer segment cytoplasm: the consequence of cell structure. *Biophys. J.*, 86(4):2566–2582, Apr 2004.

[131] E. N. Pugh and T. D. Lamb. Chapter 5 phototransduction in vertebrate rods and cones: Molecular mechanisms of amplification, recovery and light adaptation. *Handbook of Biological Physics*, 3:183–255, 2000. doi:10.1016/S1383-8121(00)80008-1.

[132] T. I. Rebrik, E. A. Kotelnikova, and J. I. Korenbrot. Time course and Ca(2+) dependence of sensitivity modulation in cyclic GMP-gated currents of intact cone photoreceptors. *J. Gen. Physiol.*, 116(4):521–534, Oct 2000.

[133] Y. Koshitani, S. Tachibanaki, and S. Kawamura. Quantitative aspects of cGMP phosphodiesterase activation in carp rods and cones. *J. Biol. Chem.*, 289(5):2651–2657, Jan 2014.

[134] S. Tachibanaki, S. Yonetsu, S. Fukaya, Y. Koshitani, and S. Kawamura. Low activation and fast inactivation of transducin in carp cones. *J. Biol. Chem.*, 287(49):41186–41194, Nov 2012.

[135] K. Tsutsui, S. Tachibanaki, Y. Shimauchi-Matsukawa, Y. Shichida, and S. Kawamura. Different phosphorylation rates among vertebrate cone visual pigments with different spectral sensitivities. *Biochem. Biophys. Res. Commun.*, 440(4):630–634, Nov 2013.

[136] A. Picones and J. I. Korenbrot. Permeation and interaction of monovalent cations with the cGMP-gated channel of cone photoreceptors. *J. Gen. Physiol.*, 100(4):647–673, Oct 1992.